Numerical Aspects of Population Balance Equations Coupled to Computational Fluid Dynamics

---

Dissertation
zur Erlangung des Grades eines
Doktors der Naturwissenschaften

Der Fakultät für Mathematik der
Technischen Universität Dortmund
vorgelegt am 2014 von

Evren Bayraktar

Abstract

It can be the motion of clouds, the movement of a smoke plume, or the dynamics of fluids in processes which are interesting to food, petroleum, chemical, pharmaceutical and many other industries; they are all governed by the same physical laws: fluid dynamics and population balances.

Numerical solution of Population Balance Equations (PBE) coupled to Computational Fluid Dynamics (CFD) is a promising approach to simulate liquid/gas–liquid dispersed flows, for which the governing physical phenomena are breakup and coalescence of bubbles/droplets, additional to transport phenomena of fluids.

In the literature, there are many breakup and coalescence models to close the PBE. Unfortunately, there is no unified framework for these closures; and, it is one of our objectives: to determine appropriate coalescence and breakage kernels for liquid/gas–liquid dispersions.

Another objective is to investigate numerical techniques for one-way coupled CFD and PBE, and to develop a computational tool. The developed tool is based on the incompressible flow solver FEATFLOW which is extended with Chien's Low-Reynolds number $k-\varepsilon$ turbulence model and PBE.

The presented implementation ensures strictly conservative treatment of sink and source terms which is enforced even for geometric discretization of the internal coordinate. The validation of our implementation which covers a wide range of computational and experimental problems enables us to proceed into three-dimensional applications as, turbulent flows in a pipe and through static mixers.

Regarding the studies on static mixers, not only we have obtained numerical results; we have conducted comprehensive experimental studies in the Sulzer Chemtech Ltd. laboratories (Winterthur, Switzerland). The inclusive experimental results has offered a good ground for verifying the adopted mathematical models and numerical techniques.

The obtained satisfactory results in the studies for one-way coupled CFD and PBE has motivated us to study two-way coupled CFD-PBE models. The so far developed numerical recipe of which main ingredients are the method of classes, positivity-preserving linearization and the high-order FEM-AFC with FEATFLOW including the standard $k-\varepsilon$ solver has been extended to cover bubble induced turbulence and mixture-model with algebraic slip relation. A smart algorithm is developed, offering a compromise between the computational cost and the accuracy.

Numerical simulation of air-in-water dispersed phase systems in a flat bubble column which is, numerically, a very challenging case-study and is experimentally studied by Becker et al. has been performed with the developed computational tool. The dynamic movement of the bubble swarm which is observed in the experiments have been successfully simulated.

Keywords: computational fluid dynamics (CFD), population balances, coalescence, breakage, numerical solution, method of classes, parallel parent daughter classes, simulation, static mixers, multiphase flows.

"*Do not worry about your difficulties in mathematics,*
I assure you that mine are greater."

Albert Einstein

Acknowledgements

First and foremost, I would like to present my endless gratitude to Prof. Stefan Turek, who gave me the opportunity to work at LS III where I have had an access to excellent research facilities and have enjoyed the friendly atmosphere. He gave me the ticket to a new world: applied mathematics and numerics, where I have been fascinated by his works. He has always been supportive, encouraging and guiding; so that, this study has been accomplished.

Prof. Dmitri Kuzmin, thank you very much for being so kind to review my dissertation, your remarks and advices are invaluable. Without your guiding studies and suggestions, from which I have benefited quite a lot, this work would have been incomplete.

JP Dr. Dominik Göddeke, thank you very much for kindly accepting to be a member of the examination committee.

Otto and Frank, they are great people, friends, officemates and researchers; whose experience and knowledge helped me all the way through my studies. Thank you my friends.

I have been a member of, fortunately, a very big and great group, LS III; unfortunately, it is not possible to mention here all the names, thank you all; especially to those whom I have bothered anytime when I have had a problem with computers; thank you very much, Sven and Christian.

I must mention Dr. Hirschberg and Mr. Schöck from Sulzer Chemtech and Sulzer Innotec, Switzerland, which supported me with a doctoral grant. Their work was very motivative for this study. They have always been very interested in my studies, provided experimental results; moreover, they let me to access their laboratory where I have conducted experiments which were essential for this study. I have very much enjoyed their hospitality and friendship, thanks a lot.

My family, they have always been a great support; they always let me know that they are there for me; they have believed in me, have trusted in me; thank you very much for everything.

Dear Mila, living in Dortmund would not feel so warm, pleasant and joyful without you, my sincere gratitude.

Dortmund, September 17, 2014

Evren Bayraktar

Contents

1

Introduction

The dispersed two-phase flow is one of the most common flow types observed both in the nature and in industrial processes. It can be the motion of clouds, the movement of a smoke plume, or the dynamics of fluids in processes which are interesting to food, petroleum, chemical, pharmaceutical and many other industries; they are all governed by the same physical laws. Even though the dispersed phase systems[1] are encountered so often in daily life and in the industrial processes worth billions of Euros, our understanding of the physical laws governing the dispersed phase systems is still quite limited; and indeed, it is not due to lack of interest in this research field but "simply" due to being the physical phenomena highly complex and tangled.

The dispersed phase systems can be categorized into four: solid–liquid (crystallization systems), solid–gas (smoke/soot dispersion), gas–liquid (aerobic fermentation) and liquid–liquid (petroleum industry, polymerization) dispersions. Each of these dispersed phase systems is a distinct problem to be understood and to be solved by the researchers of the corresponding field. Liquid–liquid and gas–liquid dispersions which are in the scope of this study are such that the continuous (primary) phase is liquid and the dispersed phase (secondary phase) is either liquid or gas.

The liquid–liquid and gas–liquid dispersions are commonly used for many diverse purposes in the following fields:

- water & wastewater treatment: aeration of water, ozonation of water, pH–control and neutralization.
- oil & gas refinery in the applications: crude oil blending and crude oil desalting.
- food industry in the production of beer, wine, mineral water and soft-drinks.

All these applications serve to different purposes but require the same: a homogeneous mixing and a narrow size distribution of the dispersed phase. In these fields and many others, two ways to obtain the required dispersed phase systems are using in-line *static mixers* and employing *bubble column reactors*.

[1] Dispersed phase system refers to the dispersion of two phases in the context of this thesis.

In cases of static mixer applications or bubble column reactors, our understanding of the physical phenomena governing the evolution of the dispersed phase in a flow field is very limited; although, the first studies on this field can be found from the 17th century by Stevin (1605) and Newton (1687). The question to be answered is a very "simple" one:

> *How does the dispersed phase evolve in time and space with the hydrodynamic quantities and physical properties of the phases?*

In the case of liquid/gas–liquid dispersions, the governing physical phenomena are bubble[2] breakup and coalescence, additional to transport phenomena of fluids. Bubble breakup occurs due to collisions of the turbulent eddies with bubbles. Moreover, the turbulent eddies which have larger sizes than the bubbles transport the bubbles in space and cause bubble–bubble collision that can result in coalescence. These phenomena are mathematically modeled by many different researchers; nevertheless, there is no unified framework of these models, particularly for the breakup phenomenon.

On the one hand, the evolution of the bubble size distribution is an example of a research field which involves the population balance modeling; the transport phenomena of fluid is another problem which has still been studied by many researchers of distinct fields. However, an attempt on solving the *transport problem* of the dispersed phase systems requires the solution of the problems of these distinct research fields.

The transport phenomena discuss three closely related topics: fluid dynamics, heat transfer and mass transfer. In the transport problem of isothermal immiscible dispersed phase systems, e.g. oil in water and air in water at constant temperature, where there is negligible mass transfer and no heat transfer, we are left with *Fluid Dynamics*. The fluid dynamics is described with the *Navier-Stokes Equations* for the fluids which are sufficiently dense to be considered as continuum and have velocities for which the laws of Newtonian physics are still valid. Navier-Stokes Equations are a nonlinear set of partial differential equations (PDEs) governing the motion of fluids whose stress is linearly dependent on pressure and velocity gradients. Since the equations do not possess general closed-forms solutions, problems of this field are solved by using computational tools; and, they are primary interest of *Computational Fluid Dynamics* (CFD).

Population balances may be regarded either as an old subject that has its origin in the Boltzmann equation more than a century ago, or as a relatively new one in light of the variety of applications in which engineers have recently put population balances to use. There is an intensive ongoing research in this field by researchers of many different backgrounds. Applications cover a wide range of dispersed systems for which the analytical solutions of *Population Balance Equations* (PBE) are limited to very specific cases being far from encountered ones in industrial applications. And, this study will investigate the numerical solution of PBE for gas/liquid–liquid dispersed systems where no analytical solution is available [2].

In practical applications a single bubble size model, as reported by numerous researchers [3,4], cannot properly describe the interfacial interactions between the phases, and analytical solutions of the PBE are available just for very few and specific cases. Hence, the use of appropriate numerical techniques is unavoidable in order to deal with practical problems. There are several numerical methods satisfying the necessary requirements with respect to robustness and realizability: the method of moments (MOM) [5], the quadrature method of moments [6, 7], the direct quadrature

[2]Unless it is explicitly stated, bubble also refers to droplet in the context of this chapter, but not the other way around. It is needed to adopt this convention due to readability purposes.

method of moments (DQMM) [8], parallel parent and daughter classes (PPDC) [9] and the method of classes (MC) [10, 11].

The choice of appropriate numerical technique depends on the nature of the problem and the results which are of interest. If the problem in the scope does not exhibit any spatial variation and, rather than the size distribution, certain statistical values are interesting, one can immediately employ a moment based method like PPDC or MOM to solve the PBE. However, if PBE equations are to be solved for the dispersed phase systems in bubble columns or static mixer applications, it is not that easy to say which model is more suitable. Where moment based methods suffer due to the ill-posed *product difference algorithm* which leads to lack of robustness, class based methods require much more computational effort. Therefore, evaluating the discretization techniques and numerical solutions with respect to robustness and computational efficiency is one of our objectives.

In the literature, there are several noticeable breakup and coalescence models to close the PBE and these closures are very often named as breakage kernel and coalescence kernel. The two competing mechanisms finally lead the distribution to a certain dynamic equilibrium at which the bubbles continuously breakup and coalesce, yet the size distribution of the bubbles remains the same. Thus, it is important to have compatible kernels for coalescence and breakage. If one of these kernels is dominant with respect to the other, the achieved equilibrium distribution can be unrealistic, or the achievement of an equilibrium distribution can be unrealistic. Therefore, the breakage and coalescence kernels are usually modeled together. Chen and his co-workers studied the effect of different breakage and coalescence closures and they showed that incompatible kernels produce poor results [12]. Certain experimental and theoretical models for breakage and coalescence kernels are regarded as milestones for the evolution of population balances in the framework of gas/liquid–liquid dispersed phase systems and the development of these models is presented in detail by Jakobsen [13].

Most of the present models for coalescence kernels were derived analogously to the kinetic theory of gases [15–18]. In kinetic theory of gases, collisions between molecules are considered while in the process of coalescence, bubble–bubble and bubble–eddy collisions count. Thus, various coalescence models show similar trends, that is a monotonous increase in the specific coalescence rate with increase in the bubble diameter [19]. The coalescence kernel function adopted in this work is the one proposed by Lehr et al. [20] which is implemented according to the technique developed by Buwa and Ranade [19] and improved by an additional term to reduce the coalescence rate for high holdup values of the secondary phase.

In the case of breakup, most of the published studies on bubble breakup are derived from the theories which are outlined by Hinze [21] and Kolmogorov [22]. All these models have their own advantages and weak points which make them dramatically different. Nevertheless, they have similar phenomenological interpretations: bubble breakage occurs due to turbulent eddies colliding with the bubble surface. If the energy of the incoming eddy is higher than the surface energy, deformation of the surface happens, which may result in breakup of a bubble into two or more daughter bubbles. The colliding eddies that are larger than the bubble result in spatial transportation. Thus, collisions between bubble and eddies being smaller than or equal in size to the bubble give rise to breakage.

The main differences among the available breakage kernels are due to their predictions of daughter size distributions (DSD). Some of the models assume a uniform or a truncated normal distribution which is centered at the half of the bubble size. In other words these models are based on the assumption of equal-sized breakage [23, 25, 26]. In contrast, some others presume unequal

breakup which means a bubble/droplet breaking into a large and a smaller one [16, 23, 27]. The developed model by Lehr et al. [28] is able to combine the features of these significantly different breakage closures. Their model is based on the theoretical findings of Luo and Svendsen [27]. The breakage kernel is derived from the frequency of arriving eddies onto the surface of a bubble and from the probability that collisions lead to breakage. Accordingly, their model predicts an equal-sized breakage for relatively small bubbles and an unequal-sized breakage for large ones. In fact, their approach appears even intuitively to be reasonable: large bubbles firstly collide with large turbulent eddies so that a large and a smaller daughter bubble exist while for small bubbles equal-sized breakage is easier due to high interfacial forces (large and small are relative to stable bubble size under given conditions). A comprehensive comparison of the noticeable coalescence and breakage models is given by Wang et al. [29]. The comparison shows that the model proposed by Lehr et al. [20] is generally superior to other available breakup closures which makes it a suitable candidate for the choice of our breakage kernels.

The breakage and coalescence kernels are the first terms which exhibit the coupling between PBE and CFD. In the formulation of these kernels, there are variables which has to be obtained from the numerical solution of flow problems. The kernels require fluid dynamic variables, e.g., turbulent kinetic energy, turbulent dissipation rate, etc. When the coupled system of governing equations is broken down in *Chapter 2*, all the existing couplings will be analyzed. However, even if the problem is solved in 0D (ideal Stirred Tank Reactor), the variables from computations of fluid dynamics appear. Therefore, in order to solve the PBE one always needs accurate CFD results.

The dynamics of multiphase flows has been a very interesting topic to researchers in the field of CFD for the last several decades and many different methods have been developed. Numerical simulations which assume the dispersed flows to be laminar are not able to produce mesh independent results. The finer the grid, the more vortices are resolved. That is more typical for turbulent flows. Turbulence models which are applicable to produce results with an acceptable accuracy and reasonable computational cost generally originate from the family of two-equation eddy viscosity models. The most preferred model in this sense is related to the standard or modified $k-\varepsilon$ turbulence models which have been implemented in several commercial CFD programs and in-house codes, including FEATFLOW.

FEATFLOW is an open source, multipurpose CFD software package which was firstly developed as a part of the FEAT project at the University of Heidelberg in beginning of the 1990s based on the Fortran77 finite element packages FEAT2D and FEAT3D (see *http://www.featflow.de*). FEATFLOW is both a user oriented as well as general purpose subroutine system which uses the finite element method (FEM) on unstructured (block-structured) quadrilateral (in 2D) and hexahedral (in 3D) meshes. Multilevel Pressure Schur Complement techniques are employed to handle pressure–velocity coupling in Navier-Stokes equations. First, the time discretization is performed with one of available techniques (Forward–Euler, Backward–Euler, Crank–Nicholson or Fractional–step–θ–scheme) then, the spatial discretization is carried out by finite elements with nonconforming parametric/nonparametric rotated bilinear/trilinear shape functions for velocities and piecewise constant approximation for the pressure. The resulting linearized discrete systems of equations are solved with a geometric multigrid solver accelerated by Incomplete Lower Upper (ILU) factorization technique. Coarse grid problems are treated within preconditioned Richardson iterative method for which the preconditioners are chosen from Krylov space methods like, conjugate gradient (CG) method, the BiCGSTAB. FEATFLOW is being developed with new numerical methods and various applications at TU Dortmund by Turek and his coworkers.

In most of the present studies which consider the implementation of CFD coupled with PBE, it is preferred to work with commercial codes like FLUENT [12, 30–32] or CFX [19, 20, 28, 33], naming just two of the most important CFD software packages. However, a commercial code is not the only option, and open-source software packages such as FEATFLOW possess the advantages of higher flexibility and robustness. FEATFLOW has already been extended with many additional modules such as turbulence model [34], multiphase model [4], subgrid-scale mixing model [35], and will be extended with population balance models within this study.

In our approach, the transport problem of bubbles is a pure unsteady convection problem which is particularly difficult to solve and exhibits challenging numerical problems as stabilization of convective term with introducing the least possible or no numerical diffusion to solution. However, when the unresolved subgrid features of the flow are modeled in a Reynolds Averaged Navier-Stokes fashion, the diffusive term consequently appears due to turbulent viscosity. Then, the problem is not anymore the solution of a hyperbolic equation but it is the solution of a parabolic PDE describing nonlinear unsteady convection-diffusion-reaction model. The design of the required computational tools with adequate numerical methods and combining them in order to solve the resulting system of integro-differential equations is another objective of this study.

Analytical solutions of PBE are limited to very few cases. The solution of PBE for dispersed phase systems involves an inevitable coupling of PBE and turbulent flow dynamics which can lead to unreasonable computational cost and many difficulties in numerics if the problem is not tackled properly. The aim of this thesis is to propose numerical solution strategies to these challenging problems and develop an efficient and robust computational tool to solve arising coupled system of integro-differential and differential equations in the framework of gas/liquid–liquid dispersed phase systems.

In *Chapter 2*, an overview of governing equations and the couplings will be presented; then, the possible simplifications are discussed to obtain subproblems which are of use while studying the solution of coupled PBE–CFD models: *(i)* ideal stirred tank reactors, 0D problem *(ii)* steady flow in a channel, 1D problem *(iii)* one-way coupled PBE–CFD problem, solution of PBE for a dispersed pipe-flow and on a quasi-steady 3D flow field through a static mixer, *(iv)* two-way coupled PBE–CFD problem, solution of PBE in the framework of bubble column reactors. Solution of the first subproblem is presented with a detailed discussion on PBE in *Chapter 3*; moreover, this chapter is also focused on to validate and to verify our implementations. *Chapter 4* and *Chapter 5* investigate the solution of the one-way coupled (*(ii)* and *(iii)*) and the two-way coupled (*(iv)*) PBE-CFD problems respectively.

2

Mathematical Model and Numerics

This chapter presents the governing equations of the dispersed phase system and discusses the numerical solution of coupled PBE–CFD models. First, we will give an overview to the solution of our final problem: *population balances of gas/liquid–liquid dispersed phase systems in time and space*; then, the subproblems are formulated in order to investigate and discuss the different aspects of the problem, and to analyze the numerical behavior of the chosen methods for the different parts. These problems present a guideline to this research; so that, an accurate and computationally affordable mathematical model can be established, and the required numerical methods for the solution of the model can be investigated.

2.1. Overview

The research for population balances of dispersed phase systems has focused two initially-distinct fields: modeling of coalescence and breakup kernels, and CFD studies on the dispersed phase flows. The solution of coupled models has been studied for the last two decades, thanks to development in computer technologies and boosted compute powers [36]. Lo [37] presented in 1996 the first computational results of coupled PBE–CFD model for bubbly flows; and, there has been a growing interest in this new field: modeling and numerical studies of dispersed flows within a coupled PBE–CFD approach. Jakobsen et al. provided a comprehensive review [13] of the studies in this field which covers the studies up to the middle of the last decade, and a more up to date review is presented by Cheung et al. [38] covering the last decade as well.

An attempt to understand the population balance of bubbles or droplets in a continuous phase, requires the solution of the transport problem which is both in the *external coordinate* and in the *internal coordinate* described with the following hyperbolic transport equation whose right hand side (RHS) is implicitly written for the moment;

$$\frac{\partial f}{\partial t} + \mathbf{u}_g \cdot \nabla f \;=\; s, \tag{2.1.1}$$

where f is the number density probability function. Equation (2.1.1) describes a purely convective transport in the external coordinate; indeed equation (2.1.1) holds, if the population balance of the dispersed phase is subject to laminar flow. However, in the population balance of bubbles[1] the flow regime of interest is often turbulent. Should the turbulence be modeled with one of the two-equation eddy viscosity model such as standard $k-\varepsilon$ model in a RANS fashion, a diffusive term appears and the governing equation is not anymore a hyperbolic transport equation but an unsteady second order PDE which should be solved with the appropriate modeling of the RHS

$$\frac{\partial f}{\partial t} + \mathbf{u}_g \cdot \nabla f - \nabla \cdot \frac{\nu_T}{\sigma_T} \nabla f \;=\; B^+ + B^- + C^+ + C^-. \tag{2.1.2}$$

When the stationary counterparts of this type PDEs are elliptic, as in the case of equation (2.1.2), these equations are of parabolic type. Nevertheless, if there is a distinct direction of advection and if the diffusion is negligibly small in this direction, the steady convection-diffusion-reaction equation can be rewritten as a hyperbolic transport equation, a detailed discussion is given by Kuzmin [39]. The terms on the RHS of equation (2.1.2) are source and sink due to bubble coalescence and breakup which needs to be modeled with PBE; then, it leads to

$$\begin{aligned}\frac{\partial f}{\partial t} + \mathbf{u} \cdot \nabla f - \nabla \cdot \frac{\nu_T}{\sigma_T} \nabla f \;=\; & \int_{\upsilon}^{\infty} r^B(\upsilon, \tilde{\upsilon}) f(\tilde{\upsilon})\, d\tilde{\upsilon} - \frac{f(\upsilon)}{\upsilon} \int_0^{\upsilon} \tilde{\upsilon} r^B(\tilde{\upsilon}, \upsilon)\, d\tilde{\upsilon} \\ & + \frac{1}{2} \int_0^{\upsilon} r^C(\tilde{\upsilon}, \upsilon - \tilde{\upsilon}) f(\tilde{\upsilon}) f(\upsilon - \tilde{\upsilon})\, d\tilde{\upsilon} - f(\upsilon) \int_0^{\infty} r^C(\tilde{\upsilon}, \upsilon) f(\tilde{\upsilon})\, d\tilde{\upsilon}. \end{aligned} \tag{2.1.3}$$

Finally, we could write down the complete governing equation describing the transport of bubbles, which is an integro-PDE and needs to be numerically treated very carefully in order to obtain results with a desired accuracy and in an affordable computational cost. The right hand side of equation (2.1.3) is the source and sink terms of the transport problem in the external coordinate due to transport of bubbles in the internal coordinate, e.g. size coordinate. The equation (2.1.3) involves all the terms which exhibit the coupling between turbulent fluid dynamics and PBE: velocity field of the dispersed phase ($\mathbf{u}$), turbulent viscosity (ν_T) and the breakage and coalescence kernels, denoted with r^C and r^B respectively. These terms require the solution of a turbulent flow problem and cause the system to be coupled to the Navier-Stokes equations and a turbulence model. The complete model with all external and internal couplings can be schematically given as in Figure 2.1.

The presented model is highly nonlinear due to all these couplings sketched in Figure 2.1. On the other hand, the couplings for lean liquid–liquid dispersions can be much weaker relative to the ones for gas–liquid dispersions such that the first system exhibits much less nonlinearity than the later does; based on this fact, the mathematical model and the solution strategies can alter. Therefore, it is not reasonable having an attempt to solve the complete model before analyzing the existing couplings in terms of modeling and numerics, and this can be realized by formulating subproblems.

[1] Unless it is explicitly stated, bubble also refers to droplet in the context of this chapter, but not the other way around. It is needed to adopt this convention due to readability purposes.

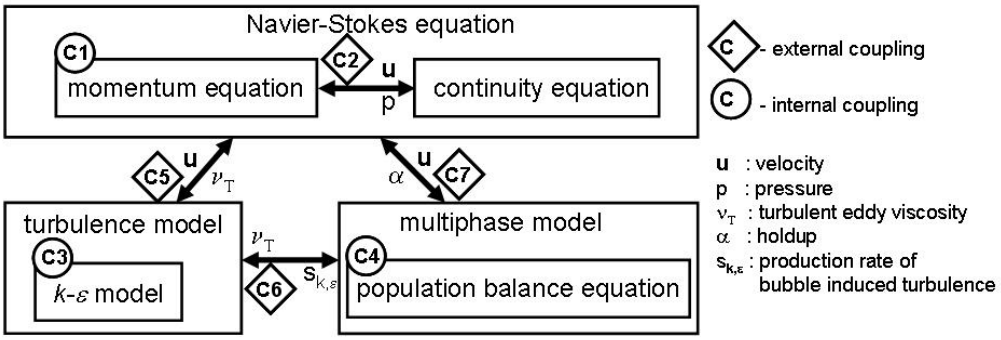

Figure 2.1: Sketch of the coupling effects inside the complete model.

2.2. Subproblems

The population balance equation for gas–liquid (liquid–liquid) flows, equation (2.1.3), is a transport equation for the number density probability function, f, of bubbles (droplets). By definition, f needs to be related to an internal coordinate, what in most of the cases is the volume or size of bubbles, υ. The transport of f can be basically described with two distinct but coupled phenomena:

- the turbulent flow field,
- the population balance of the dispersed phase.

It is possible to analyze the transport problem of f, which is described with equation (2.1.3) and schematically explained in Figure 2.1, with several assumptions such that the phenomena are not any more associated and the problem is divided into subproblems:

i) 0D problem: ideal stirred tank reactor (STR),
ii) 1D problem: solution of PBE with a steady flow in a channel,
iii) 3D problem: solution of PBE with a quasi-steady 3D flow field.

The solution of each set of governing equations describing our coupled model will involve some uncertainties and errors in the results due to the adopted closures of the mathematical model and employed numerical techniques. Studying these subproblems provides a basis where we can analyze the solution of each possibly decoupled model, i.e. solution of the turbulent flow dynamics and solution of the population balances, so that the external and internal couplings in Figure 2.1 are analyzed and the appropriate modeling approaches and numerical methods are determined for the solution of our final problem:

> *Solution of PBE for gas–liquid dispersed systems in the framework of bubble column reactors.*

The first subproblem, namely 0D problem, is our "play ground" to study the solution of PBEs for ideal STR. In the ideal STR, the dispersed phase system is homogeneously stirred and the dispersion does not exhibit any spatial variation; therefore, the transport problem in the external coordinate, i.e. the equations regarding the external couplings *C6* and *C7*, and the solution of multiphase model concerning the internal coupling *C4* (Figure 2.1) is not necessary; only, the solution of PBE is required to obtain the evolution of the size distribution of the secondary phase. So, the transport equation of f reduces to

$$\frac{df}{dt} = \int_{\upsilon}^{\infty} r^B(\upsilon,\tilde{\upsilon}) f(\tilde{\upsilon})\, d\tilde{\upsilon} - \frac{f(\upsilon)}{\upsilon}\int_0^{\upsilon} \tilde{\upsilon} r^B(\tilde{\upsilon},\upsilon)\, d\tilde{\upsilon} + \frac{1}{2}\int_0^{\upsilon} r^C(\tilde{\upsilon},\upsilon-\tilde{\upsilon}) f(\tilde{\upsilon}) f(\upsilon-\tilde{\upsilon})\, d\tilde{\upsilon} - f(\upsilon)\int_0^{\infty} r^C(\tilde{\upsilon},\upsilon) f(\tilde{\upsilon})\, d\tilde{\upsilon}. \quad (2.2.1)$$

This subproblem offers advantages of studying the numerical methods related to only PBE and the closures of the PBE (the coalescence and breakage kernels) independent of the fluid dynamics.

The numerical methods which have been developed for the solution of PBE are initially studied independent of the external transport problem; the solution of PBE with the transport in the external coordinate is the later step which is firstly achieved by Lo in 1996 [36].

Lo adopted a class based method for the discretization of PBE and called it MUSIG (Multi Size Group) model [37], the class based method was originally developed for the solution of PBE in 0D. Therefore, first we will study the discretization of PBE (2.2.1) in time and internal coordinate with several hypothetical and physical closures of PBE.

There is no benchmark or validation study (up to the author's knowledge) to test the solution of PBE with physical kernels for a full 3D problem which we desire to accomplish. Therefore, after determining the appropriate numerical methods and closures of PBE, we need to test the employed methods, e.g. time discretization schemes, stabilization scheme; without any additional uncertainties associated to turbulent flow dynamics. Consequently, a one-dimensional model problem in 3D is formulated based on the assumptions:

- **u** is known, constant in space and time, and aligned with one of the coordinate axes (say, x);
- there is no diffusion;
- the kernels are either independent of turbulent variables, or they are known and have the same value in the whole computational domain;
- cases with pure coalescence or breakage exist.

Then, an unsteady formulation of this problem is described with the following nonlinear hyperbolic transport equation,

$$\frac{\partial f}{\partial t}+\mathbf{u}\cdot\nabla f = \int_{\upsilon}^{\infty} r^{B}(\upsilon,\tilde{\upsilon})f(\tilde{\upsilon})\,d\tilde{\upsilon}-\frac{f(\upsilon)}{\upsilon}\int_{0}^{\upsilon}\tilde{\upsilon}r^{B}(\tilde{\upsilon},\upsilon)\,d\tilde{\upsilon} + \frac{1}{2}\int_{0}^{\upsilon} r^{C}(\tilde{\upsilon},\upsilon-\tilde{\upsilon})f(\tilde{\upsilon})f(\upsilon-\tilde{\upsilon})\,d\tilde{\upsilon}-f(\upsilon)\int_{0}^{\infty} r^{C}(\tilde{\upsilon},\upsilon)f(\tilde{\upsilon})\,d\tilde{\upsilon}. \quad (2.2.2)$$

Furthermore, one can immediately see that based on the first assumption the steady version of equation (2.2.2) is analogous to equation (2.2.1), as it is done in the study by Silva et al. [40]. So that, equation (2.2.2) can be rewritten:

$$u_x\frac{df}{dx} = \frac{df}{dt} = \int_{\upsilon}^{\infty} r^{B}(\upsilon,\tilde{\upsilon})f(\tilde{\upsilon})\,d\tilde{\upsilon}-\frac{f(\upsilon)}{\upsilon}\int_{0}^{\upsilon}\tilde{\upsilon}r^{B}(\tilde{\upsilon},\upsilon)\,d\tilde{\upsilon} + \frac{1}{2}\int_{0}^{\upsilon} r^{C}(\tilde{\upsilon},\upsilon-\tilde{\upsilon})f(\tilde{\upsilon})f(\upsilon-\tilde{\upsilon})\,d\tilde{\upsilon}-f(\upsilon)\int_{0}^{\infty} r^{C}(\tilde{\upsilon},\upsilon)f(\tilde{\upsilon})\,d\tilde{\upsilon}. \quad (2.2.3)$$

Equation (2.2.3) says that time dependent 0D-PBE and constant velocity 1D-PBE are equal. So that, for the cases which have an analytical solution of PBE, the accuracy of the employed numerical schemes to discretize the convective terms can be studied. And with the last assumption, it is possible to see how accurately the coalescence and breakage integrals are calculated being independent of each other. Once the implementation of the employed kernels and numerical schemes is validated and verified by comparing the obtained results against the analytical solutions and the available results in the literature, we are ready to progress to the solution of PBE coupled to turbulent fluid dynamics.

The computational tools which are developed for the numerical simulation of multiphase problem require extreme computational costs and stability problems arise due to external couplings:

C5, *C6* and *C7* (see Figure 2.1). These couplings are very strong and exhibit nonlinearities which cause stability problems during numerical computations. Furthermore, employing inappropriate numerical schemes results in numerical instabilities. Then, instead of tackling the complete problem being described with the model in Figure 2.1, we formulate a simplified mathematical model describing the evolution of liquid-liquid dispersions in turbulent flows with the following assumptions:

- Physical properties as the viscosity and the density of the primary- and the secondary-phase are similar.
- A quasi-stationary solution of turbulent flow field exists.

The first assumption says that the momentum exchange between the phases is negligible and the phases share the same momentum field so that the problem is reduced to single phase problem from the point of the Navier-Stokes equations and the turbulence model, i.e. fluid dynamics part. That is to say, the *C7* external coupling and the *C4* internal coupling are canceled so these models are called as one-way coupled PBE-CFD models.

One-way coupled PBE-CFD models offer the advantage of analyzing solutions of the PBE for both steady and unsteady flow fields. Since we assumed that the population balance of the dispersed phase has no influence on the fluid dynamics, the PBE are decoupled from the equations of the fluid dynamics; additionally with the second assumption, we are left with the solution of equation (2.1.3) for a given velocity field which is a stationary result of CFD simulations.[2]

The numerical simulation of the oil-water dispersion is a comprehensive case to exploit the one-way coupled PBE-CFD model; and, this is achieved by numerically and experimentally studying the oil-in-water dispersed flows through a static mixer. Nevertheless, first we studied dispersed phase flows in a pipe with hypothetical immiscible liquids whose physical properties are identical to the water. The reason to study turbulent pipe flow is: The accurate steady state result of numerical simulation is available for certain Reynolds number flows [34, 41]. This ensured us that the results involve the possible least error due to the computation of flow field variables; since there was no available experimental or numerical result to compare results of PBE computations for the pipe flow, we numerically and experimentally studied flow through a static mixer with the oil-in-water dispersion of which the density and the viscosity can be assumed to be the same with the water for low holdup values of the secondary phase. With the last case study, it was possible to verify the implemented model and the accordingly developed computational tool.

2.3. Two-way coupled PBE–CFD problems

The last problem to be solved is the dispersed phase flow in bubble columns which is the two-way coupled PBE–CFD problem in this study. The solution requires a clever modeling of the multiphase flow such that the model is comprehensive yet does not lead to excessive computational costs. There are several approaches for modeling of bubbly flows, varying from single-fluid models with a constant gas phase velocity approach to multi-fluid models with PBE, in other words, varying from the most simplified and the least computationally expensive one to the least simplified and the most computationally expensive. The idea is to determine a model which describes the physical phenomena sufficiently accurate and does not lead to excessive computational costs.

Bubbles can have significantly different sizes in bubble column reactors which change by time

[2]Turbulent flows never reach a physical steady-state; however, due to the RANS modeling it is possible to obtain steady numerical solutions for turbulent flows, which corresponds to time averaged quasi-stationary flow.

and in space due to the coalescence and the breakage, i.e. bubbles exhibit a dynamic population-distribution in the internal coordinate; and, bubble sizes have a certain influence on the flow which can not be neglected. Therefore, PBE must be considered in the modeling of the bubbly flows, especially for bubble column reactors. On the other hand, including PBE in the mathematical model requires to model the turbulent fluid dynamics within the multi-fluid approach. Suitable ones are the two-fluid model or the multi-fluid model, depending on the discretization of PBE and how the external coupling *C7* is considered; this point is very crucial regarding the computational effort for solving the developed model.

Independent of which multi-phase model (two-fluid or multi-fluid) is adopted, another difficulty is to decide on the proper modeling of the inter-phase forces which govern the key phenomenon: momentum exchange of the phases. The influential forces are generally considered to be: drag force (f_{D}), lift force (f_{L}) and virtual mass force (f_{VM}). There is no unified formulation of the last two, and most of the available mathematical descriptions of these forces have some empirical/free parameters which are determined by data fitting or for specific studied cases in light of the experimental results.

The only inter-phase force having a widely accepted definition is the drag force which is unfortunately still open due to the drag coefficient (C_D) having many drastically different definitions. The definition of the drag coefficient can be given as a constant function or an intricate function of Reynolds number, it is the most accurately modeled one; and, there are researchers who prefer to include only the drag force in their model (please, refer to *Chapter 5*).

The two-way coupled PBE-CFD model with which we describe the behavior of the dispersed phase system in our problem involves *(i)* Navier-Stokes equations, *(ii)* an extended $k-\varepsilon$ turbulence model, *(iii)* algebraic slip model, *(iv)* drift-flux model: a simplified two-fluid model, *(v)* population balance model. In *Chapter 5*, while we are developing our model by coupling the listed models, we discuss in detail which assumptions are done, which inter-phase forces are considered, and how the nonlinearities are treated. Thus, we aim to have a model describing the dispersed phase system in our problem which is sufficiently accurate and does not require extreme computational effort if the problem is tackled within appropriate numerical approaches.

3

Population Balance Equation

Population balances are concerned with the “particles"[1] dispersed in a continuous phase. The particles are represented with the particle state vector whose components are properties of particles described with continuous and discrete variables. The particle state vector lies in the particle phase space which is spanned by the internal coordinates ($e = [e_1, ..., e_p] \in R^p$) and the external coordinates ($x = [x_1, x_2, x_3]^T \in \Omega \subset R^3$ and time, $t = [0, t_{final}]$), so to identify a particle with only a point in this phase space, i.e. the position of the particle in physical space at a certain time with its characteristics.

Discrete variables of the particle state vector are the discrete characteristics of the particle, e.g., color, density, hardness, surface charge, which are mostly related to the material property of the particles. However, the evolution of the dispersed phase system in time continuously varies and considers the rate of change of particle state variables. Therefore, continuous variables are mostly of interest while analyzing the population balances. Continuous variables can be size, mass, surface area, age, coordinates of point-like particles (external coordinate), etc. Whether the variables of the particle state vector are continuous or discrete, they are always the direct variables of the primary interest. In case of bacterial growth (thinking out of the context), the age of the particles is not a direct interest; nevertheless, it is not possible to have a complete particle state vector without including the age variable. The growth of population is directly related to the age variable. Therefore, the variables of the state vector, either continuous or discrete, strongly depend on the applications. For a more detailed discussion on the particle state vector, the internal and external coordinates, and the discrete and continuous variables of the particle state vector, the reader is referred to the cited studies [2, 5, 43].

In this chapter, we study the population balances of dispersed phase system (gas/liquid–liquid) in the framework of ideal stirred tanks, namely our 0D problem. We will have two main aspects to the solution of the PBE: *(i)* discretization of PBE, *(ii)* closures of PBE.

[1] “Particles" refer to the secondary phase, e.g., bacteria, crystals, polymers, glass beads, bubbles, droplets.

First, regarding the discretization of Equation (2.2.1),

$$\frac{df}{dt} = \int_{\upsilon}^{\infty} r^B(\upsilon,\tilde{\upsilon}) f(\tilde{\upsilon})\, d\tilde{\upsilon} - \frac{f(\upsilon)}{\upsilon}\int_0^{\upsilon} \tilde{\upsilon} r^B(\tilde{\upsilon},\upsilon)\, d\tilde{\upsilon} + \frac{1}{2}\int_0^{\upsilon} r^C(\tilde{\upsilon},\upsilon-\tilde{\upsilon}) f(\tilde{\upsilon}) f(\upsilon-\tilde{\upsilon})\, d\tilde{\upsilon} - f(\upsilon)\int_0^{\infty} r^C(\tilde{\upsilon},\upsilon) f(\tilde{\upsilon})\, d\tilde{\upsilon}$$

it is discussed with a review of available numerical techniques in the literature, and the semi-discrete formulation of Equation (2.2.1) will be presented for the chosen numerical techniques: *method of classes* and *parallel parent daughter classes*. First, the semi-discretized equations are rewritten in-terms of holdup (α) as the internal coordinate, additional to the formulation with volume (υ); and, the equations are discretized in time with classical one-step θ-schemes. Later, we study the closures of PBE, the studies on coalescence and breakage kernels are reviewed and three physical breakage kernels and one coalescence kernel in addition to hypothetical kernels (sum coalescence and erosion) are analyzed.

After the PBE are discretized and closed, 0D problems are solved as numerical tests. We study the influence of time step size and the time-stepping techniques: $\theta = 1$ for the Backward Euler-, $\theta = 0.5$ for the Crank-Nicolson- and $\theta = 0$ for the Forward Euler-scheme. Then, the convergence behavior of different coalescence and breakage kernels are compared with respect to time step size and discretization in the internal coordinate. Finally, in order to verify our implementation the numerical results will be compared with the experimental results. Consequently, we determine the discretization technique and the closures of PBE with which we adopt to solve coupled PBE-CFD problems.

3.1. Numerical solution of the population balance equations

Analytical solutions of PBE are available in very few cases, only depending on the closures and the initial size distributions. The existence of these solutions is discussed in detail by Ramkrishna [2]. The presented idea is to recast PBE such that an equivalent formulation to Fredholm or Volterra integral equations of second kind is obtained which are commonly studied in the mathematical textbooks. In *Section 3.4.1*, we present a case having an analytical solution which was obtained by McCoy and Madras [42]; however, here we consider the solution of PBE in cases for which analytical solutions are not available, and we need numerical techniques to discretize PBE in order to obtain the desired solution. In the context of this chapter, the population balances of dispersed phase systems are described with equation (2.2.1), and the discretization of this equation is achieved in the internal coordinate and in time.

3.1.1. Discretization in the internal coordinate

The internal coordinates help us to distinguish individuals of the secondary phase, e.g., droplets, bubbles, with respect to properties of interest. Internal coordinates can be dependent as in the case of the size and the volume of spherical droplets – in case of the constant density even the mass –, all these internal coordinates are related; if one of these variables is given in the physical state, it is sufficient to identify the other properties.

The choice of variables defining the internal coordinate strongly depends on the application

and is a restriction on numerical techniques which can be employed. In the choice of the discretization technique, it is important *(i)* which dynamics of the population appears, e.g., coalescence, breakage, nucleation, growth, *(ii)* which properties of interest are given in the particle state vector.

Let us slightly digress to give a clear picture about these two criteria and consider the PBE of a crystallization process. In the crystallization process, the key dynamics of the population to be modeled is the growth: once the concentration of the crystal molecule is above a threshold value (saturation concentration), crystals nucleate and grow. This phenomenon is added to population balance models as a convection in the internal coordinate (size coordinate). Then, for ideal STR, the governing equation is not anymore equation (2.2.1) but it is a one-dimensional, in internal coordinate, integro-partial-differential equation of the hyperbolic type. And the arising convective term due to the growth requires special care while being discretized. So, a low order method which fits to the purpose of discretization of governing equation for bubble dynamics will be a poor choice for the solution of mathematical models describing the crystallization process. Moreover, if one wants to model the population dynamics of the crystallization process with more than one property, an appropriate discretization technique for multivariate PBE has to be employed. It is worth to mention here that in the study of bubble dynamics for ideal stirred tanks (reactors), the interesting characteristics of the secondary phase are diameter, surface area, volume and mass; however, all these variables are related to each other since bubbles are assumed to be spherical, and it is sufficient to identify the secondary phase with one of them. Through this thesis, we will interchangeably adopt the diameter and the volume as the internal coordinate, depending on the convenience. Therefore in the governing equation (2.2.1) we have only one internal coordinate which needs to be discretized.

The discretization methods can be first categorized with respect to the PBE: multivariate PBE and one-dimensional PBE. When multivariate population balance equations are considered, there is no single numerical method which applies to all. The number density distribution of the secondary phase is described with more than one variable as age, volume, size, concentration. In (wet) granulation, a particle may be identified with the properties: individual masses of binder, active material, particle size, porosity of granules. For instance, a three-dimensional population balance model of granulation with wetting, nucleation, aggregation and consolidation phenomena is given by Poon et al. [44]. In their study, the three internal coordinates are chosen as the solid volume, liquid volume and gas volume of the granules. Or, in liquid–liquid extraction, a drop is identified with its volume and concentration of solutes within this volume, which leads to a bivariate population balance model, some of the bivariate population balance models can be listed as Boltzmann Equation, granulation by Marshall Jr. et al. [45], sintering by Fox [46] and microbial production of chemicals by Roussos and Kiparissides [47] and anisotropic crystal growth by Briesen [48]. The list can be extended with more studies on modeling of PBE in the bivariate [50–54] and multivariate [55–59] fashions; and they all need to be solved with appropriate numerical methods, e.g., X-discretization by Chauhan et al. [60], bivariate direct quadrature method of moments by Fox [46], a Monte Carlo method by Braumann [58], extended sectional grid technique by Alexopoulos et al. [61], bivariate extension of the Quadrature Method of Moments by Wright et al. [62], Galerkin FEM based discretization by Alexopoulos et al. [63], fast Monte Carlo methods by Irizarry [65, 66], a new framework by Chakraborty and Kumar such that by requiring $n+1$ property of population instead of 2^n the use of triangles (bivariate) and tetrahedral (multivariate) is possible for discretization [67], or a dimension reduction approach by Heineken et al. [68]. Among all these studies and more, the study which focuses on multivariate population balance modeling of bubbly flows by Buffo et al. (2012) [49] is very interesting in the aspect of presenting an outlook for this study.

In this study by Buffo et al. [49], the dynamics of bubbly flows in STR is modeled within an approach of multidimensional population balance model coupled to CFD. Within their approach, they were able to describe the interactions between the continuous liquid phase and the gas bubbles, as well as the interactions among different gas bubbles: the coalescence and break-up phenomena. The internal coordinates chosen as, the bubble velocity, the size, and the composition of bubbles. In order to solve this multivariate PBE they suggest a numerical technique based on the direct quadrature method of moments. Although, the studied problem can be formulated within one-dimensional PBE fashion, as it has been achieved in this study, it can be interesting to adopt their approach to solve the problem and compare the results of these two different methodologies.

When the discretization of one-dimensional PBE is considered, one has to firstly account whether the growth term, i.e. convection in the internal coordinate, arises in the governing equation or does not. The arising difficulties due to the growth term have been already mentioned when the crystallization process has been discussed. Most of the methods providing sufficient accuracy for the numerical solution of population balance models with the breakage and coalescence phenomena will not be accurate enough to solve the models with the growth term. John et al. presented a comprehensive study [69] in which only the nucleation and growth terms are considered in the model, appropriate numerical techniques based on the finite element method are presented to solve the PBE coupled to the Navier-Stokes equations, and they conduct detailed numerical experiments for the validation. This study is another one which presents us a possible direction for further research: Extending our model with the growth and nucleation terms and adopting numerical techniques presented in the study [69] to handle the arising terms so to obtain the numerical solution of a population balance model which involves nucleation, growth, breakage and coalescence.

The approaches to solve one-dimensional PBE can be categorized into three: *(i)* The distribution function is approximated by dividing into finite number of bins and employing polynomials of certain order(s), *(ii)* PBE is averaged according to one internal coordinate, *(iii)* simulation techniques designed to artificially realize the system behavior through the generation of random numbers used for the identification of the probability functions governing the system behavior [2]. Each approach leads to a family of methods; the first approach leads us to methods based on classes, the second points to method of moments and the last one is concerned with the stochastic methods.

Stochastic methods, i.e. Monte Carlo method and its variations, are preferred mostly due to its ability to deal with multivariate and one-dimensional PBE in a relatively less complicated manner, and the numerical solution of the PBE, especially multivariate, gets computationally expensive when these methods are preferred. Stochastic methods are based on the assumption that dynamics of a population (e.g. 10^{12} particles) can be simulated with a representative population which has a much smaller number of particles (e.g. 10^{6}) [70]. These methods can realistically describe the behavior of the population by tracking representative particles which undergo randomly selected events which are nothing else but coalescence and breakup phenomena observed in the real system. The drawback of these methods is: The accuracy of the method strongly depends on the number of particles in the representative population, the greater the number of particles, the more accurate the results will be, on an exponentially increasing computational cost.

Stochastic methods are used to simulate various processes. Firstly, Spielman and Levenspiel [72] used to simulate progress of reactions occurring in the dispersed phase of two-phase systems in backmix reactors; then, in 1981 Ramkrishna [73] provided a comprehensive mathematical background of the stochastic simulation methods and population balance equations. After

this study, a great interest developed in using and improving the stochastic methods to solve PBE. A review of stochastic methods is given in the study by Meimaroglou et al. [70], they compare Monte Carlo and the generalized method of moments. Recently, stochastic methods are used to simulate PBE in a batch stirred tank by Goodson and Kraft [74], nano-particle processes by Zucca et al. [75] and aerosol modeling by Kruis et al. [76]. The last study is one of the very first steps to combining Monte-Carlo based PBE modeling with a CFD model. Nevertheless, considering the required number of representative particles to obtain sufficiently accurate results and the state of art computer technology, it can be concluded that these methods are not yet ready to be fully coupled with CFD for the simulation of coalescence and breakage dominant systems, i.e. simulation of bubbly flows [49].

In the following paragraphs, the review of class based and moment based methods is given with a detailed description of the method of classes with a fixed pivot technique and method of parallel parent daughter classes,

The Method of Classes

The method of classes is the most widely used numerical method from the family of sectional methods. In the context of this thesis, class based methods are used to define the methods which discretize the population balance equations in the internal coordinate, e.g., size, area, volume, mass. Considering "class" as a discrete size range we can define "higher order methods" or "zero order methods" as methods which approximate the continuous particle size distribution with a set of linearly independent functions of high order or zero-order, respectively [77]. High order schemes are mostly preferred for the numerical solution of models describing processes like crystallization (John et al. [69], Wulkow et al. [89]) where the convection in the internal coordinate should be taken into account. Whereas low order methods are mostly preferred to simulate processes which are driven with the breakage and the coalescence, even though they have a tendency to overestimate the resulting particle size distribution.

Sectional methods are developed on the idea which was first suggested by Bleck in 1970 [78] and later by Gelbard and Seinfeld [79]. The population of rain droplets for a finite range is considered to be constant via the use of mean field approximation on the number density [78]; then, the PBE could be written as a set of ordinary differential equations with double integrals which are costly to calculate, and these are considered as the drawback of this method. Later, Hounslow et al. [80] proposed a new discretization technique with the geometrically increasing class width (interval) ($\upsilon_i = 2\upsilon_{i-1}$) which avoids the calculation of double integrals and ensures the mass conservation and the total number of particles being tracked correctly. In the mean time Gelbard and Seinfeld (1978) [79] presented the solution of PBE for droplet coalescence in an ideal stirred tank by employing cubic polynomials on finite elements, as the first study with high order methods. Nevertheless, their method also suffered from the excessive computational load due to the computation of multiple integrals, particularly when the coalescence and breakage kernels also involve integral terms in their formulations. Moreover, the integrands could exhibit singularities causing other difficulties [81].

Hounslow et al. contributed with a major advancement to the numerical solution of the PBE in their study [80]. They were mostly influenced by the study of Batterham et al. [82]. Batterham et al. described the process of coalescence with a system of discretized equations in the internal coordinate. Volume was chosen as the internal coordinate and the discretization is firstly achieved with equidistant intervals, i.e. $\upsilon_{i+1} - \upsilon_i = \upsilon_i - \upsilon_{i-1}$, within this approach it was not feasible to

account for particles with size differences in the order of magnitudes; therefore, the numerical solutions was not providing the satisfactory resolution in the internal coordinate. Then, they introduced the discretization of the internal coordinate such that the notional particle volumes were in a geometric series ($\frac{v_{i+1}}{v_i} = 2$). Nevertheless, particles appearing as a result of coalescence whose volume do not coincide with the values in the series can not be represented with conserving both particle number and particle volume.

Hounslow et al. took over the work from where Batterham et al. had left and proposed a piecewise constant approximation of the particle size distribution over a discretized size domain of which the values follow the geometric series introduced by Batterham et al. Hounslow et al. studied the nucleation, growth and aggregation of calcium oxalate monohydrate crystals (kidney stones). By considering the finite intervals, they were able to simulate the aggregation process in a way that unless two parent particles had the same size, the daughter particle always appears in the size interval of the larger particle and in case of the aggregation of two equal sized parent particles, the daughter particle appears in the next interval. However, due this consideration, the method was able to correctly account only for the changes in particle number but could not conserve the mass. Therefore, a correction factor independent of the kernel was incorporated to the method by enforcing the mass conservation. With respect to how the discrete particle size distribution described, Figure 3.1, their method is the closest to the technique of Kumar and Ramkrishna [83]: *the method of classes*.

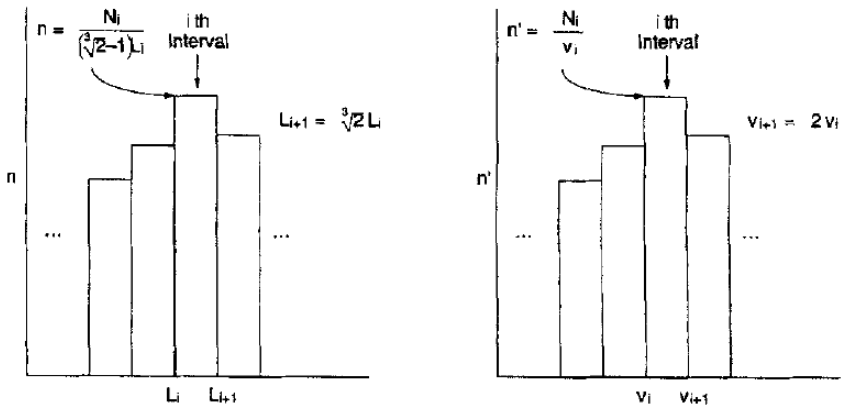

Figure 3.1: Discrete size distributions with length (L) or volume (v) as internal coordinate (Source: Hounslow et al. [80]).

In 1994, Kostoglou and Karabelas had published their study [85] which was about comparing the different numerical techniques for solving PBE. They studied the methods by Batterham et al. [82], Marchal et al. [86], Gelbard et al. [87] and Hounslow et al [80]. The methods are evaluated according to their accuracy and performance by comparing the numerical solutions with analytical solutions for a constant coalescence rate and a sum of arguments coalescence kernel. They concluded that due to the best computational performance additional to conserving both mass and particle number, the method proposed by Hounslow et al. was superior to others [85].

Parallel to the development of the zero-order methods, high-order methods were introduced as an alternative approach. One of the very first studies was presented by Gelbard and Seinfeld in 1978 [79]. They suggested a finite element approach for the discretization of PBE involving the orthogonal collocation methods and cubic polynomials. Later, Nicmanis and Hounslow [88] had an hybrid approach, they combined Galerkin finite element approach with the method suggested

by Gelbard and Seinfeld: the mixed Galerkin and the orthogonal collocation method. Wulkow et al. [89] had a Galerkin finite element approach with h- and p-adaptivity. One of the recent studies is by John et al. [69], they studied the numerical simulation of crystallization process with one-dimensional PBE in 2D space. A high order upwind finite difference method was used to discretize the particle size distribution. The main drawback of the high-order methods is: They require high computational effort due to arising multiple integral terms, especially when the coalescence and breakage kernels involve additional integral expressions in their formulations; although, high-order discretization is not a "must" for these terms but the growth term. Another major difficulty is to decouple the coalescence and the breakage from the variables depending on time [77]; however, Mahoney and Ramkrishna suggested a remedy for this complication within Galerkin's method on finite elements in their study [81]. If it is considered that the difficulties in high-order methods arise due to the breakage and coalescence terms and actually these methods are of use to have a stable scheme for the growth term, it can be concluded that for the solution of PBE involving only the coalescence and breakage terms, high-order methods are not more preferable. For 0D problems, e.g., problem in the study by Wulkow et al. [89], finite elements with h- and p- adaptivity can be considered as an ultimate solution when they are combined with high order stabilization schemes. In problems of the same type exhibiting variation in space, h-adaptivity will be cumbersome, if it is possible at all. Consequently, the numerical solution of PBE for problems of this type is still opened and deserves attention of researchers.

Kumar and Ramkrishna presented their method, the method of classes [83, 84], which was a breakthrough in the numerical solution of PBE, appeared with a novel concept: *internal consistency*. The discrete counterpart of PBE can be reformulated in terms of any moment (property) of the size distribution, and the internal consistency of the employed numerical technique requires that the scheme is conservative for this (these) moment (moments) even if a coarse grid is employed. Kumar and Ramkrishna had firstly suggested the fixed pivot approach [83] with which it was possible to conserve only one moment value; shortly later, they published the moving point approach [84] which was able to conserve desired two properties of the size distribution.

The motivation of Kumar and Ramkrishna was: Unless the internal coordinate was linearly discretized, it was not possible to obtain a grid where all daughter particles coincided with a pivot (representative value of the property on the grid). The main idea of their study reads: When a daughter particle is formed (after the breakage or the coalescence), the daughter particle is assigned to the class whose lower (upper) limit is smaller (larger) than the value of the particle's property and represented by the fixed pivot value, this way it was possible to conserve only one property, e.g., volume, size, number density. With the successor, they were able to conserve two desired properties. If these two properties are taken as volume and number (as it is generally done), the total volume of the remaining parent particles and the appearing daughter particles in the certain class are correctly tracked and the pivot is dynamically adjusted according to these values. This method arose as a remedy to the problem: the fixed pivot approach leads to over-predicted size distributions when it was used on coarse grid and the particle size distribution exhibits steep changes. With the moving pivot approach, they overcome this difficulty such that the pivot moves towards the lower (upper) limit of the class when the number density is sharply decreasing (increasing) and to the center when the change is less steep. They achieved this by solving two sets of equations which describe the conservation of the related properties. This method definitely increased the accuracy by doubling the computational cost; moreover, the realization of the method of classes within moving pivot approach gets very tedious and much more expensive than the first when dispersions with spatial variation are considered [77].

The method of classes was embraced by researchers and was employed to obtain the numerical

solution of the PBE describing many different processes; additionally, numerous studies were done to improve this method. Vanni studied the numerical solution of the PBE for "aggregation-fragmentation" (coalescence-breakage) by adopting 7 different discretization methods of which one was the method of classes with the fixed pivot approach. The others were the methods by Vanni [90], Batterham [82], Hounslow et al. [80], Marchal et al. [86], Lister et al. [91], and Gelbard and Seinfeld [79]. They studied several hypothetical closures (coalescence and breakage kernels) and compared the methods with respect to accuracy, efficiency and robustness. Vanni concluded that the methods developed by Kumar and Ramkrishna, and Gelbard and Seinfeld were superior at all. The comparison criteria and the differences between these two model is presented as: "They are capable of predicting accurately the PSD, the average values and the corresponding uncertainty even in the most ill-conditioned situations. While the implementation of the method by Gelbard is complex and time-consuming, the method by Kumar and Ramkrishna is rather simple" [92]. Consequently, Vanni suggested to employ the method of classes for the numerical solution of general case of coalescence-breakage problems.

Lee et al. [25] studied the numerical simulation of the crystallization process with a combined discretization method: The method of characteristics is combined with the method of classes with a mesh adaptation; Puel et al. [93] use the method of classes to numerically study a bi-modal population balance model describing the crystallization processes; Attarakih et al. also studied PBE with more than one internal coordinate by extending the method of classes for describing the flow dynamics of liquid-liquid extraction contactors [94–96]. Bove et al. suggested a "non-standard method of classes", *parallel parent daughter classes*, and used this method for numerical simulations of bubble columns [9, 97]. Alopaeus and his coworkers contributed remarkable studies, several of which were based on the method of classes as well [98–100], he mostly studied liquid-liquid dispersions in nonideal stirred tanks. Bannari et al. [101] and Selma et al. [102] adopted the method of classes to study the numerical solution of the PBE in the framework of bubble columns. Among these and other available studies, the study of Bove et al. is very interesting, according to us it is a hybrid method of the method of class and the quadrature method of moments, perhaps it is possible to agree with the authors that the method is a "non-standard method of classes" with the description in their study; nevertheless, we will suggest a novel implementation approach so that it shall be considered as a moment based method. Therefore, we analyze this method in more detail in the related section.

Implementation of the method of classes

The discretization of the population balance equation (2.2.1) is carried out by the *method of classes* with the fixed pivot approach (with piecewise constant approximation functions). The fixed pivot volume of the classes is initialized by specifying the particle volume of the smallest "resolved" class $\upsilon_{\min}$ and the discretization factor q, such that

$$\upsilon_i = \upsilon_{\min} q^{i-1} \quad \text{with} \quad i = 1, 2, ...n \tag{3.1.1}$$

where n is the number of classes. The class width $\Delta\upsilon_i$ is defined by the difference of the upper υ_i^U and lower υ_i^L limits of the given class i:

$$\Delta\upsilon_i = \upsilon_i^U - \upsilon_i^L \quad \text{with} \quad \upsilon_i^U = \upsilon_{i+1}^L \quad \text{and} \quad \upsilon_{i-1}^U = \upsilon_i^L. \tag{3.1.2}$$

The limits are fixed and initialized such that in the case of $q = 2$ the pivot volume υ_i is centered in the class

$$\upsilon_i^U = \upsilon_i + \frac{1}{3}(\upsilon_{i+1} - \upsilon_i), \quad \upsilon_i^L = \upsilon_i - \frac{2}{3}(\upsilon_i - \upsilon_{i-1}). \tag{3.1.3}$$

Following equation (3.1.3), the discrete internal coordinate can be sketched as in Figure 3.2.

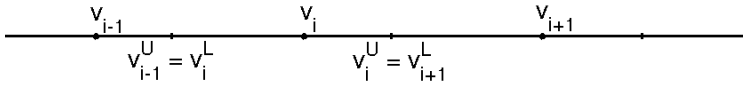

Figure 3.2: Discrete internal coordinate with MC.

The discretized PBE (2.2.1) of the i-th class' number density probability, f_i (i, j and k are class indices), results in

$$\frac{\partial f_i}{\partial t} = \sum_{j=i}^{n} r^B_{i,j} f_j \Delta\upsilon_j - \frac{f_i}{\upsilon_i} \sum_{j=1}^{i} \upsilon_j r^B_{j,i} \Delta\upsilon_j + \frac{1}{2} \sum_{j=1}^{i} r^C_{j,k} f_j f_k \Delta\upsilon_j - f_i \sum_{j=1}^{n} r^C_{j,i} f_j \Delta\upsilon_j$$

$$\text{for} \quad i = 1,2,...n. \quad (3.1.4)$$

The choice of fixed pivot volumes and fixed class widths with piecewise constant approximation functions offers the advantage of expressing the discretized transport equation (3.1.4) in terms of class holdups α_i instead of the number probability density, $f_i = \frac{\alpha_i}{\upsilon_i \Delta\upsilon_i}$ with the following definition of the number density and the holdup of particles having a volume between υ_a and υ_b,

$$N_{ab} = \int_{\upsilon_a}^{\upsilon_b} f \, d\upsilon, \quad \alpha_{ab} = \int_{\upsilon_a}^{\upsilon_b} f\upsilon \, d\upsilon. \quad (3.1.5)$$

Doing so enforces only mass conservation, and the bubble number density is not conservative. Regarding the arising inconsistency we subscribe to the argument of Buwa and Ranade [19], who reported that the difference in the predicted values of interfacial area and Sauter mean bubble diameter obtained with only mass conservation and obtained with mass and bubble number conservation was less than 1%. Multiplying equation (3.1.4) with $\upsilon_i \Delta\upsilon_i$ results in conservative source and sink terms, since the overall gas-holdup can not be changed due to coalescence or breakup procedures[2]. Additionally, any sink (source) term of a given rate associated to a particular breakup or coalescence procedure induces a source (sink) term with the same rate but in a different class. This enables us to assemble only the sink terms while the same contribution is applied to the corresponding source term in the resulting class.

For instance, let us consider a breakup of particles of class i into particles of classes j and k. Such a procedure, obeying to equations (3.1.4) and (3.1.5), leads to the following sink in the i'th class and the sources in the j'th and k'th classes with a zero net flux:

$$\begin{array}{lllll}
i: & -\left(\upsilon_j r^B_{i,j} \Delta\upsilon_j \frac{f_i}{\upsilon_i}\right) \upsilon_i \Delta\upsilon_i \; -\left(\upsilon_k r^B_{i,k} \Delta\upsilon_k \frac{f_i}{\upsilon_i}\right) \upsilon_i \Delta\upsilon_i & = & -r^B_{i,j} \alpha_i \frac{\upsilon_j \Delta\upsilon_j}{\upsilon_i} & -r^B_{i,k} \alpha_i \frac{\upsilon_k \Delta\upsilon_k}{\upsilon_i} \\
j: & +\left(\upsilon_j r^B_{i,j} f_i \Delta\upsilon_i\right) \upsilon_j \Delta\upsilon_j & = & r^B_{i,j} \alpha_i \frac{\upsilon_j \Delta\upsilon_j}{\upsilon_i} & \\
k: & +\left(\upsilon_k r^B_{i,k} f_i \Delta\upsilon_i\right) \upsilon_k \Delta\upsilon_k & = & r^B_{i,k} \alpha_i \frac{\upsilon_k \Delta\upsilon_k}{\upsilon_i} & \\
\Sigma & & = & 0 &
\end{array}$$

where $\upsilon_k = \upsilon_i - \upsilon_j$. However, if we consider the coalescence of particles of the j'th and the k'th class to form particles of the i'th class, to show the conservation of void fraction is a little bit more tricky. The losses in the j'th and k'th classes due to coalescence with each other are as follows:

$$\begin{aligned}
j: & \quad -\left(f_j r^C_{j,k} f_k \Delta\upsilon_k\right) \upsilon_j \Delta\upsilon_j = -r^C_{j,k} \alpha_j f_k \Delta\upsilon_k \\
k: & \quad -\left(f_k r^C_{k,j} f_j \Delta\upsilon_j\right) \upsilon_k \Delta\upsilon_k = -r^C_{k,j} \alpha_k f_j \Delta\upsilon_j
\end{aligned}$$

[2]Note that we assume incompressible conditions for bubbles.

The gain in the i'th class due to coalescence of the k'th and j'th classes is:

$$i: \quad \tfrac{1}{2}\left(r^C_{j,k} f_j f_k \Delta\upsilon_j + r^C_{k,j} f_k f_j \Delta\upsilon_k\right) \upsilon_i \Delta\upsilon_i$$

If we assume that the discretization is equidistant, that means $\Delta\upsilon_i = \Delta\upsilon_j = \Delta\upsilon_k$, and recalling that $\upsilon_i = \upsilon_j + \upsilon_k$ then the following relation is obtained

$$\frac{1}{2}\left(r^C_{j,k} f_j f_k \Delta\upsilon_j + r^C_{k,j} f_k f_j \Delta\upsilon_k\right)(\upsilon_j + \upsilon_k)\Delta\upsilon_i = r^C_{j,k}\alpha_j f_k \Delta\upsilon_k + r^C_{k,j}\alpha_k f_j \Delta\upsilon_j$$

which shows that the sink and source terms of coalescence are also conservative in terms of void fraction.

In this study, geometric grids (for the internal coordinate) with varying discretization constants are employed. Therefore, instead of calculating individual sink and source terms due to coalescence, only sink terms for each possible pair of classes are calculated and their sum is added to the resultant bubble class. Accordingly, conservation of mass is enforced from the point of view of coalescence, too.

The above explained implementation strategy of the method of classes does not only enforce the mass conservation but also leads to an efficient computational tool. The coalescence and breakage kernels, $r^C(\upsilon_i, \upsilon_j)$ and $r^B(\upsilon_j, \upsilon_i)$, which can be now described as functions of internal coordinate with fixed pivot volumes, turn out to be constant in time since the pivots are fixed to a certain volume. Therefore, they are calculated and stored at the beginning of the computation and used for the rest. Moreover, since neither breakage nor coalescence necessarily result in the particle volume which coincides with the fixed pivot sizes, a search algorithm has to be implemented to assign the resulting particles after the coalescence and breakage phenomena to the corresponding classes. And, this was also realized as it was done for the calculation of the kernels: At the beginning of computation, coalescence and breakage maps are initialized such that the daughter k'th class as a result of coalescence of i'th and j'th classes is found, as well as in the breakage map, the second daughter, k'th, class is determined as a result of the breakage of the i'th class into j'th, the first, daughter class. Again by taking advantage of the fixed point approach, the breakage and the coalescence maps are initialized for once and all.

As a summary, the method of classes has proven to be a robust and sufficiently accurate numerical method on the cost of high computational demands, especially when the method is employed in CFD simulations (A further discussion will be given in *Chapter 4*.). Hereby, we proposed a strategy to implement the method of classes within the fixed pivot approach, which results in a highly robust and relatively efficient computational tool and in the need of accuracy for coarse meshes due to conservation of only one particle property. Therefore, the arising objective is to determine the approximate discretization constant and the corresponding number of classes such that results are grid independent. This objective is accomplished by studying convergence behavior of the method in 0D problems.

Parallel parent daughter classes

Some of the engineering applications require the properties of the particle size distribution rather than the distribution function itself. Therefore, only the low-order moments of the particle size distribution which corresponds to certain physical properties of the population are considered to be interesting and sufficient for these engineering applications. The moment based method arose as

an effort to reduce the computational cost and to increase the accuracy of the numerical solution of PBE for the specified low order moment of the particle size distribution which are of interest. The evolution of the methods follows as, the method of moments, the quadrature method of moments, direct quadrature method of moments and their variations.

The main idea of the moment based method is to track the certain properties of the particle size distribution instead of tracking the evaluation of the distribution itself. When the distribution is evaluated as a function of size, the low-order integer moments (Equation (3.1.6)) correspond to certain physical properties, e.g. $k = 0$ for total number density, $k = 1$ for total size density, $k = 2$ for total surface density, $k = 3$ for total volume density:

$$m_k = \int_0^\infty f(x)x^k dx \qquad k \in \mathbb{N} \tag{3.1.6}$$

The ratio of some of these moments corresponds to useful variables of the population, e.g., ratio of the third order moment to the second corresponds to the Sauter mean diameter of the population: $d_{32} = \frac{m_3}{m_2}$. The moments, i.e. the integral properties of the particle size distribution, are tracked accurately to the steady state and the final particle size distribution is reconstructed from these values.

Case studies which do not show spatial variation, ideal stirred tanks, exhibits a very suitable framework for the moment based methods. Since the moment values are very accurately tracked in time, depending on the mathematical model and its closures even exactly, the variables which are of interest, e.g. interfacial area density (very important for heat and mass transfer), can be directly calculated. However, if one is interested in the actual size distribution of the population, then the distribution function has to be obtained from the available moments with appropriate reconstruction methods and this is one of the main difficulties within in these methods.

The moment based methods convert equation (2.2.1) into a set of differential equations by integrating both sides of the equation with respect to the internal coordinate according to equation (3.1.6) which results in

$$\frac{\partial m_k}{\partial t} = \int_0^\infty (G^+ + C^+ + C^-)x^k dx \tag{3.1.7}$$

with the implicit definition of the source and sink terms. The characteristics of the growth and coalescence kernels, i.e. formulation of $G^+ + C^+ + C^-$, determines whether equation (3.1.7) is closed or not. And, it can be immediately concluded that this exhibits a limitation for the numerical solution of general case of coalescence-breakage problems. However, the closure problem holding for the equation (3.1.7) can be easily relaxed by adopting the quadrature approximation. Consequently, moment based methods, with this approximation, were proposed as *Quadrature Method of Moments* (QMOM) and in this respect, it can be considered as generalization of standard method of moments.

The (standard) method of moments (MOM) has been used as a powerful numerical tool to solve the PBE with the advantage of describing dynamics of the population with nucleation, growth and coalescence. The MOM established the concept for the methods which were based on tracking the evolution of properties of the population rather than the size distribution. It has been successfully used to numerically simulate aerosol dynamics by, e.g., McGraw and Saunders [103], Frenklach and Harris [104], Pratsinis [105], and crystallization processes by, e.g., Melikhov and Berliner [106], Wey [107], Nagy et al. [108]. Hulburt and Katz [5] extended the use of MOM by working with two internal coordinates in order to describe the dynamics of non-spherical particles.

The MOM could have found a wider area of application unless the closure requirement of

the method had been so severe. The method accomplishes its objective by formulating equations for evolution of the moments in the closed form that is more likely to obtain for mathematical models describing aerosol dynamics and crystallization processes with only growth phenomenon, and, rarely, coalescence and growth phenomena together. Fortunately, there are certain cases of interest in which the first low-order moments can be written in the closed form or the unknown size distribution can be approximated with a predefined distribution. For constant or linear growth kernels, $\phi(x) = a + bx$, as it is studied by Hulburt and Katz, and McGraw and Saunders [5, 103], the moment equations are in the closed form; however, when a more complex growth kernel is used or the coalescence is needed to be incorporated into the model, a predefined size distribution in the form of, e.g., log-normal distribution, gamma distribution, must be employed as in these studies [5, 109, 110]. In some other cases the resulting moment equations can be closed with an interpolative closure method as Franklach et al., and Deimer et al. have done in their studies [104, 111, 112]. Even though with these tricks the MOM widen the area of application, it has yet not been possible to adopt the MOM to numerically solve the general PBE; therefore, generalized moment methods have been developed to overcome the difficulties concerned with the closure of moment equations.

The first study which is considered as one of generalized moment methods was presented by McGraw for a dispersed system which involves only the nucleation and the growth, *Quadrature Method of Moments* [7]. The QMOM is based on an approximated closure, quadrature-based closure, rather than the exact closure in the case of MOM so it is possible to apply the method to a wider range of problems. The main idea of the approximated closure is that the abscissas, x_i, and weights, w_i, can be directly determined from the low-order moments of the unknown distribution function, $f(x)$, i.e. there is no dependence of x_i and w_i on the size distribution and kernels. With n-point Gaussian quadrature we can rewrite the equation (3.1.6) as,

$$m_k = \int_0^\infty f(x)x^k dx = \sum_{i=1}^{n} x_i^k w_i \,, \qquad k = 0, 1, ...2n-1. \tag{3.1.8}$$

For the first $2n$ moments we obtain $2n$ nonlinear algebraic equation of which the solution will be n abscissas and the corresponding weights. The solution of this type of equation would require a nonlinear search and would be computationally too expensive, instead the algorithm proposed by Gordon [14] in 1967 was employed, *product-difference algorithm*. The solution strategy to obtain the abscissas and the weights involves the solution of an eigenvalue problem for the symmetric tridiagonal Jacobi matrix constructed from the sequence of moments by using the product-difference algorithm. This matrix has to be positive definite so that the solution, x_i and w_i, is found in $\mathbb{R}^+ \bigcup 0$; however, this may not be so for problems involving spatial transport of the moment which is discussed later when the one-way coupled PBE-CFD model is analyzed in the next chapter. As a summary, the QMOM was developed to calculate the growth contribution was based on the idea: The n-point quadrature approximation of the distribution function can be obtained from the first $2n$ moments by means of product difference algorithm and the growth contribution to moments can be easily calculated by the known abscissas and weights.

The QMOM found a wide area of application, the method first extended to numerically simulate the growth and coalescence phenomena in the study by Barret and Webb [113] and later, the QMOM has beem improved to be applied to systems involving breakage and coalescence by Marchisio et al. [115].

Marchisio et al. firstly studied the numerical simulation of precipitation process with fluid dynamics, in their study [114] they considered only the growth and coalescence phenomena and showed that QMOM is computationally affordable and an accurate method for problems of this

type. Then, they extended their study including breakage, as well. They had many numerical tests with several different hypothetical breakage and coalescence kernels and compared the solutions obtained with QMOM to "the rigorous solution" which was presented by Vanni [92]. They found results to be very satisfactory; then, they employed QMOM to numerically solve PBE coupled to fluid dynamics in their next study [116] in which they implemented QMOM into a commercial CFD software package, FLUENT, to numerically simulate simultaneous aggregation-breakage in turbulent Taylor-Couette flow. They employed relatively simple coalescence (Brownian kernel) and breakage (power-law and exponential breakage kernels) kernels which make the implementation of the QMOM more straightforward. They successfully achieved the numerical simulation of the process and verified their results by comparing with experiments.

QMOM was shown to be a strong numerical tool to simulate simultaneous coalescence–breakage with fluid dynamics by Marchisio et al. [116]. However, they also presented that QMOM exhibits two strong drawbacks[3]: *(i)* application to the multidimensional PBE is tedious and relatively inefficient, *(ii)* the coupling between the PBE and fluid dynamics is loosened due to assumption of a constant advection velocity for the moments; [117]. In order to establish a remedy, they proposed the direct quadrature method of moments (DQMOM) which suggests to directly track the variables existing in the formulation of the quadrature approximation (abscissas and weights) rather than tracking the moments of the particle size distribution. Nevertheless, for the monovariate case they showed that QMOM and DQMOM leads to the same solution [117]. DQMOM was generally accepted by researchers to numerically solve coupled PBE-CFD problems, therefore the further discussion on this method is left to the relevant chapter, *Chapter 4*.

As the last method to be discussed in this section parallel parent daughter classes (PPDC) will be reviewed. Here, we would like to present only the concept of PPDC, and the details of the method is given when the implementation of the method is presented in the corresponding section. PPDC is categorized as a non-standard method of classes by its developers, Bove et al [97], since it approximates particle size distribution (PSD) as a set of Dirac's delta functions. Nevertheless, it has the same step with QMOM: obtaining the abscissas and weights of the approximated PSD. And, the product-difference algorithm which was suggested by McGraw [7] was also adopted by Bove et al. to solve the ill-conditioned problem: root finding of a polynomial.

This section can be concluded with a common critique for the all moment based methods: the methods of this type leave the *finite-moment problem* opened. After obtaining the final values of the moments, PSD must be reconstructed from a given number of moments and this is severely ill-conditioned problem because of the ill-posedness of the Hausdorff moment problem [118]. The reconstruction of the PSD from a number of given moments is studied in detail by John et al. [119]. He concluded that there is no unified framework to solve this ill-posed inverse problem. The reconstruction by parameter fitting with a predefined shape functions is more accurate and is only possible when the shape of the distribution is known in advance; however, this is the trivial case that is not our interest in this study. The discrete method works for dispersed phase systems involving only the nucleation and growth processes, and the spline reconstruction requires a greater number of moments than the others do. Consequently, the reconstruction problem still remains unsolved; and if one needs the detailed information of the PSD, the moments based methods would not be a wise choice.

[3]These critiques will be further discussed when we are concerned with coupling PBE to CFD.

Implementation of parallel parent daughter classes

PPDC is a recently proposed numerical technique by Bove et al. [97]. Even if Bove et al. define this method as a non-standard method of classes, we can consider it as an hybrid approach of class based and moment based methods as it has the robustness of class based methods and accuracy of the moment based methods.

PPDC suggests to approximate the number density function with quadrature points similar to MC but PPDC requires much less quadrature points. In the study by Bayraktar et al. [1], it was shown that 20-30 classes are required for an accurate approximation of the particle size distribution with MC; whereas in the study by Bove et al., three parent classes are sufficient to have accurate calculations. Since PPDC is presented with all details in the study by Bove [9], it is sufficient to give the necessary definitions and the implementation algorithm so to highlight the outline of this method.

The method is described with certain definitions and properties of the parent and daughter classes. The definitions are taken from the study of Bove [9] since they are necessary to explain the method; the prescribed properties of the classes are only discussed as they can be intuitively deduced.

Definition 1. Parent Classes are those present at time t^n in the unexpanded PSD. They are denoted by abscissas $x_i \in [\upsilon_i, \upsilon_{i+1})$ and weights N_i, with $i = 1, ..., M$.

Definition 2. The i'th breakage daughter classes denoted by abscissas $z_k \in [\upsilon_k, \upsilon_{k+1}) \subseteq [0, x_i)$ with $k = 1, ..., NB(i)$ and weights B_k^i, are classes originated from the i'th parent class having abscissa x_i.

Definition 3. Coalescence daughter classes are denoted by abscissas $y_{ij} \in [0, \infty)$ and weights A_{ij} with $i, j = 1, ..., M$ and $j \geq i$. The coalescence daughter class with double index ij, generated by coalescence of particles from the i'th and j'th parent classes, is coincident with the ji coalescence class. There is no duplication.

With these definitions, it is clear that the change of parent classes are only sink terms as a result of the death events due to breakage and coalescence. Even if the abscissa of a daughter class coincide with one of the parent class', it is not considered as a source term at the corresponding parent class, because the daughter classes after each breakage or coalescence are represented in a distinct internal coordinate which is parallel and may overlap with the internal coordinate of the parent classes. Considering these properties we can conclude that the source terms appear only for the daughter classes in the parallel coordinates and they are not additives.

The numerical treatment of coalescence terms and sink term due to breakage in equation (2.2.1) is straightforward with these definitions and properties; however, how to numerically calculate the source term is neither obvious nor explained in the studies by Bove et al. [9, 97]. The arising difficulty can be explained with ease by using Figure 3.3 which pictures the complete algorithm of PPDC with all the possible processes at time $= t$ according to the given definitions. In Figure 3.3, it is clear that the daughter sizes due to coalescence of parent classes are exactly defined. Nevertheless, the daughter classes due to breakage are unknown and need to be prescribed, which is the loose end of this method.

The algorithm of the PPDC starts with an n-point quadrature approximation of PSD for *M parent classes*,

$$N(\upsilon,t) \cong \sum_{i=1}^{M} N_i(t)\delta(\upsilon - x_i) \tag{3.1.9}$$

where x_i is a quadrature point (size of the i'th parent class) and N_i is the corresponding weight (number density of the i'th parent class). Then, approximated PSD that expands with daughter classes due to breakage and coalescence of particles, i.e. the sink and source terms which are

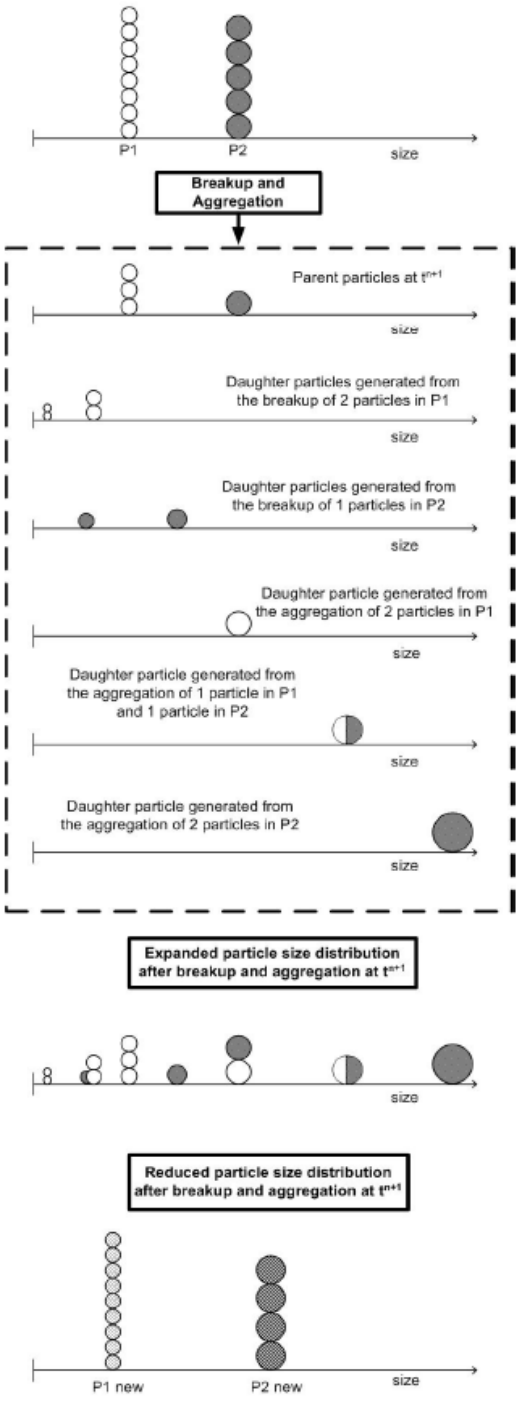

Figure 3.3: PPDC algorithm; source: [9].

calculated according to equations (3.1.10)–(3.1.12), can be given with equation (3.1.13).

$$\frac{\partial N_i(t)}{\partial t} = -N_i(t)\sum_{j=1}^{M} r^C(\upsilon_i,\upsilon_j)N_j(t) - N_i(t)\int_0^{\upsilon_i} r^B(\upsilon_i,\upsilon)d\upsilon \tag{3.1.10}$$

$$\frac{\partial A_{ij}(t)}{\partial t} = (\frac{1}{2}-\delta_{ij})r^C(\upsilon_i,\upsilon_j)N_i(t)N_j(t) \quad \text{for } i,j=1,...,M;\ j\geq i, \tag{3.1.11}$$

$$\frac{\partial B_{ik}(t)}{\partial t} = \gamma(\upsilon_i)N_i(t)N_i(t)\overline{P}(\upsilon_i,\upsilon_k)\int_0^{\upsilon_i} r^B(\upsilon_i,\upsilon)d\upsilon \quad \text{for } i=1,...,M; k=1,...,NB_i\,, \tag{3.1.12}$$

$$N(\upsilon,t) = \underbrace{\sum_{i=1}^{M} N_i(t)\delta(\upsilon-x_i)}_{\textit{parent classes}} + \underbrace{\sum_{i=1}^{M}\sum_{j=1}^{M} A_{ij}(t)\delta(\upsilon-y_{ij})}_{\textit{coalescence daughter classes}} + \underbrace{\sum_{i=1}^{M}\sum_{j=1}^{M} B_k(t)\delta(\upsilon-z_k^{(i)})}_{\textit{breakage daughter classes}}. \tag{3.1.13}$$

Equation (3.1.12) describes the rate of change in the k'th daughter class due to breakage of the i'th parent class by assigning the certain ratio, $P(\upsilon_i,\upsilon_k)$, of the total sink (the second integral term on the right hand side of equation (3.1.10)), in the i'th parent class to the k'th daughter class. The ratio is given by the integral value of all breakage probabilities of υ_i to particles with volume represented by υ_k. Analogously to the method of classes, the $k'th$ daughter class is defined with the pivot size υ_k, and the upper and lower limits υ_k^U and υ_k^L, respectively. Then, $P(\upsilon_i,\upsilon_k)$ is given by $\int_{\upsilon_k^L}^{\upsilon_k^U} p(\upsilon_i/\upsilon)d\upsilon$, where $p(\upsilon_i/\upsilon)$ is the daughter size distribution function and defines the breakup probability of a particle with volume υ_i to particle with volume υ_k under certain conditions. The prescription of daughter classes and the calculation of this integration is a key factor on the accuracy of this method. For the time being, $p(\upsilon_i/\upsilon_k)$ is given as an explicit function of only the ratio of volumes; nevertheless, it is a function of several variables. Since this issue is more related to the modeling of closures, we leave the further discussion to the related section.

The increase in the set of Dirac's functions is cumulative in time; therefore, the expanded PSD should be reduced to the number of parent classes by preserving $2M$ order of moments of the expanded distribution by solving Equation (3.1.14) with the given definition of moment, (3.1.8).

$$\sum_{i=1}^{2M} N_i(t^{n+1})x_i^{(k)}(t^{n+1}) = \sum_{i=1}^{K}\tilde{N}_i(t^n)\tilde{x}_i^{(k)}(t^n) \tag{3.1.14}$$

where $\tilde{N}_i$ and $\tilde{x}_i$ denotes weight and abscissas of the expanded DSD. Equation (3.1.14) is a non-linear algebraic equation and can be solved by employing Product-Difference algorithm (PD) the details of the solution of this type of problems are given in the Gordon's study [14]. Nevertheless, this algorithm does not ensure that the solution is always non-negative for N_i and x_i, it's very sensitive to perturbations of right hand side values and this exhibits a bottleneck for the numerical solution of PBE coupled to CFD.

3.1.2. Time discretization

The numerical studies on the solution of population balance equations are mostly focused on developing numerical methods to discretize the PBE in the internal coordinate. The discretization in time is handled with explicit time stepping techniques, i.e. *Forward Euler*. However, regarding the problem being highly non-linear and having large time scales[4] high order implicit time stepping techniques can be more suitable.

[4] A "true" steady state could have not been observed in the experiments related to the simultaneous coalescence and breakage processes for large time scales [120].

Equation (2.2.1) is a an integro-differential equation and can be solved by even using "exotic" time stepping techniques. Bakhbakhi studied the solution of the PBE with the high-order Lax-Wendroff method and the combined Lax-Wendroff and Crank-Nicolson method, and he concludes that the second method could successfully treat the adopted population balance model in his study [121]. Bakhbakhi focused on the numerical solution of PBE in 0D, so he could study many different numerical techniques. However, this study is restricted with the conventional time-stepping techniques used in the field of computational fluid dynamics, One-step-θ schemes.

The PBE (2.2.1) with implicitly written right hand side can be given as,

$$\frac{f^{n+1}-f^{n}}{\Delta t} = \theta S^{n+1} + (1-\theta)S^{n}. \tag{3.1.15}$$

The time index is denoted with the ^{n} superscript and θ is the parameter of the time-stepping scheme. Certain values of the θ parameter leads to well known schemes as, $\theta = 0$ for the Forward Euler-, $\theta = 1$ for the Backward Euler- and $\theta = 0.5$ for the Crank-Nicolson-scheme.

Time discretization within method of classes

We can discretize the semi-discrete PBE 3.1.4 in time according to equation (3.1.15). The resulting fully discrete equation is

$$\frac{f^{n+1}(\upsilon_i)-f^{n}(\upsilon_i)}{\Delta t} = \theta S(f^{n+1}(\upsilon_i), f^{n+1}(\upsilon_j)) + (1-\theta)S(f^{n}(\upsilon_i), f^{n}(\upsilon_j)). \tag{3.1.16}$$

This is a non-linear equation for the unknown $f(\upsilon_i)^{n+1}$ and should be iteratively solved. The algorithm for the solution of this non-linear equation is presented in Figure 3.4.

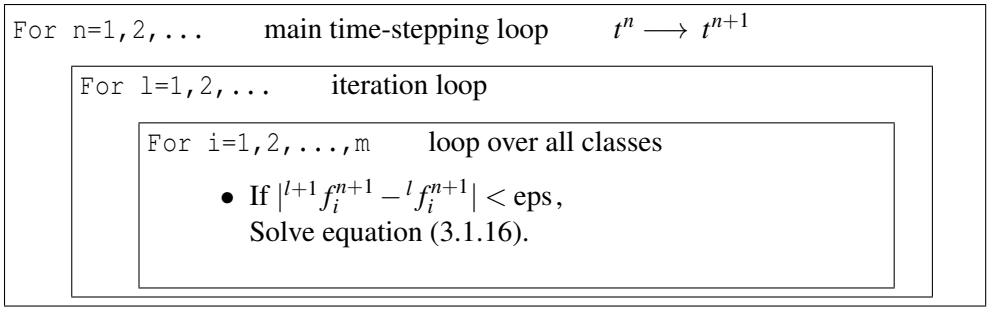

Figure 3.4: Solution of discrete PBE (eps: a small number, typically $\approx 10^{-8}$).

Time discretization within parallel parent daughter classes approach

The time discretization of equations within the PPDC method is analogous to the one within method of classes. However, solutions of the discrete equations are the sources and the sinks, i.e. births of the daughter classes and deaths in the parent classes, which are used to calculate moments of the population in the following part of the solution procedure given. Equations (3.1.10)–(3.1.12) need to be discretized in time to obtain the expanded particle size distribution, (3.1.13).

The equation (3.1.10) is the only non-linear equation in terms of the unknown N_i which should be treated implicitly for this equation. On the other hand, N_i is treated explicitly for the source

terms (3.1.11) and (3.1.12), since it is obtained by solving equation (3.1.10). By following this prescription, foremost we write down the discretized equation for the sink term analogously to equation (3.1.15).

$$\frac{{}^{l+1}N_i(t^{n+1}) - N_i(t^n)}{\Delta t} = \theta\Big(- {}^{l}N_i(t^{n+1}) \sum_{j=1}^{M} r^C(\upsilon_i^n, \upsilon_j^n)\, {}^{l}N_j(t^{n+1}) - {}^{l}N_i(t^{n+1}) \int_0^{\upsilon_i^n} r^B(\upsilon_i^n, \upsilon) d\upsilon \Big)$$
$$+ (1-\theta)\Big(- N_i(t^n) \sum_{j=1}^{M} r^C(\upsilon_i^n, \upsilon_j^n)\, N_j(t^n) - N_i(t^n) \int_0^{\upsilon_i} r^B(\upsilon_i^n, \upsilon) d\upsilon \Big) \quad (3.1.17)$$

On the right hand side, at the first term it may occur that the time indices ${}^{n\ n+1}$ are mixed but this is not true. While the sink term is calculated, only the change in weights (N_i) is accounted and the corresponding abscissas (υ_i) are constant through the time step, t^{n+1}, and they are updated when the expanded size distribution is reduced at the end of the time step; this point can be clearly seen at the presented algorithm in Figure 3.5. Therefore, we should keep in mind that the abscissas of parent classes are constant within one time step.

The discrete equation (3.1.17) can be solved with an analogous approach presented in Figure 3.4 to obtain $N_i(t^{n+1})$. Then, since the value of $N_i(t^{n+1})$ is known, A_{ij} and B_{ik} can be explicitly calculated according to the discrete equations (3.1.18) and (3.1.19).

$$\frac{A_{ij}(t^{n+1}) - A_{ij}(t^n)}{\Delta t} = (1-\theta)\Big((\frac{1}{2} - \delta_{ij}) r^C(\upsilon_i^n, \upsilon_j^n) N_i(t^n) N_j(t^n) \Big)$$
$$+ \theta\Big((\frac{1}{2} - \delta_{ij}) r^C(\upsilon_i^n, \upsilon_j^n) N_i(t^{n+1}) N_j(t^{n+1}) \Big) \qquad \text{for} \quad i,j = 1,...,M;\ j \geq i \quad (3.1.18)$$

$$\frac{B_{ik}(t^{n+1}) - B_{ik}(t^n)}{\Delta t} = (1-\theta)\Big(\gamma(\upsilon_i^n) N_i(t^n) N_i(t^n) \overline{P}(\upsilon_i^n, \upsilon_k^n) \int_0^{\upsilon_i^n} r^B(\upsilon_i^n, \upsilon) d\upsilon \Big)$$
$$+ \theta\Big(\gamma(\upsilon_i^n) N_i(t^{n+1}) N_i(t^{n+1}) \overline{P}(\upsilon_i^n, \upsilon_k^n) \int_0^{\upsilon_i^n} r^B(\upsilon_i^n, \upsilon) d\upsilon \Big)$$
$$\text{for } i = 1,...,M; k = 1,...,NB_i \quad (3.1.19)$$

3.2. Closures of Population Balance Equations

The Population Balance Equations of liquid/gas-liquid dispersed systems (Equation (2.2.1)) involve breakage and coalescence kernels (r^B and r^C respectively) which describe all the physics in breakup and coalescence phenomena. There are numerous studies available in the literature about modeling coalescence and breakage processes and a detailed review of these studies was presented by Jakobsen et al. [13]. While it is more likely to gather coalescence kernels into a unified framework, the breakage kernels show distinct behaviors and their formulations can exhibit remarkable differences which cause determination of the appropriate breakage kernel for this study to be cumbersome. To determine an appropriate coalescence kernel can also be troublesome if one is interested in the "unusual" effects of the chemical or physical properties of phases, e.g., electrocoalescence: is the coalescence which occurs due to the motion of an electrostatically

1. Abscissas and weights for M parent classes at $t = t^n$; if $n = 0$, initial conditions.
2. Calculating the weights of parent classes at t^{n+1} (3.1.17).
3. Calculating the abscissas and the weights of the coalescence daughter classes, (3.1.18).
4. Calculating the abscissas and the weights of the breakage daughter classes (3.1.19).
5. Solving the inverse finite-moment problem to obtain the abscissas and the weights of the parent classes at t^{n+1} from the expanded PSD (3.1.13).
6. Go to (1), if $t_{n+1} < t_{end}$ and $\frac{\|N^{n+1}-N^n\|_\infty}{\|N^n\|_\infty} > \mathrm{Tol_N}$
7. Stop

Figure 3.5: PPDC algorithm

charged dispersed phase under the influence of an electric field. Fortunately, we do not need to consider these “unusual" effects for our purposes; hence, a coalescence kernel which is commonly adopted for the studies of air/oil-water dispersions has been chosen.

The breakage kernels can be classified as statistical, theoretical and phenomenological. The last two are subject to this study because of their rigorous formulations and accurately reflecting the physics in the breakage process. The breakage kernels are adopted from the studies by *(i)* Lehr and Mewes [28], *(ii)* Lehr et al. [20], *(iii)* Martińez–Bazań et al. [23, 24].

3.2.1. Coalescence Kernel

Most of the present models for coalescence kernels were derived analogously to kinetic theory of gases [15–18]. In kinetic theory of gases, collisions between molecules are considered while in the process of coalescence, bubble (droplet)–bubble (droplet) and bubble/droplet–eddy collisions count. Thus, various coalescence models show similar trends, that is a monotonous increase in the specific coalescence rate with increase in the bubble/droplet diameter [19]. The coalescence kernel adopted in this work is the one proposed by Lehr *et al.* [20] which is implemented according to the technique developed by Buwa and Ranade.

According to Lehr and Mewes [28] the coalescence kernel function is defined by

$$r^C(\upsilon, \tilde{\upsilon}) = \frac{\pi}{4}(d + \tilde{d})^2 \min(u', u_{\mathrm{crit}}), \tag{3.2.1}$$

with d and $\tilde{d}$ denoting the diameter of bubbles of υ and $\tilde{\upsilon}$. The characteristic velocities u' and u_{crit}

are computed as follows

$$u' = \sqrt{2}\varepsilon^{1/3}(d\tilde{d})^{1/6}, \tag{3.2.2}$$

$$u_{\text{crit}} = \sqrt{\frac{We_{\text{crit}}\sigma}{\rho_l d_{eq}}} \quad \text{with} \quad d_{eq} = 2(d^{-1} + \tilde{d}^{-1})^{-1}, \tag{3.2.3}$$

where ε is the turbulent dissipation rate, σ is the surface tension of the liquid phase, ρ_l is the density of the liquid phase, and We_{crit} is the critical Weber number being equal to 0.06 for pure liquids [20]. Alternatively, it is also common to assume $u' = 0.08\,\text{m/s}$ instead of considering u' to be a function of υ and $\tilde{\upsilon}$, as it was done in the study of Lehr and his colleagues [20]. On the other hand, the coalescence kernel described with (3.2.1) shows similar trends with the most of the other models in the literature.

3.2.2. Breakage Kernel

Most breakage kernels are derived from the theories which are outlined by Kolmogorov [22] and Hinze [21]. Physical interpretations of these kernels are all the same: droplet breakage occurs due to the collisions of turbulent eddies onto the droplet surface; should the energy of the turbulent eddy larger than the surface energy, the surface is deformed. And, this deformation may split the droplet; so that, two or more daughter droplets appear. The turbulent eddies whose size is larger than or equal to the droplet size (diameter) spatially transport the droplets. Consequently, eddies which cause breakage are the ones only being smaller than the droplet size.

The main distinction among all these models which have the same physical interpretation is their prediction on the resulting daughter size distribution; some models presume a uniform or a truncated normal distribution which is centered at the half of the droplet size (I-type distribution function), i.e. an equal-sized breakage is preferable according to some models. In contrast, there are other models which suppose an unequal-breakage, breakage into a small and a large daughter droplets, which is preferable; these models suggest a U-type distribution function.

Regarding the daughter size distribution there are various different formulations which yield significantly different results. This is why it is not likely to claim that one model can highlight all the features of the given process. A comparison of the most remarkable breakup kernels in the literature is carried out by Wang et al. [29]. In pursuance of the this study, it is shown that the model presented by Lehr et al. [20] is more comprehensive than the others. Nevertheless, motivated by the wide diversity of available breakage models in the literature, we extended our scope by consideration of several breakage kernels: *(i)* Lehr and Mewes [28], *(ii)* Lehr et al. [20], *(iii)* Martińez–Bazań et al. [23, 24]. The first two are theoretical kernels, the last one is a phenomenological kernel with a statistically modeled daughter size distribution; and, each has been adopted by many researchers to model gas/liquid-liquid dispersed phase systems.

All the breakage models have the common definition: the multiplication of the total breakage rate, K^B, and daughter size distribution (DSD), $\Phi(\upsilon, \tilde{\upsilon})$, (3.2.4) and the same underlying assumptions: *(i)* the turbulence is usually assumed to be isotropic, *(ii)* only the binary breakage is considered, *(iii)* the breakage volume fraction is considered to be a stochastic variable, *(iv)* the occurrence of breakup is determined by the energy level of the arriving eddies, *(v)* only the eddies which are smaller or equal to the droplet/bubble diameter can lead to breakup. These assumptions have been introduced in order to achieve phenomenological simplifications by Luo and Svendsen [27]. So that, it has been possible to theoretically model the breakage rate without any free or adjustable

parameter; therefore, we focused on the mentioned breakage kernels.

$$r^B(\upsilon,\tilde{\upsilon}) = K^B \Phi(\upsilon,\tilde{\upsilon}) \tag{3.2.4}$$

Breakage Kernel by Lehr and Mewes

Lehr and Mewes [28] have had two approaches: a local and a global approach, to model the interfacial area density in bubble columns; and, population balance equations arise within the local approach as an attempt to model the breakup and the coalescence. Later, this model has been revised by Buwa and Ranade [19], and it is reformulated such that the implementation of the model is more straightforward.

Following the formulation of Buwa and Ranade, the breakage kernel can be rewritten according to equation (3.2.4) and the first term (breakage rate) can be given as,

$$K^B = 1.5(1-\alpha_g)\left(\frac{\rho_l}{\sigma}\right)^{2.2}\varepsilon^{1.8}, \tag{3.2.5}$$

where α_g, ρ_l, σ and ε are the void fraction of the secondary phase, the density of the primary phase, the interfacial tension and the turbulent dissipation rate, respectively. The aforementioned properties of the adopted breakage kernel are hidden in the definition of the daughter size probability distribution function, $\phi(\upsilon,\tilde{\upsilon})$, which can provide DSD representing both equal and unequal breakage; Figure 3.6 shows that the daughter size probability distribution function can describe

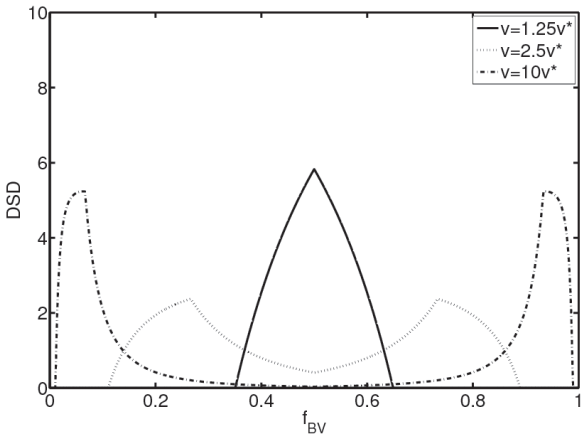

Figure 3.6: Dimensionless daughter size distribution.

the equal and unequal breakage as a function of the droplet size. If the parent droplet is very large respective to the stable droplet size, its daughter droplets have two extremely different sizes, i.e. unequal breakage, see the dashed-line curve for $v = 10v^*$. On the other hand, if the parent droplet's size is close to the stable size, the resulting daughter droplets have similar sizes, i.e. equal breakage, see the solid-line curve for $v = 1.25v^*$. This behavior of the distribution function is even intuitively right: Large bubbles are firstly hit by large eddies; so that, a very large and a very small daughter bubble form; and small bubbles are spatially transported by the large eddies but the collisions with small eddies result in two similarly sized bubbles. This behavior of the

distribution function is achieved by the following formula

$$\phi(\upsilon,\tilde{\upsilon}) = \max\left(\frac{\omega^{1/3}}{\tilde{\omega}^{4/3}}\left(\min\left(\tilde{\omega}^{7/6},\tilde{\omega}^{-7/9}\right)-\omega^{-7/9}\right),0\right) \quad \text{for} \quad \frac{\tilde{\omega}}{\omega}\in(0,0.5\rangle$$
$$\text{with} \quad \tilde{\omega}=\tilde{\upsilon}\frac{\pi}{6}\frac{\sigma^{1.8}}{\rho_l^{1.8}\varepsilon^{1.2}} \quad \text{and} \quad \omega=\upsilon\frac{\pi}{6}\frac{\sigma^{1.8}}{\rho_l^{1.8}\varepsilon^{1.2}}. \tag{3.2.6}$$

According to the implementation technique developed by Buwa and Ranade [19], the substitution of the dimensionless bubble volume $f_{BV}=\frac{\tilde{\omega}}{\omega}=\frac{\tilde{\upsilon}}{\upsilon}$ – Luo and Svendsen assumed that f_{BV} is the stochastic variable [27] – into (3.2.6) yields to

$$\phi(\upsilon,\tilde{\upsilon}) = \max\left(\omega^{-1}f_{BV}^{-4/3}\left(\min\left(\left(f_{BV}\omega\right)^{7/6},\left(f_{BV}\omega\right)^{-7/9}\right)-\omega^{-7/9}\right),0\right)$$
$$\text{for} \quad f_{BV}\in(0,0.5), \tag{3.2.7}$$

and makes it possible to analytically integrate the DSD in arbitrary limits. Being consistent with the assumption, the breakup process results in a pair of daughter bubbles of volume $\tilde{\upsilon}$ and $\upsilon-\tilde{\upsilon}$, this requires function being symmetric $\phi(\upsilon,\tilde{\upsilon})=\phi(\upsilon,\upsilon-\tilde{\upsilon})$ for $f_{BV}\in(0.5,1)$ (Figure 3.6). Consequently, the mean probability of breaking a bubble of volume υ into a bubble between $(\tilde{\upsilon}-\Delta\upsilon)$ and $(\tilde{\upsilon}+\Delta\upsilon)$, i.e. into a certain class whose pivot size is equal to $\tilde{\upsilon}$, can be obtained as follows

$$\Phi(\upsilon,\tilde{\upsilon}) = \frac{\upsilon}{2\Delta\upsilon}\int_{\frac{\tilde{\upsilon}-\Delta\upsilon}{\upsilon}}^{\frac{\tilde{\upsilon}+\Delta\upsilon}{\upsilon}}\phi(\upsilon,\tilde{\upsilon})\,df_{BV}. \tag{3.2.8}$$

Breakage Kernel by Lehr et al.

Lehr et al. [20] follow the definition of breakage kernel in (3.2.4) and they postulate that bubble/droplet size distribution can be calculated by specifying the breakage rate and knowing the daughter size distribution. They also clearly state all the assumptions which were made by Luo and Svendsen but the first one (see above the given assumptions). However, even though it is not explicitly stated, this assumption is in between the lines of their study; otherwise, they would not be able to handle the problem.

They start with the assumption: Right before the breakage, the bubbles are locally almost cylindrical; so that, the force balance can be written as

$$\frac{1}{2}\rho_l u_\lambda^2 = 2\frac{\sigma}{\tilde{d}}, \tag{3.2.9}$$

where u_λ, ρ_l, σ and $\tilde{d}$ denote the turbulent eddy velocity, the continuous phase density, interfacial tension and the smaller daughter droplet's size.

The breakup kernel is calculated from the frequency of the colliding eddies and the probability of these collisions leading to breakup

$$r^B(\upsilon,\tilde{\upsilon}) = \int_{\tilde{d}}^{d}\omega(\upsilon,\lambda)P(\lambda,\tilde{\upsilon},\upsilon)\mathrm{d}\lambda.$$

$\omega(\upsilon,\lambda)$ stands for the number of collisions between a droplet with the volume υ and an eddy of length scale λ; and $P(\lambda,\tilde{\upsilon},\upsilon)$ is the probability that the collision between them results in a droplet of size $\tilde{\upsilon}$. The collision frequency has been derived analogously to the kinetic gas theory as follows

$$\omega(\upsilon,\lambda) = \frac{\pi}{4}(\lambda+d)^2\overline{u}_\lambda n_\lambda. \tag{3.2.10}$$

The turbulent eddy velocity can be calculated according to Hinze [21] as $\overline{u}_\lambda = \sqrt{2}(\varepsilon\lambda)^{1/3}$. The number of eddies per unit volume $n\lambda$ having size between λ and $\lambda + d\lambda$ is given as $n_\lambda = \frac{0.8413}{\lambda^4}$.

One can derive the breakage probability $P(\lambda, \tilde{\upsilon}, \upsilon)$ again by following Hinze and starting with the force balance (3.2.9), Hinze postulates that the eddy velocities is distributed according to a Gaussian curve (normal distribution) about a mean value $\overline{u}_\lambda$. Then, the breakage probability is

$$P(\lambda, \tilde{\upsilon}, \upsilon) = \frac{4\sigma}{\pi\rho_l} \frac{(\varepsilon\lambda)^{-2/3}}{\tilde{d}^4} exp\Big(-\frac{2\sigma(\varepsilon\lambda)^{-2/3}}{\rho_f \tilde{d}}\Big) \tag{3.2.11}$$

So, the breakage kernel function can be obtained by combining equations (3.2.11) and (3.2.10) as

$$\begin{aligned} r^B(\tilde{\upsilon}, \upsilon) = \int_{\tilde{d}}^{d} \sqrt{2}\, C\, \frac{\sigma}{\rho_f \varepsilon^{2/3} \tilde{d}^4} \frac{(\lambda + d)^2}{\lambda^{11/3}} exp\Big(-\frac{2\sigma}{\rho_f \varepsilon^{2/3} \lambda^{2/3} \tilde{d}}\Big) d\lambda \\ \text{for} \quad 0 \le \tilde{\upsilon} \le \upsilon/2 \\ r^B(\tilde{\upsilon}, \upsilon) = r^B(\upsilon - \tilde{\upsilon}, \upsilon) \qquad \text{for} \quad \upsilon/2 < \tilde{\upsilon} \le \upsilon \end{aligned} \tag{3.2.12}$$

where $C = 0.8413$. However, equation (3.2.12) can not yet be expressed as (3.2.4); hence, (3.2.12) is rewritten as being analogous to (3.2.4), by using the incomplete Γ-functions and by introducing the length and time scales:

$$L = \Big(\frac{\sigma}{\rho_f}\Big)^{0.6} \varepsilon^{-0.4} \quad \text{and} \quad T = \Big(\frac{\sigma}{\rho_f}\Big)^{0.4} \varepsilon^{-0.6} \tag{3.2.13}$$

Defining the dimensionless bubble diameter $d^* = d/L$ and bubble volume $\upsilon^* = \upsilon/L^3$ gives rise to:

$$\begin{aligned} K^B &= \frac{d^{*5/3}}{2T} \exp\left(-\frac{\sqrt{2}}{d^{*3}}\right) \\ \phi(\upsilon, \tilde{\upsilon}) &= \frac{6}{\left(L\sqrt{\pi}\tilde{d}^*\right)^3} \frac{\exp\left(-2.25\left(\ln\left(2^{2/5}\tilde{d}^*\right)\right)^2\right)}{1 + \operatorname{erf}\left(\ln\left(2^{1/15} d^*\right)^{1.5}\right)} \quad \text{for} \quad \tilde{\upsilon}^* \in (0, 0.5\rangle \\ \text{and} \qquad & \phi(\upsilon, \tilde{\upsilon}) = \phi(\upsilon, \upsilon - \tilde{\upsilon}) \quad \text{for} \quad \tilde{\upsilon}^* \in (0.5, 1)\,. \end{aligned} \tag{3.2.14}$$

So that, to rewrite the kernel in the form of (3.2.4) is accomplished.

Breakage Kernel by Martínez-Baźan et al.

Martínez-Baźan et al. experimentally studied a lean air-in-water dispersion to model the breakup phenomenon. The dispersed system exhibits negligible coalescence therefore they could consider solely the effect of the breakage on the transient evaluation of bubble-size[5] distribution function in a fully developed turbulent flow field in order to model a phenomenological breakup kernel.

Martínez-Baźan et al. modeled the breakage kernel according to the definition of Luo and Svendsen, (3.2.4). In the first part of their study they obtained the breakup frequency [23] and later they drived the expression for the daughter size distribution [24]. Then, they performed a number of experiments and computations over a wide range of bubble sizes to verify the derived breakup kernel.

[5] Martínez-Baźan et al. stated that their model is also valid for liquid–liquid dispersions. Since they use the word "bubble" in their article, in this subsection the word "bubble" is adopted to refer the dispersed phase.

They started with the same assumptions of Luo and Svendsen; additionally, they assumed that since the studied dispersion is very lean, the secondary phase had no significant influence on the primary phase, no back-coupling. And, their basic presumption was: The turbulent stress produced by the primary phase deforms the bubble's surface and this deformation might lead to breakup of bubble. Then, it was possible to write with neglecting the internal viscous deformation forces due to very small Ohnesorge number, e.g, $Oh < 10^{-2}$ for a bubble of size $10^{-}6\,\mathrm{m}$, the deformation force per unit surface as

$$\tau_t(D) = \frac{1}{2}\rho\overline{\Delta u^2}(D),$$

where the last term denotes the velocity fluctuations between the two points having a distance D and it can be estimated by the expression

$$\overline{\Delta u^2}(D) = \beta(\varepsilon D)^{2/3},$$

where β is an empirical parameter and whose value was given as 8.2 by Batchelor [122]. Then, following the presumption and the the deformation force per unit area, it is possible to introduce two key concepts: the critical diameter (D_c) and the minimum diameter (D_min) and they can be formulated as,

$$D_\mathrm{c} = \left(\frac{12\sigma}{\beta\rho}\right)^{3/5}\varepsilon^{-2/5} \quad \text{and} \quad D_\mathrm{min} = \left(\frac{12\sigma}{\beta\rho D}\right)^{3/2}\varepsilon^{-1}.$$

With these concepts, one can describe the breakage of a bubble as, only bubbles which are larger than the D_c can breakup and the smaller or equal-sized bubbles are stable in the turbulent flow, and the smallest daughter bubble can not be smaller than D_min. These two concepts are the basic differences of this breakage model compared with the first two and lead to a significantly different daughter size distribution.

The breakup frequency was considered as a function of mainly two variables: bubble-size (d) and turbulence which is characterized by a dissipation rate (ε). Then, the authors postulated that the breakup frequency is inversely proportional to the difference between the deformation and the confinement forces which produce the deformation of the interface. Then, the breakup frequency can be written as,

$$K^B(\varepsilon, d) = K_g\frac{\sqrt{\beta(\varepsilon d)^{2/3} - 12\sigma/(\rho d)}}{d} \tag{3.2.15}$$

where K_g is another empirical parameter being equal to 0.25 which was obtained by the authors. The breakup frequency is zero for bubbles of size $d < D_\mathrm{c}$, and it rapidly increases for the ones being larger than the critical size and reaches a maximum at $d = 1.63D_\mathrm{c}$ and later, it decreases monotonically with increasing bubble size.

Independent of the breakup frequency the authors assume a binary breakage which leads to two daughter bubbles of complementary masses/volumes, with sizes d_1 and d_2. When the stochastic variable d_1 (the third assumption) is uniformly distributed on $[0, d_0]$, so does $d^* = d_1/d_0$ on $[0, 1]$. On the other hand, the breakup does not produce a uniformly distributed density function and the probability of the splitting of a bubble of size d_1 should be weighted with the difference in the stresses, $\Delta\tau_{t1} = \frac{1}{2}\rho\beta(\varepsilon d_1)^{2/3} - 6\sigma/d_0$. Moreover, appearance of a daughter bubble of size d_1 implies that there exists a complementary bubble for which the probability is proportional to $\Delta\tau_{t2} = \frac{1}{2}\rho\beta(\varepsilon d_2)^{2/3} - 6\sigma/d_0$. Hence, the author postulates that the probability of a bubble breaking into a pair of bubbles with sizes d_1 and d_2 should be proportional as following:

$$P(d^*) \propto \left[\tfrac{1}{2}\rho\beta(\varepsilon d^* d_0)^{2/3} - \frac{6\sigma}{d_0}\right]$$

Then, by introducing a dimensionless variable $\Lambda = D_c/d_0$ and regarding that the density probability is normalized, the daughter probability density function of d^* can be written as:

$$\phi^*(d^*) = \frac{P(d^*)}{\int_0^1 P(d^*)} = \frac{[d^* - \Lambda][(1-d^{*3})^{2/9} - \Lambda^{5/3}]}{\int_{d^*_{min}}^{d^*_{max}} [d^* - \Lambda][(1-d^{*3})^{2/9} - \Lambda^{5/3}]\mathrm{d}(d^*)} \tag{3.2.16}$$

Finally, the probability density function of daughter bubbles as a result of the breakup of a parent bubble d_0 is obtained as $\phi(d1, d0) = \phi*(d^*)/d_0$. The function ϕ mainly depends on ε and d_0 and this is presented in Figure 3.7. In Figure 3.7, the dependence of DSD on the turbulent dissipation

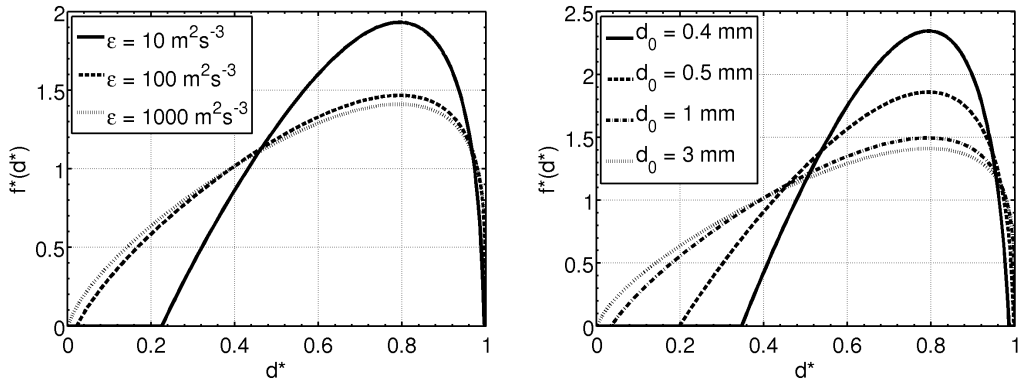

Figure 3.7: The dependence of DSD on ε and d_0, respectively.

rate is given for air in water dispersed phase system, with a fixed parent size, $d_0 = 3\,\mathrm{mm}$; on the right the dependence on d_0 is shown for a fixed turbulent dissipation rate, $\varepsilon = 1000\,\mathrm{m^2 s^{-3}}$. The possible minimum bubble size, $D_{\min}$, is strongly related to ε and d_0. The inverse proportionality between $D_{\min}$, and ε and d_0 is clearly shown. Additionally, these are the reproduction of the Figure 3 from Martińez–Bazań et al. and our computations match exactly to theirs; consequently, our implementation is validated.

Martińez–Bazań et al. suggested the DSD which prefers only the equal breakage hence the function is I-type. This is significantly different than the previously discussed kernels which combines the advantages of both U-type and I-type functions. Also, defining D_c and especially $D_{\min}$ is debatable, having a certain minimum size enforces the daughter size distribution to be I-type, where as Lehr et al. states that collision of large bubbles firstly with large eddies results in two daughter bubbles which are extremely different in size. The statement of Lehr et al. is more satisfactory with respect to Martińez–Bazań et al.; however, once we successfully compare these models, we can make a clear conclusion.

3.3. Hypothetical Closures

Certain kernels are proposed to close the PBE *only* in order to study them computationally. These kernels are chosen so simple that they lead to analytical solution of the PBE. We will address several of the hypothetical closures to test the implemented numerical techniques.

Coalescence kernels for which analytical solutions of PBE are available from Scott (1967) [123] describes a constant coalescence

$$r^C(\upsilon, \tilde{\upsilon}) = C, \tag{3.3.1}$$

and a sum-coalescence

$$r^C(\upsilon,\tilde{\upsilon}) = C(\upsilon+\tilde{\upsilon}). \tag{3.3.2}$$

The analytical solution of the PBE being closed with these kernels are provided for the initial condition

$$f(\upsilon,t=0) = N_0 e^{-\upsilon}. \tag{3.3.3}$$

The analytical solution with the constant closure (3.3.1) is given as

$$f(\upsilon,t=0) = \frac{2N_0}{CN_0t+2}. \tag{3.3.4}$$

And the solution with the sum coalescence (3.3.2) is

$$f(\upsilon,t=0) = N_0 e^{-CN_0\upsilon_0 t}. \tag{3.3.5}$$

McCoy and Madras [42] studied analytical solution of PBE for simultaneous coalescence and breakage. They adopted the constant coalescence kernel (3.3.1) and a breakage kernel which is directly proportional to the volume of the parent droplet/bubble and the breakage rate and daughter size probability function are given as equation (3.3.6).

$$K^B = S\upsilon \quad \text{and} \quad \phi(\upsilon,\tilde{\upsilon}) = 1/\tilde{\upsilon} \tag{3.3.6}$$

The initial condition which leads to the analytical solution for the total number density, (3.3.8), was chosen as following,

$$N(\upsilon,t=0) = \frac{m_0(0)^2}{m_3} e^{-\frac{m_0(0)}{m_3}\upsilon}. \tag{3.3.7}$$

$$\phi(\eta,\tau) = [\varphi(\tau)]^2 e^{-[\eta\varphi(\tau)]}. \tag{3.3.8}$$

In Equation (3.3.8) the dimensionless variables are $\eta = \upsilon m_0(0)/m_3$, $\tau = tC/m_0(0)$ and φ with the expression:

$$\varphi(\tau) = \varphi(\infty)\frac{1+\varphi(\infty)\tanh(\varphi(\infty)\tau/2)}{\varphi(\infty)+\tanh(\varphi(\infty)\tau/2)} \tag{3.3.9}$$

where $\varphi(\infty) = [2Sm_3/C]^{1/2}/m_0(0)$.

For different values of $\varphi(\infty)$, it is possible to simulate three cases: *(i)* the invariant solution: $\varphi(\infty) = 1$, *(ii)* the breakage dominant solution: $\varphi(\infty) > 1$, *(iii)* the coalescence dominant solution ($\varphi(\infty) < 1$). The last two cases are in our scope to test the accuracy of the implemented numerical techniques, PPDC and MC.

3.4. Numerical Computations

The breakage and coalescence models and the numerical techniques which have been discussed in this chapter are employed to simulate physical and hypothetical cases. While we are analyzing the accuracy of the implemented models, the efficiency and the robustness of the adopted numerical techniques are investigated, as well. First, we consider the accuracy and the efficiency of the numerical techniques, MC and PPDC, for cases which admit analytical solutions. Later, physical cases which have been already numerically and experimentally studied by other researchers are studied with the theoretical and phenomenological breakage kernels and the coalescence kernel. So that, we are able to validate our implementation and to see the accuracy of the models and the range of their operating conditions. Consequently, we can determine the pair of kernels and the discretization technique for the internal coordinate to be adopted so to study the PBE in 3D.

3.4.1. Hypothetical Cases

We have numerically studied three cases with the hypothetical kernels proposed by Scott [123], and McCoy and Madras [42] who also provided the analytical solution of the PBE with them. The first two cases are numerical simulation of pure coalescence phenomena which are described with the kernels (3.3.1) and (3.3.2), in order. Later, we look upon a simultaneous coalescence and breakage case which are modeled with (3.3.1) and (3.3.6).

The constant coalescence kernel (3.3.1) describes the coalescence of droplets with a constant rate independent of any other variable or parameter. When the initial condition is taken as in (3.3.3), the PBE with this kernel can be analytically solved for the total number density and the solution is given with (3.3.4).

For the calculations the initial value of the total number density $N(t=0)=N_0$ and C were set to 1 and the numerical results were obtained with the PPDC and the MC, see Figure 3.8 and Figure 3.9.

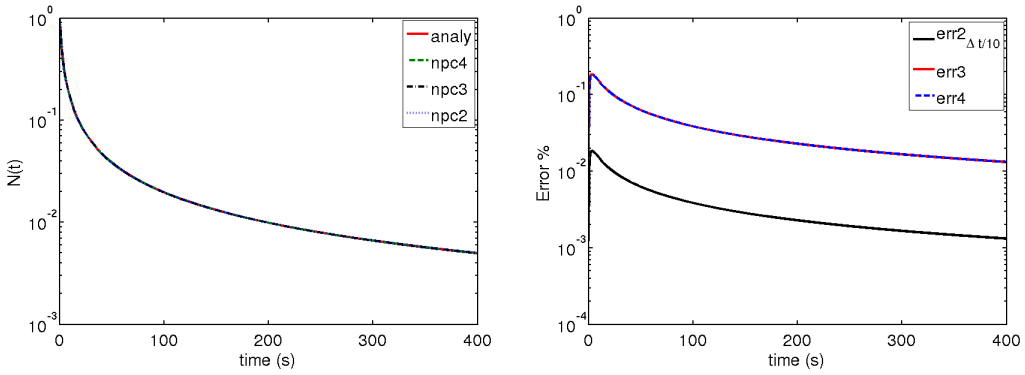

Figure 3.8: $N(t)$ for different number of parent classes (npcX) and the corresponding errors (errX), within the PPDC method.

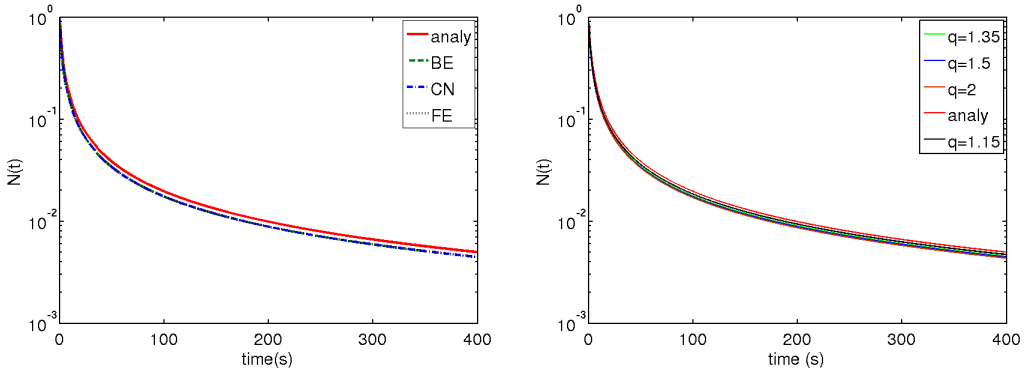

Figure 3.9: Comparison of $N(t)$ with the analytical solution (red) for different time discretization techniques and $q=1.5$ (left), and for different values of q (right).

The first conclusion reads: the PPDC is more accurate than the MC and the computational effort and the time are incomparably in favor of the PPDC. Different numbers of parent classes ($npc=2,3,4$) lead to identical evaluation of total number density in time. This is not surprising be-

cause within PPDC, the first $2 \times npc$ number of moments are always conserved; $N(t)$ corresponds to the zeroth order moment hence it has to be preserved even with the least number of parent class, 2. On the other hand, with the adopted approach of MC it is possible to preserve only one moment which has chosen to be the third order moment, total volume density, i.e. volume fraction of the secondary phase. The conservation of this variable is more important for the solution of physical problems, otherwise the mass conservation is violated (incompressibility). Consequently, there is a visible difference among the results with MC, see Figure 3.9; however, as $q \to 1$ the difference is getting visibly smaller; and, when one has a linear discretization of the internal coordinate, the error will be independent of the internal coordinate discretization and will be limited by the accuracy of the time discretization as in the case of PPDC, Figure 3.8. The plots of the errors show that the error is reduced to the one tenth when the time step size is chosen to be one tenth, 0.1 ms. We can have a closer look at the errors in the results with MC, first we see the convergence with q, Figure 3.10 (BE, FE and CN denote Backward-, Forward-Euler and Crank-Nicholson, in order).

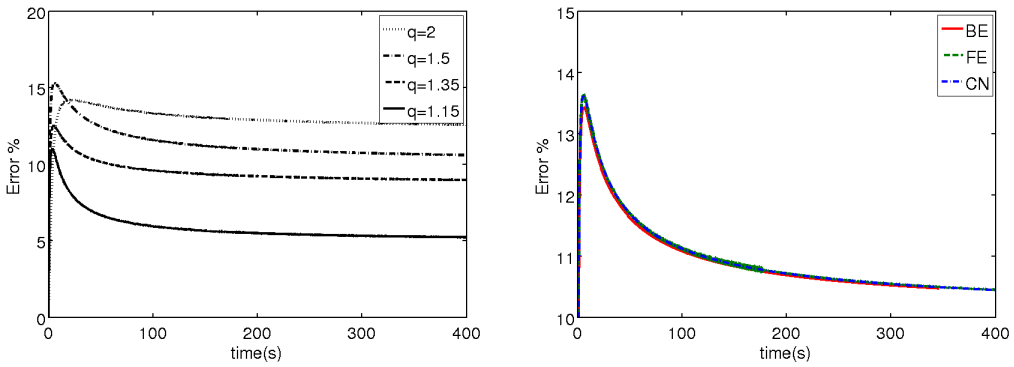

Figure 3.10: $N(t)$ with various values of q (discretization constant) and different time discretization techniques.

The error for the smallest q decreases to $\approx 5\%$ from $\approx 13\%$, and the computational cost increases exponentially; even though the required computational cost for the finest calculations are easily affordable for ideal STR simulations, this is not the situation for 3D simulations which are coupled to CFD. Table 3.1 shows that how the computation time changes with respect to number of classes; for this purpose, the constant-coalescence case is computed with FE method with fixed time step-size on dual-core AMD Opteron™ 2214 processor (2.2 GHz).

The behavior of the PPDC regarding the time discretization technique is studied for three parent classes and the time step size being $dt = 1$ ms, see Figure 3.11. Although the results which are obtained with PPDC are very sensitive to the time step size, Figure 3.8, it is not surprising that all time-stepping methods produce the same results for sufficiently small time steps. Consequently, the results can not be significantly improved with adopting a higher order or a more stable time discretization technique and the error introduced by the time discretization is linearly proportional to the time step size within PPDC.

The results which are obtained with MC have larger errors than the ones obtained by PPDC, Figure 3.11 and Figure 3.10. Moreover, as in the case of PPDC, the choice of discretization technique is not very influential on results unless the time step size is too large. Nevertheless, this test case is only for a constant coalescence kernel and it is not sufficiently complicated to comprehensively compare the two methods but, this test case is important to see that our understanding and implementation is correct for the constant coalescence.

Table 3.1: Time vs number of classes.

q	nClass	Time (s)
2	30	3.53E0
1.9	32	3.99E0
1.8	35	4.88E0
1.7	39	6.04E0
1.5	50	1.02E1
1.25	91	3.27E1
1.20	111	4.94E1
1.15	145	8.38E1
1.075	279	3.15E2
1.05	413	6.94E2
1.01	2021	2.13E4

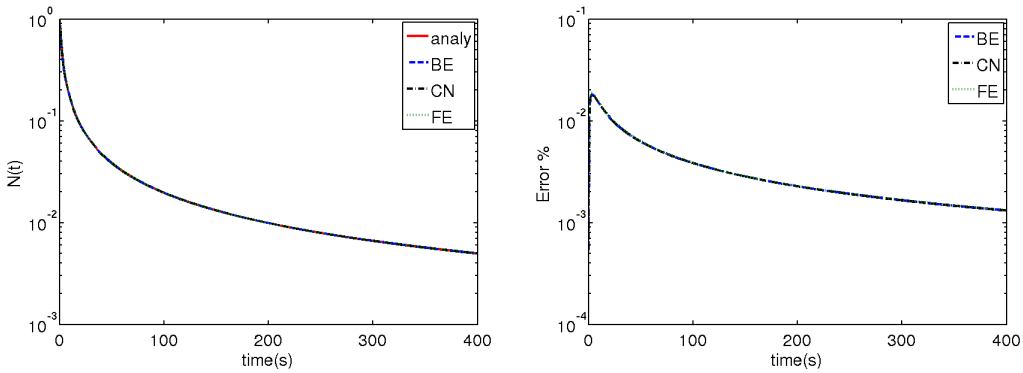

Figure 3.11: Errors due to different discretization techniques within PPDC.

The sum-coalescence kernel 3.3.2 is slightly more complicated than the constant coalescence kernel. This time, the coalescence rate is not constant and depends on the droplet sizes, i.e. the solution of the previous time step, and it logarithmically increases in time. We studied this case for different number of parent classes ($npc = 2,3,4$) with PPDC, and for $q = 1.5$ with MC; the results are as follows, Figure 3.12 and Figure 3.13.

The obtained results by both methods are satisfactory and as in the first case, PPDC leads to more accurate results such that the error is always less than 1% independent of the number of parent classes. On the other hand the error for MC is mostly between 10% and 15%, and this can be reduced by decreasing the value of q or adopting a linearly discretized internal coordinate which leads to results only involving errors due to time discretization as it holds for PPDC. Nevertheless, our aim, here, is not to obtain the exact results but to see the accuracy of the employed numerical techniques with the values of parameters which we will employ in the 3D simulations.

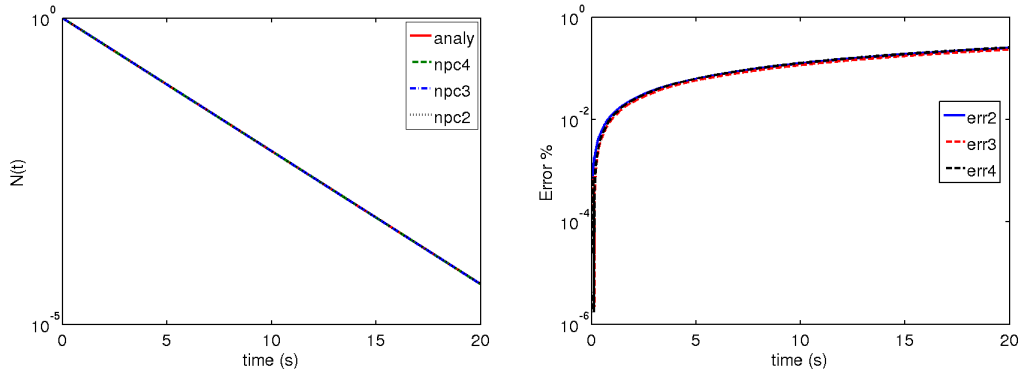

Figure 3.12: Results for sum coalescence kernel with PPDC.

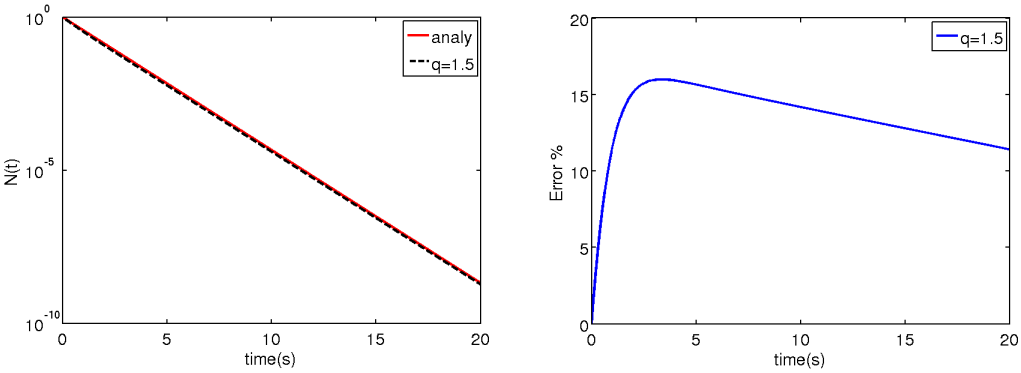

Figure 3.13: Results for sum coalescence kernel with MC.

There is a very small difference in the results with PPDC for different number of parent classes, almost invisible, Figure 3.12. The results are very sensitive to initial conditions and parent classes can not be uniquely initialized for two and three parent classes because there are only two constraints on the initial condition: the total volume and the total number of droplets. Hence, the difference in the results must be due to the initial conditions.

The second case was studied also by Bove et al. [97]. Our results are almost identical with theirs but the results of Bove et al. are slightly oscillatory for the first eight seconds. We think that these oscillations are purely due to the time discretization. They write the discrete form of the equations in the Forward-Euler scheme; if they had used smaller time step size or a stable time stepping scheme, e.g., Backward-Euler, their results would not have been oscillatory.

The last case which is the most challenging involves both the breakage and the coalescence phenomena. The coalescence phenomena is again described with the constant kernel (3.3.1) and the breakage is described with equation (3.3.6). The challenging part of this problem is the implementation of the breakage kernel. Whereas the arising coalescence daughter classes are uniquely specified, the breakage classes are not. We see two options, either the breakage daughter classes are specified in a similar fashion to the one employed in MC or directly the arising source terms for the moments due to the breakage daughter classes are calculated. The later option would not require the specification of the breakage daughter classes; and, their contribution to the first $2M$ moment values can be calculated analogously to the quadrature method of moments. In this case, the method would suffer the same problems as does QMOM, closure problems. Moreover, Bove et al. clearly state that the breakage daughter classes exist due to the breakage of parent classes.

Therefore, we followed the first choice and define the width of classes as one hundredth of the parent classes' so that the discrete internal coordinate consists of 100 equidistant classes; and, for the i'th class the pivot location is given as $\upsilon_i = \frac{2i-1}{200}\upsilon$ for $i = 1, 2, ..., 100$. The number hundred is not a magical number, our studies which are presented later show that the results with 100 breakage daughter classes lead to sufficiently accurate results.

The case is simulated for $S = 1$ and $C = 0.1$ with both MC and PPDC and the results are compared against the values computed from the analytical solution (3.3.8), Figure 3.14. The

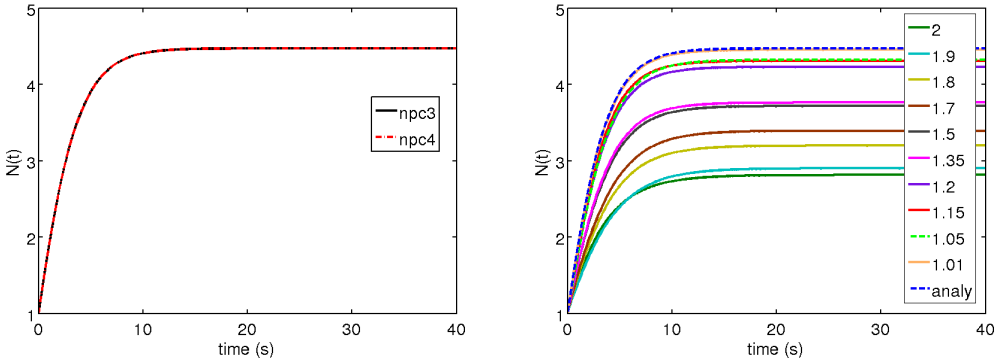

Figure 3.14: Results for the simultaneous breakage and coalescence phenomenon with PPDC (left: with 3 and 4 parent classes) and MC (right: for varying values of q).

results which have been obtained with PPDC are so accurate that it was not necessary to plot the reference solution (the curve "analy" in the right plot); whereas, it was required to reduce the discretization constant to very small values ($q < 1.01$), of course, this ends up in such high computational costs that it is not possible to afford for the solution of coupled CFD-PBE problems. Therefore, the convergence of PBE's solution for physical kernels is also needed to be analyzed. Unless fairly converged results can be obtained with reasonably small values of the discretization constant, $q \approx 1.5$, progressing with MC will not be possible.

The errors due to the number of parent classes adopted in PPDC are presented in Figure 3.15. The total number density, N(t), is indistinguishably evolving in time for two and three parent classes. This is expected because the total number density is conservative for any number of parent classes; however, this is not the case for the high order of moments, e.g., greater than four because the required order of moments for the engineering applications are mostly smaller than four and seldom equal to four. To investigate the results for the high order moments we adopted the analytical solution for the fractional moment order (3.4.1) from the study by Silva et al. [40].

$$m_k(\tau) = \left[\varphi(\infty)\frac{\varphi(\infty) + \tanh(\varphi(\infty)\tau/2)}{1 + \varphi(\infty)\tanh(\varphi(\infty)\tau/2)}\right]^{k-1} \Gamma(k+1) \tag{3.4.1}$$

The results obtained with three parent classes are less accurate than the case with four parent classes, especially for moment order being larger than five, $k > 5$. The error at $k = 3$ drops to the machine precision which means that volume (in case of constant density mass) is strictly conserved. Of course, the error values reduce linearly with reducing the time step size. These results agrees well with those of Bove et al. [97]. The results for the same case which are obtained by MC are not as promising as the ones with PPDC, Figure 3.14. Errors due to the discretization of internal coordinate with different number of classes, i.e. varying values of the discretization constant, are presented in Figure 3.16. The steady-state results which are obtained with MC are

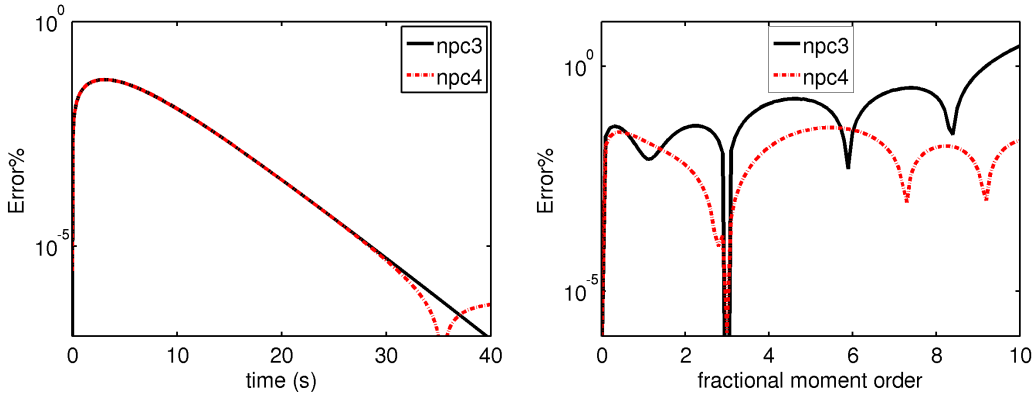

Figure 3.15: Error of the results for the simultaneous breakage and coalescence phenomenon with PPDC, left: for $N(t)$, right: for the fractional moment order.

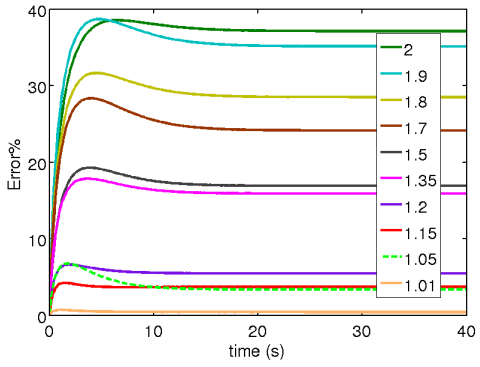

Figure 3.16: Error of the results for the simultaneous breakage and coalescence cases with MC.

nicely converging to the analytical solution with the grid refinement. The error drops from 40 % to less than 1 % for values of q which decreases from 2 to 1.01, Table 3.2.

Table 3.2: Final error in total number density vs the discretization constant.

q	1.01	1.05	1.15	1.20	1.35	1.50	1.70	1.80	1.90	2
Error (%)	0.4	3.4	3.7	5.5	15.9	16.9	24.2	28.5	35.1	37.1

The test cases: *(i)* the constant coalescence, *(ii)* the sum coalescence, *(iii)* the simultaneous breakage and coalescence kernels were numerically studied within MC and PPDC frameworks. Numerically obtained results are compared against the computed results from the analytical solutions which are presented by Scott [123] for the first two cases, and McCoy and Madras [42] for the last case. Moreover, the numerical solution of the third case has been compared with the analytical solution of Silva et al. [40] for fractional order of moments. PPDC is very satisfactory according to accuracy, performance and robustness, and MC requires a very fine grid in the internal coordinate to be sufficiently accurate; this requirement leads to much higher computational cost than PPDC. Of course, the studied problems are 0D and the computational costs/efforts are negligible comparing to available computer resources. However, the methods will be employed in 3D as well, in those cases negligible costs will add up and perhaps create a great bill. Hence,

it is a very important point that MC is relatively an expensive method, and if it requires such fine grids to converge when the physical kernels are employed, MC should be discarded. On the other hand the studied case suits better to test mostly moment based methods; thus, it was not fair to compare the two methods within these test cases. Nevertheless, the comparisons verify that our implementations are correct and the numerical results are valid.

3.4.2. Physical Cases

In this subsection, the physical kernels are employed to close PBE, so to numerically simulate the dispersed phase flow in stirred tanks. Several studies [19, 124–126] provide comprehensive experimental data and numerical results for dispersed phase systems in STRs which are mostly air in water dispersions for varying volume ratios of the phases and different values of turbulent dissipation rates. These studies provide us with a good basis to verify employed breakage and coalescence kernels and to compare them within the adopted numerical approaches because if the values of dissipation rate and gas holdup are fixed for a certain dispersed phase system, the equilibrium size distribution will be unique regardless of the initial conditions.

This subsection is also interesting to see the applicability range of the kernels for different physical parameters, e.g. void fraction, interfacial tension, turbulent dissipation rate. For this purpose, the experiments which are conducted by Laakkonen et al. [127] and Olmos et al. [128] will be numerically simulated and the results will be compared. Laakkonen et al. studied the evolution of the secondary phase in highly turbulent flows and Olmos et al. focused on the experiments with low values of turbulent dissipation rate.

First, we compare the first and the second breakage kernels, breakage kernels by Lehr et al. [20, 28]. Three test cases are considered, they all involve air in water dispersion with different holdup and turbulent dissipation rate values:

i) case-1A: $\alpha = 0.13$ and $\varepsilon = 0.392\,\mathrm{m^2 s^{-3}}$,

ii) case-1B: $\alpha = 0.08$ and $\varepsilon = 0.196\,\mathrm{m^2 s^{-3}}$,

iii) case-1C: $\alpha = 0.20$ and $\varepsilon = 0.785\,\mathrm{m^2 s^{-3}}$.

The test cases are chosen such that they have already been studied by other researchers and reliable experimental and/or numerical results are available. Later, PPDC and MC are studied in test case-1A by employing the superior breakage kernel of the tests, so to compare the accuracy and efficiency of the numerical methods. The superior theoretical kernel is also compared against the phenomenological kernel and the chosen breakage kernel is used to numerically simulate the cases which were studied by Laakkonen et al. and Olmos et al. in order to have an idea on the range of applicability.

Comparison of the Theoretical Breakage Kernels

The theoretical kernels are studied within the three test cases, case-1A is simulated with using both the first [28] and the second [20] breakage kernels for varying values of the discretization constant q in order to obtain a converged result with respect to the discrete internal coordinate; then, the coarse grid and the fine grid results are compared against the experimental and the numerical results which were provided by Wilkinson [124], and by Buwa and Ranade [19], respectively. Later, the value of q for the fine grid is adopted to simulate the case-1B and case-1C with the both breakage kernels.

If we consider that the three test cases exhibit a range, case-1A is the moderate one with respect to both turbulent dissipation rate and holdup of the secondary phase with $\alpha = 0.13$ and $\varepsilon = 0.392\,\mathrm{m^2 s^{-3}}$. This air in water dispersed phase system is simulated with both breakage kernels for varying values of discretization constant, $q = \{1.05, 1.075, 1.15, 1.25, 1.5, 2.0\}$, see Figure 3.17, in order to see the convergence behavior of the kernels.

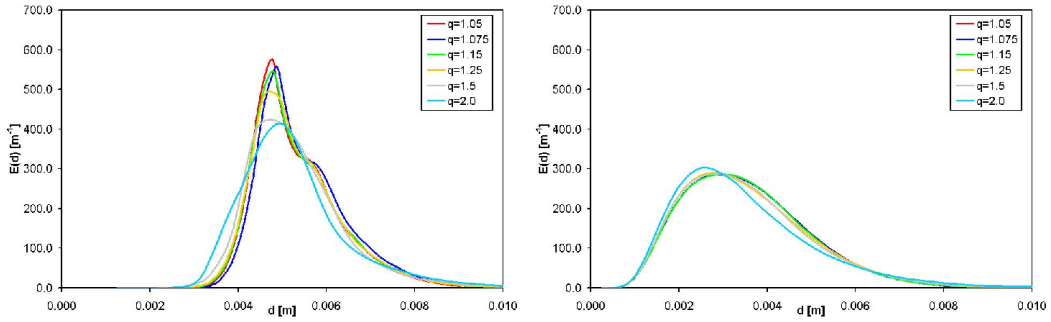

Figure 3.17: Steady state interfacial area density vs bubble diameter for case-1A, $q = 1.05, 1.075, 1.15, 1.25, 1.5, 2.0$. Left: The first breakage kernel [28]. Right: The second breakage kernel [20].

The results which are obtained with the first breakage kernel show a great change for varying values of q, the steady-state results for $q = 2$ and $q = 1.05$ are completely distinguishable, and the results poorly converges, even the results for $q = 1.075$ and $q = 1.05$ visibly differ, see Figure 3.17. Regarding the plot on the left, it is unlikely to claim that any value of q leads to a grid independent result but we can conclude that one has to choose q less than 1.15 for a "converged" result. On the other hand, the results which are obtained with the second kernel converge very nicely with the grid refinement, even the results with $q = 1.5$ can be accepted as converged. The results with $q < 1.25$ are indistinguishable in the plot at the right in Figure 3.17. Consequently, the second breakage kernel has a better convergence behavior with the grid refinement.

The obtained converged results motivated us to compare our numerical results against the experimental results. The results which we got on the finest and the coarsest grids were plotted with the experimental results, see Figure 3.18. It should be noted, that Wilkinson's data on bubble

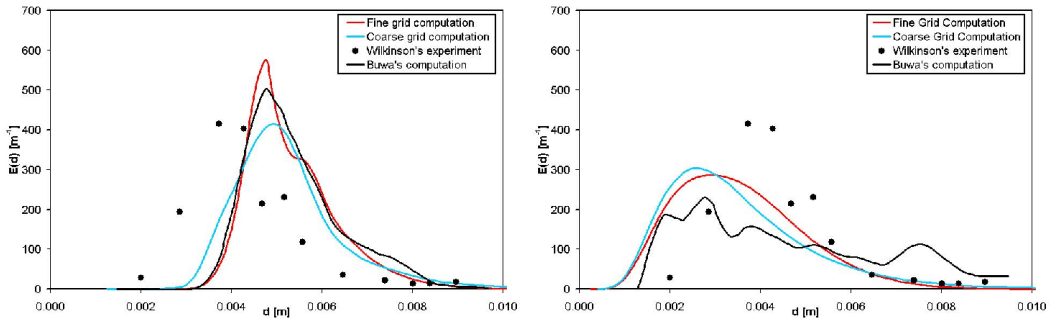

Figure 3.18: Comparison of case-1A's results with the reference results (Wilkinson [124] – experimental, Buwa and Ranade [19] – computational). Left: The first breakage kernel [28]. Right: The second breakage kernel [20].

size distribution corresponds to the average over the whole reactor, so it does not necessarily reflect the true equilibrium of the bubble breakage and coalescence. Our comparison has been performed on the basis of the bubble number fraction normalized with the group width, $E(d)$, for

both adopted breakage models. Our computational predictions are in a good agreement with the experimental results of Wilkinson and correlate well with the computational results obtained by Buwa and Ranade (especially in the case of the first breakage kernel [28]) for the same problem and for the same model, see Figure 3.18.

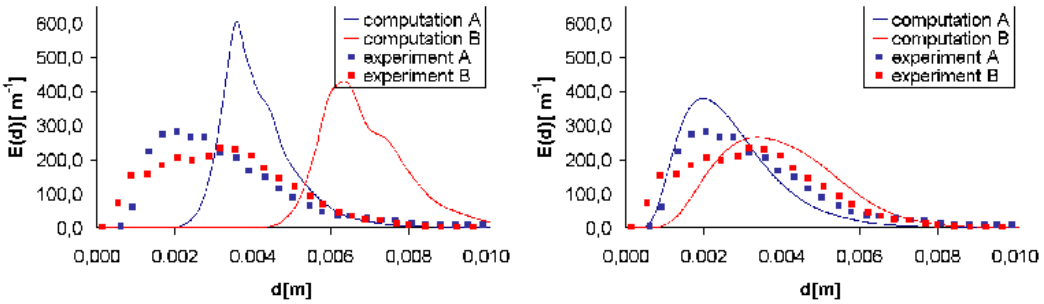

Figure 3.19: Comparison of case-1B's and case-1C's results with the experimental results by Grienberger and Hofmann [125], and by Schrag [126]. Left: The first breakage kernel [28]. Right: The second breakage kernel [20].

In Figure 3.19, experimental data which were measured by Grienberger and Hofmann [125] and by Schrag [126] are presented and compared to our computational predictions. The experiments were conducted with air–water multiphase flow for different values of superficial gas velocities $j_g^B = 0.08\,\mathrm{ms}^{-1}$ and $j_g^C = 0.02\,\mathrm{ms}^{-1}$ which corresponds to dissipation rates of $0.196\,\mathrm{m}^2\mathrm{s}^{-3}$ and $0.785\,\mathrm{m}^2\mathrm{s}^{-3}$, respectively. The representative quality of the results was chosen to be the "normalized number of bubbles per fraction width", $E(d)$. We obtained a good agreement between the results of our numerical calculations and the presented experimental results, Figure 3.19. This comparison leads us to conclude that the model by Lehr *et al.* [20] is a more suitable candidate for our CFD coupled PBE model because *(i)* its convergence behavior with the grid refinement is better such that with $q = 1.5$ qualitatively converged results can be obtained, i.e. a grid of 35 classes is sufficient to cover a fairly large domain and to get grid independent results, Figure 3.17; *(ii)* it can predict the experimental results more accurately in a wider range of operating conditions, see Figure 3.19.

Comparison of MC and PPDC

The pure coalescence and simultaneous coalescence-breakage phenomena have been studied with the hypothetical breakage kernels in section 3.4.1 with both PPDC and MC. The results have shown that one needs a very small discretization constant, $q \approx 1.01$, for a sufficiently accurate results within MC; although, computations with such small q can be easily affordable for 0D problems, it is not reasonable for the computation of CFD coupled PBE in 3D. Here, the MC and PDDC are studied with physical kernels in order to compare the convergence of the methods.

In section 3.4.2, we showed that obtaining converged results are possible with $q = 1.35$ for the second breakage kernel [20] in studies of case-1A. However, there is no evident that the converged result is sufficiently accurate; therefore, we simulated case-1A by adopting PPDC whose accuracy was shown to be better by studying the hypothetical kernels, section 3.4.1 So that, we aim to have more accurate results by using PPDC and compare the results with MC against those.

Before progressing to the results of the simulations for case-1A, one point has to be clarified:

why only 100 breakage daughter classes was chosen; the implementation of breakage kernel was comprehensively explained within PPDC but this point. In the studies of Bove et al. [9, 97] the implementation detail of PPDC for the breakage is not given, how to define the breakage daughter classes is not described. Since the PPDC algorithm is conservative for the first $2n$ moments, the chosen definition of the breakage daughter classes has to be moment conservative, as well. Thus, we could not adopt the same definition of classes from our implementation of MC but a similar approach is adopted: considering the computational cost, a piecewise-constant approximation (PCA) of values on an equidistant grid is adopted; the accuracy of the adopted approach is checked with a comparison of a more sophisticated approximation.

The definition of the breakage daughter classes should satisfy two requirements. First, the numerical solution of PBE should be conservative in number (-density) and volume/mass with the defined daughter classes, and the probability of a certain bubble/droplet breaking to a daughter whose size is between the limits of a certain class should be accurately calculated. To satisfy the first requirement the equidistant grid (classes with equal width) is adopted and to satisfy a predetermined accuracy, a certain number of daughter classes is chosen, 100.

The required number of daughter classes is determined as follows: *(i)* the breakage of significantly different sized bubbles (air in water) are chosen, volume of υ, $8 \times \upsilon$ and $512 \times \upsilon$; *(ii)* the breakage kernel from Martińez–Bazań et al. [23, 24] was studied, equation 3.2.16; *(iii)* the obtained results are compared with reference results which are obtained with an error of 10^{-6} by using recursive adaptive Simpson quadrature (RASQ); the results are presented in Figure 3.20.[6]

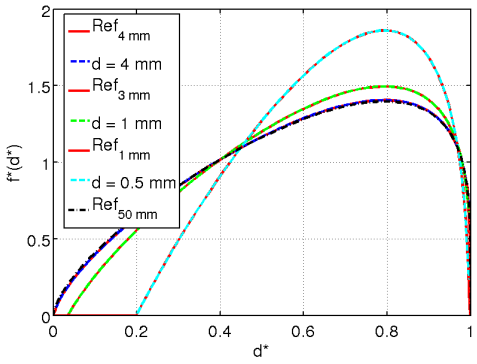

Figure 3.20: Probability density functions of the daughter bubbles for varying parent sizes and $\varepsilon = 1000 m^2 s^{-3}$ with two numerical approaches: RASQ (curves Ref_x) and PCA.

The results that are obtained with RASQ and PCA are in agreement, with respect to the comparison of the solid and dashed curves in Figure 3.20; the results are qualitatively identical. Moreover, these cases are studied by Martińez–Bazań et al. [24], and our results agree with theirs, as well. The black curve ($D_0 = 50\,\text{mm}$) does not differ more than the blue curve ($D_0 = 4\,\text{mm}$), this shows that when the parent bubble is larger than a certain bubble size (under certain operating conditions), the p.d.f of larger bubbles does negligibly vary, see the curves for 0.5 mm, 1 mm, 3 mm, 4 mm and 50 mm. Consequently, these results verify that the suggested approaches to define the breakage daughter classes are sufficiently accurate in a wide range of parent class's size such that the ratio of the limits is 10^6.

As our approach to implement PPDC is completely verified, we can go on with the results of

[6] For visualization purposes, the plot data is linearly interpolated.

the numerical computations for the case-1A. Case-1A is studied with PPDC and MC; two, three and four parent classes were employed within PPDC, and q was set to 1.35 within MC. Then, the results are compared in time for the variables: number density (d_0), interfacial area density (*iad*) $d_{(23)}$, Sauter mean diameter (d_{32}), and volume averaged diameter(d_{43}), see Figure 3.21 and Figure 3.22.

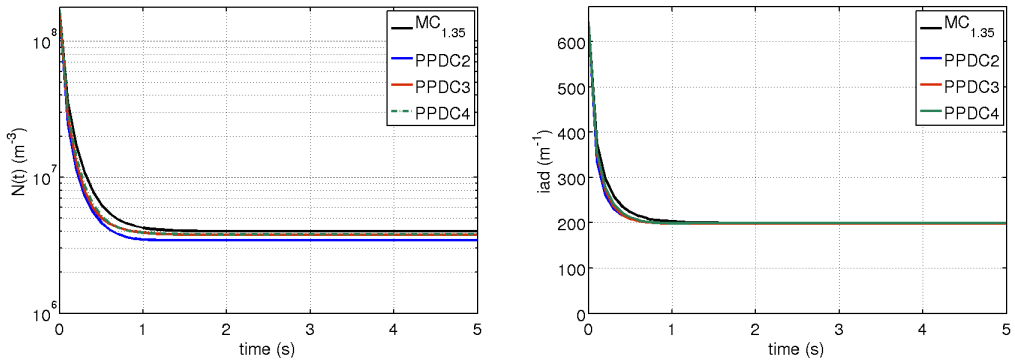

Figure 3.21: Comparison of the total number density and interfacial area density results which are obtained with MC and PPDC for $q = 1.35$ and 2,3 and 4 parent classes, respectively.

The first results are promising: the value of q does not need be as small as in the case of hypothetical kernels, Figure 3.14, and the value of $q = 1.35$, which is sufficient to obtain a converged result in previous computations (Figure 3.17) leads us to agreeing results with PPDC in this case, Figure 3.21. While the difference between the results of $N(t)$ is more visible, the results for *iad* are almost identical. Since the results for *iad* are related to the higher order moments than the total number density, we also checked other variables related to the higher order moments, d_{32} and d_{43}, which are also more interesting than the number density for the engineering applications.

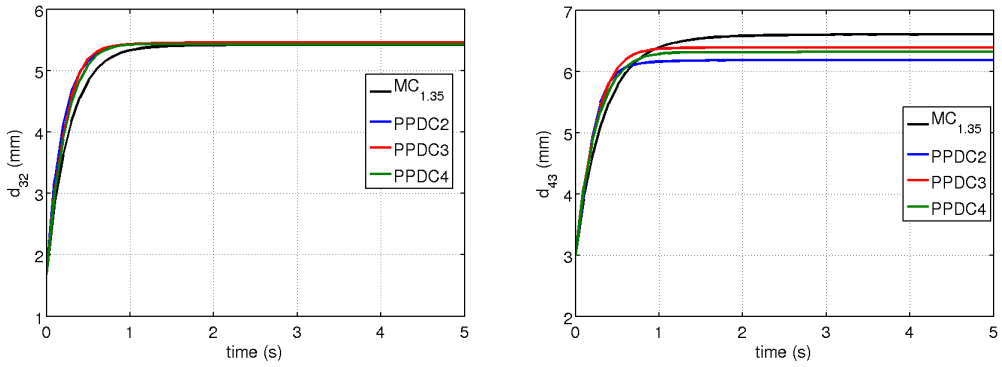

Figure 3.22: Comparison of the d_{32} and d_{43} results which are obtained with MC and PPDC for $q = 1.35$, and 2, 3 and 4 parent classes, respectively.

The results for d_{32} are more satisfactory with respect to the ones for d_{43}. This consequence was expectable, the accuracy of the MC reduces as the moment's order of interest gets further than the 3rd order; nevertheless, the variables, d_{32} and d_{43}, which have great importance for the engineering applications can be very precisely predicted with the both methods, MC and PPDC, Figure 3.21 and Figure 3.22.

Figure 3.21 and Figure 3.22 presents the qualitative comparison of the results; still, it can be

interesting to have a quantitative comparison. Since, there was neither experimental nor numerical reference-results, we had the following approach for the quantitative comparison of the results: We compare the fractional order of moments against two reference results which are obtained with *i)* MC with $q = 1.35$, *ii)* PPDC with five parent classes.

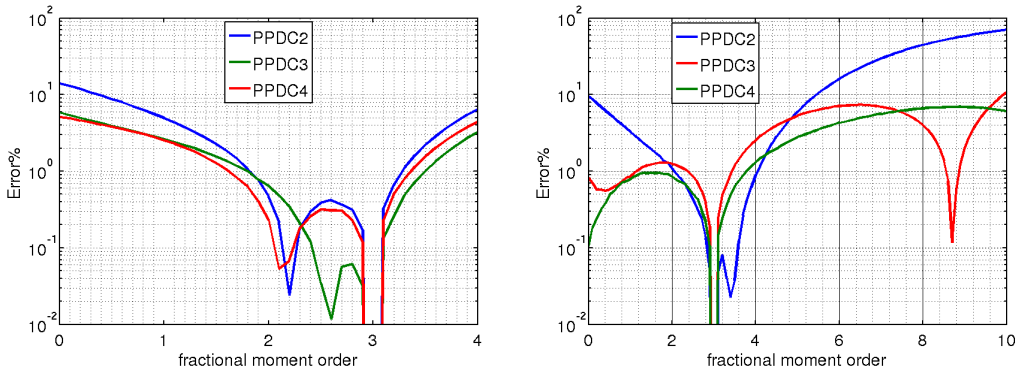

Figure 3.23: Relative error for PPDC against MC (left) and PPDC5 (right).

Fractional moment order values of the steady-state solution are obtained with MC ($q = 1.35$) and with PPDC for 2–5 parent classes (the results are denoted as PPDC*X*). The relative errors which are obtained for PPDC show that the results with two parent classes (PPDC2) are significantly different than the second reference, Figure 3.23 (right); nevertheless, PPDC3 and PPDC4 differ from the second reference less than 2% for the first four moment orders, which are of interest. For the higher moment orders, as expected, the difference gets greater and reaches to 10% for the 10'th order moment which is not very important. It is clearly shown that discrepancies among the results reduce with increasing number of parent classes with PPDC. On the other hand, when the first reference result (MC, $q = 1.35$) is regarded, the error is on an acceptable range for the first 4 low-order moments which are of interest. Briefly, both methods lead to almost converged results with acceptable numbers of parent classes (PPDC) and the discretization constant (MC); q determined to be about 1.35 for converged results, even the value of 1.5 leads to the accurate results with the studied physical kernels in contrast to the case of the studied hypothetical kernels. The method of classes provides a smooth size distribution; whereas, PPDC requires to solve the ill-posed inverse problem to obtain the size distribution. PPDC is significantly more accurate for moment orders which are higher than four; nevertheless, since both methods have a similar accuracy for the first 4 order moments which are mostly of our concern, the accuracy is not the predominant criteria on choosing either.

Comparison of theoretical and phenomenological kernels

Theoretical kernels were not the only option, we also adopted a phenomenological breakage kernel by Martińez–Bazań et al. [23, 24] to close PBE and to simulate breakage- and coalescence-dominant cases. The phenomenological kernel is adopted by many researchers to simulate liquid-liquid [129] and gas-liquid [12] dispersions and is also considered as a milestone in reviews of bubble/droplet breakup of immiscible turbulent flows [13, 131].

Case-1A is studied with the later breakage kernel from Lehr et al. (the first kernel) (3.2.11)–(3.2.12) and Martińez–Bazań et al. (the second kernel) (3.2.15)–(3.2.16) within PPDC method for 2, 3 and 4 parent classes with an initial condition which is prescribed in one parent class whose size is set to 1.67 mm, Figure 3.24. Later, the initial condition has changed to $d = 6.43$ mm; so that, a

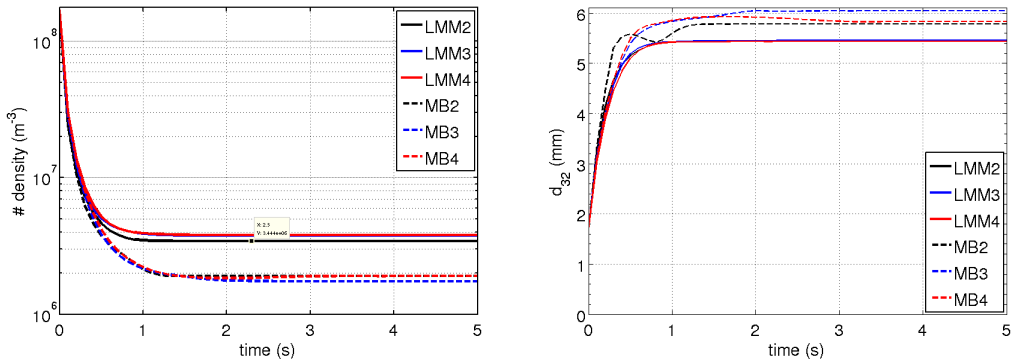

Figure 3.24: Comparison of results with breakage kernels from Lehr et al. (LMM) and Martińez–Bazań et al. (MB) for case-1A: total number density (left) and Sauter mean diameter (right).

breakage dominant case is simulated whose results are compared with the previously studied case which was a coalescence dominant case, Figure 3.25.

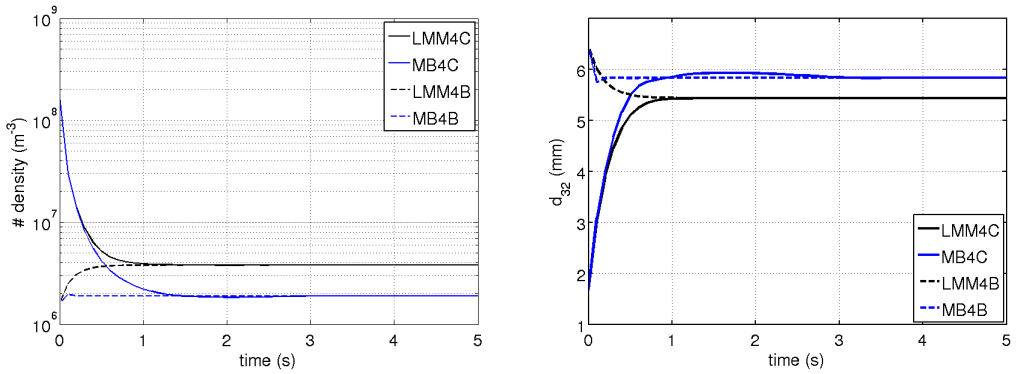

Figure 3.25: Comparison of results with breakage kernels from Lehr et al. (LMM) and Martińez–Bazań et al. (MB) for breakage- and coalescence-dominant cases: total number density (left) and Sauter mean diameter (right).

Either breakage kernel has its own converged results in time and in number of parent classes (*npc*). The steady state results are obtained for both kernels and for every number of parent classes; nevertheless, while the steady state solutions of the PBE with the second kernel were obtained for different *npc* at significantly different times: 3.3 s, 2.6 s and 1.5 s, with the first kernel the numerical solutions converged to steady state about 1 s for every *npc* regardless of the initial condition, i.e. either in coalescence-dominant cases or in breakage dominant cases the numerical solutions converged to the same steady-state solution, Figure 3.25.

The steady-state solution of the PBE can be described as a dynamic equilibrium in which the coalescence and breakage phenomena still occur but the size distribution of the secondary phase does not change. The first kernel predicts the Sauter mean diameter of the population at the equilibrium smaller than the other does, Figure 3.24–3.25. In these figures, we also see that the convergence behavior of the solutions is better with the first kernel. This is a good reason to prefer to work with this kernel; moreover, in general the numerical solution of PBE overpredicts the size distribution of the secondary phase comparing to the experimental data, which is another reason to adopt the first kernel.

Experiments by Olmos et al. and Laakkonen et al.

The validity range of the kernels for operating conditions is always an issue in population balance models. Some kernels can be very accurate for a narrow range and have very poor prediction out of this range. Theoretical kernels typically have a broader operation range since they do not involve (free-) parameters which (should be) have been found out according the experimental data. We test our kernels against the experiments which are conducted by Olmos et al. [128] and Laakkonen et al. [127] in order to see their accuracy for various operating conditions and physical properties.

Olmos et al. combine population balance equations to a classical hydrodynamic Euler–Euler simulation to investigate the operation of a cylindrical bubble column in a commercial software-package (ANSYS CFX-4.3) for various superficial gas velocities. On the other hand, Laakkonen et al. numerically and experimentally studied the stirred tanks for different dispersed systems: air–water, air–1-propanol and air–diethylene glycol. The former study concerns the low turbulent flow whereas the later one is focused on the high turbulent flows, and the both studies present comprehensive experimental and numerical data for the comparison.

Olmos et al.'s studies concern low- and mild-turbulent flows in a cylindrical bubble column for different superficial gas velocities. Their detailed numerical simulations and experiments allowed them to characterize the occurring dispersed flow regimes, and they could also determine the global mean diameter in both the experiments and the numerical simulations. This is very interesting for us because by adopting the simple relation (3.4.2) between the superficial gas velocity and the turbulent dissipation rate in bubble columns from Lehr and Mewes [28] we can roughly simulate the evolution of the secondary-phase's mean distribution in time without resolving the flow field:

$$\varepsilon = j_g\, g \tag{3.4.2}$$

So, we simulated the cases from their study and compared our results against theirs, Figure 3.26.

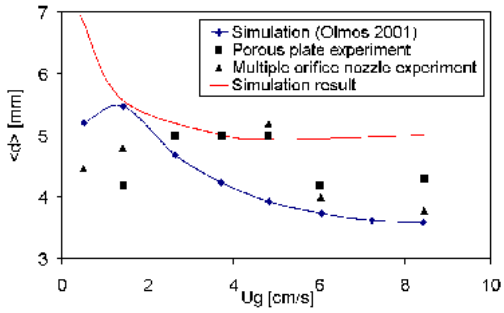

Figure 3.26: Comparison between experimental and numerical results by Olmos [128] and this study.

The results show that even with a roughly determined ε, for the moderate superficial gas velocities the numerical solutions of PBE yield to accurate predictions of the experimental results. The flow field is not homogeneous for the low superficial gas velocities [128], this can be one of the reasons for large discrepancy between the numerical and experimental results. Moreover, the empirical relation (3.4.2) can be less accurate for high u_g, and in the highly turbulent flow-regions occurring very small droplets significantly reduces the global mean diameter, which can not be simulated in our approach, thus the experimental results were overpredicted.

Laakkonen et al. studied the local bubble size distributions (BSD) for dense air–water and CO_2–n-butanol dispersions under hydrodynamic conditions characterized by high turbulent dissi-

pation rates. They measured the BSD at different regions of the Rushton turbine agitated dispersions in stirred tanks ($14/200\,L$), and they adopted a numerical approach analogous to the compartment method in order to simulate the evaluation of the dispersed phase in time at the different regions of the stirred tanks, a multiblock strirred tank model. For extremely intense agitation, they considered that the stirring is ideal and the BSD does not spatially vary in the tank so the simulation of these cases is possible with a 0D model. They numerically simulated the cases which are experimentally studied by Hu et al. [132]; they also employed the kernel from Lehr et al. [20]. The experimental [132] and simulation results obtained in the reference study of Laakkonen *et al.* [127] together with our simulation results corresponding to the simulation-time of $50\,s$ are summarized in Table 3.3.

Table 3.3: Sauter mean diameters (mm)

Case	Hu *et al.*	Laakkonen *et al.*	Our study
air-water	0.447	0.359	0.358
air-1-propanol	0.316	0.207	0.205
air-diethylene glycol	0.598	0.251	0.250

The results are in good agreement with the reference study, in fact they are almost identical. Nevertheless, we want to remark that: The obtained equilibrium BSDs and the Sauter mean diameters are strongly dependent on the stopping criteria of the iterative scheme. Meaning, the final Sauter mean diameters may slightly change by changing the criteria for convergence resulting in different simulation times (smaller criterion longer simulation and vice versa). Accordingly, the graphs plotted in Figure 3.27 show the evolution of the Sauter mean diameter for two different time frames.

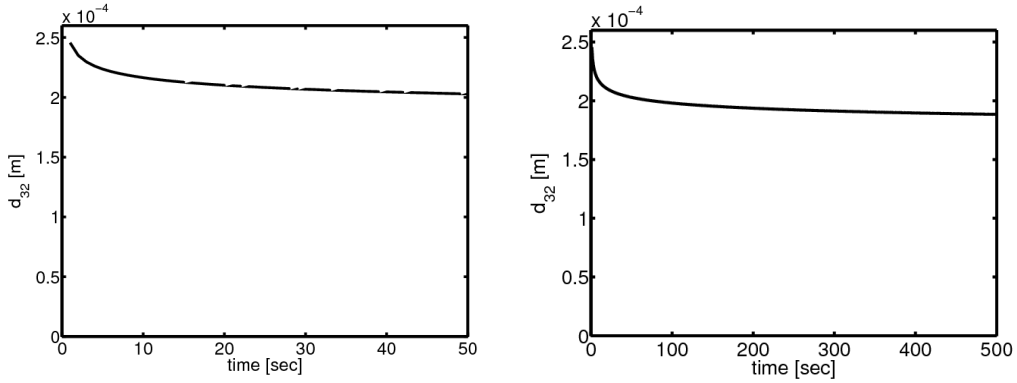

Figure 3.27: Case: air-1-propanol, for $50\,s$ and $500\,s$.

In Figure 3.27 (left), the convergence criteria – defined as the maximum relative change of gas holdup of all classes – is on the order of 10^{-7} while in Figure 3.27 (right), its value has been set to 10^{-8}. It is apparent from the graph corresponding to long time simulation, that the Sauter mean diameter is still changing. Such a behavior has been already described in the literature by Kostoglou [120]: The steady equilibrium state even for large time scales was not observed. According to the mentioned study and our observations the results tabulated in the original study of Laakkonen would have been more meaningful if the time scales had been specified.

Briefly, our numerical simulations have predicted the experimental results for d_{32} within a

reasonable error for a wide range of operating conditions and predict the same behavior as it has been stated in experimental studies. However, for very low turbulent dissipation rates and small gas holdups, predictions of the model get poorer due to inhomogeneous flow field. On the other hand, when the flow field and BSD do not significantly vary in the domain (which is the case for ideally agitated dispersions), even if the void fraction is low, the employed kernel from Lehr et al. [20] leads to very accurate results. Although, Laakkonen et al. shows that their phenomenological model is more accurate after a parameter fitting is accomplished for the free-parameters in the kernels, this is not a desirable remedy for us; because it requires large amount of experimental study to determine values of the free-parameters. As the inhomogeneous flow field can be resolved with comprehensive CFD simulations, numerical studies considering PBE coupled to CFD should significantly increase the accuracy of results.

4

PBE and CFD: One-way coupling

The dynamics of gas/liquid–liquid dispersed flows has been a topic of research for the last several decades and many different methods were developed. Numerical simulation of the dispersed flows is a cumbersome problem due to high complexity of the flow field and can be possible by adopting the Euler–Euler (E–E) or Euler–Lagrange (E–L) approaches. For practical reasons like avoiding high numerical efforts and computational costs which are related to tracking and calculating the motion of each bubble individually in the flow field, the former method is restricted to be applied when low volume fractions of the dispersed phase are considered. While the latter method requires comparatively small efforts in both numerics and computation; nevertheless, both of the methods lead to the same results if the problems are handled with adequate computational effort [134].

Each single droplet[1] is tracked within the E–L approach so that an appropriate mathematical model can describe the coalescence and breakage phenomena implicitly without statistically modeling these phenomena, i.e. without population balance models. However, if the system which is desired to be numerically simulated consists of enormous number of droplets, E–E approach should be adopted; then, it is required to explicitly describe the evolution of the size distribution with PBE. Consequently, we are faced to a multifaceted problem: solution of coupled CFD-PBE model.

When the laminar dispersed flows are considered for liquids with similar densities, we are left with a trivial problem: there will be no breakage due to absence of turbulent eddies; and droplets follow the streamlines and they do not coalesce. Therefore, we will focus on the turbulent dispersed flows in which the colliding turbulent eddies on the droplet surface result in breakage, and the eddies of larger size than the droplet transports and give rise to coalescence.

The numerical simulation of turbulent flows is a very challenging subject. The mathematical models describing the turbulent flows are mostly very demanding in computational effort and

[1] Since one-way coupled PBE–CFD models are mostly employed to describe liquid–liquid dispersed systems, we adopt the word “droplet” through this section; nevertheless, the reader can freely refer to the bubbles, as well. When this does not hold and it is not clear from the context, it is explicitly mentioned.

require highly accurate numerical techniques: very fine spatial grid and small time-steps, high-order stabilization schemes, implicit numerical methods, positivity-preserving linearization.

The turbulence models deviate in a wide range from zero-equation (algebraic) models to second order models (Reynolds Stress Models). Turbulence models which are applicable to produce results with an acceptable accuracy and reasonable computational cost in general originate from the family of two-equation eddy viscosity models. The most preferred model in this sense is related to the standard or modified $k-\varepsilon$ turbulence models which have been implemented in several commercial CFD programs and in-house codes. In most of the present studies which consider implementation of CFD coupled with PBE, it is preferred to work with commercial codes, .e.g. Parsival, Ansys CFX. In our study, the turbulence is described within a *Reynolds Average Navier-Stokes* (RANS) approach by adopting a modified k$-\varepsilon$ model: Chien's Low-Reynolds Number $k-\varepsilon$ model [133].

Difficulties in the numerical solution of the PBE have been discussed in detail in *Section 3*. Additional to those difficulties in numerical simulations of dispersed flows, the mathematical model describing our problem has a rather interlocking structure. The external and internal couplings in this interlocked structure cause high non-linearities for which a carefully-planned nested-loop strategy is required in order to obtain accurate results with reasonable amount of computational effort.

Size distribution of the secondary phase has a certain influence on the flow field; however, when the density and viscosity of the two fluids are similar, and the holdup of the secondary phase is low, one can assume that both phases share the same velocity field. So that, we can couple the PBE with CFD in a one-way fashion: The flow field influences the size distribution of the secondary phase but size distribution has no effect on the flow field. This assumption yields further significant simplifications and is important from the aspect that the uncertainties/errors in the solution of the PBE will not influence the flow solution, and cases with well known solutions of the flow field can be employed to test our coupled PBE-CFD implementation.

The studied test cases involve a channel flow, a pipe flow and static mixer applications. The channel flow is a case study to test the accuracy of the employed stabilization scheme; the pipe flow case-study concerns the transient simulation of population balances and flow field. The last case is a rigorous numerical and experimental study in which flows with varying flow-rate- and holdup-values through Sulzer SMV™ static-mixer-elements are considered. So that, the one-way coupled PBE-CFD implementation is validated and verified by comparing the obtained numerical results against experimental ones.

4.1. Mathematical modeling and numerical treatment

The evolution of the dispersed phase in a turbulent flow field occurs in time, space and internal coordinates according to the hydrodynamic quantities and physical properties of the dispersed phase system. In the E-E approach, the governing equation of the dispersed system in a turbulent flow field can be written as an inhomogeneous unsteady transport equation

$$\frac{\partial f}{\partial t} + \mathbf{u}_{\mathrm{D}} \cdot \nabla f = B^{+} + B^{-} + C^{+} + C^{-}. \tag{4.1.1}$$

This equation (4.1.1) is a transport equation for liquid/gas–liquid flows in terms of the number density probability function, f, of drops. By definition, f needs to be related to an internal coor-

dinate, what in most of the cases is the volume of bubbles, υ. So that, the number density, N, and void fraction, α, of bubbles having a volume between υ_a and υ_b are:

$$N_{ab} = \int_{\upsilon_a}^{\upsilon_b} f\, d\upsilon, \quad \alpha_{ab} = \int_{\upsilon_a}^{\upsilon_b} f\upsilon\, d\upsilon \tag{4.1.2}$$

While the considered transport phenomena account for convection in spatial space (governed by the flow field $\mathbf{u}_\mathrm{D}$ in (4.1.1)), the breakage and coalescence transport drops in the internal coordinate (governed by the PBE). This is why, the attempt on describing the liquid/gas–liquid flows requires the coupling of the PBE and fluid dynamics; moreover, since the flow field in our scope which is characterized as turbulent can not be numerically simulated in a direct numerical simulation (DNS) fashion, the turbulence model has to be incorporated in order to account for the unresolved flow features.

Let us recall Figure 2.1, we see that the complete mathematical model involves three parts

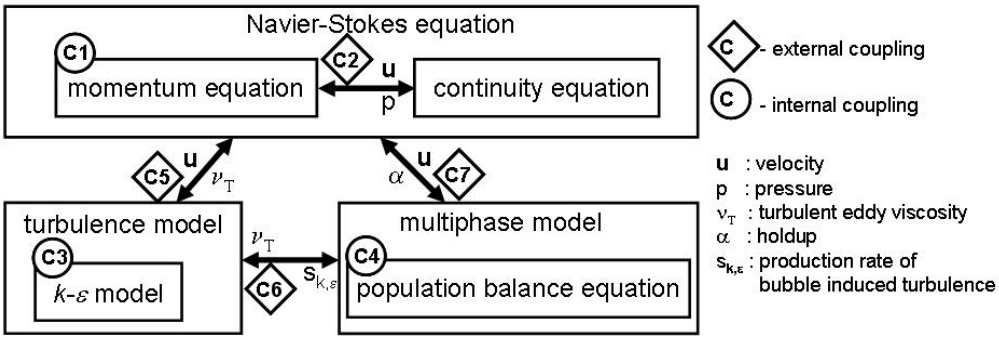

(i) the Navier-Stokes equations (N-S), *(ii)* the turbulence model, *(iii)* the population balance model; and external couplings among these parts additional to internal couplings of the each part. This sketch gives an idea about nonlinearity of the complete model. The internal couplings (*C2*, *C3* and *C4*) are very strong and they have to be treated either in a coupled fashion, e.g. Galerkin schemes for N-S, or should be decoupled and treated in a non-linear loop, e.g., Projection schemes for N-S. The *C5* coupling, which is also strong, associates the Navier-Stokes equations with the turbulence model and requires the equations to be solved in an iterative manner. Meanwhile, as a consequence of multiphase modeling, one has to be aware of even more complex coupling effects due to buoyancy (*C6*) and enhanced turbulence effects (*C7*). Furthermore, the turbulence and the multiphase model is coupled by means of the flow field with the Navier-Stokes equations (*C5* and *C7*); which all results in a rather interlocking structure. To cope appropriately with the described strongly coupled system is quite challenging and may result in unavoidably increased computational cost. Therefore, in this work the coupling effects are relaxed by not taking into account the influence of the turbulence induced by the secondary phase (also known as bubble induced turbulence in gas-liquid systems) and by neglecting the buoyancy forces. Consequently,a one-way coupled model arises, which is valid for pressure driven and shear induced turbulence dominating systems.

The fluid dynamics is described by the RANS equations of the following form

$$\begin{aligned} &\frac{\partial \mathbf{u}}{\partial t} + \mathbf{u}\cdot\nabla\mathbf{u} - \nabla\cdot\left((\nu+\nu_T)[\nabla\mathbf{u}+\nabla\mathbf{u}^T]\right) + \nabla p = \mathbf{f}, \\ &\nabla\cdot\mathbf{u} = 0, \end{aligned} \tag{4.1.3}$$

where ν depends only on the physical properties of the fluid, while ν_T (turbulent eddy viscosity) is supposed to emulate the effects of the unresolved velocity fluctuations $\mathbf{u}'$. According to Chien's

Low-Reynolds Number modification of the $k-\varepsilon$ model, the eddy viscosity has the following definition

$$\nu_T = C_\mu f_\mu \frac{k^2}{\tilde{\varepsilon}} \quad \text{with} \quad \tilde{\varepsilon} = \varepsilon - 2\nu\frac{k}{y^2}, \tag{4.1.4}$$

where k is the turbulent kinetic energy, ε is the dissipation rate and y is the closest distance to the wall [133]. Clearly enough, for computations of k and ε the above PDE system is to be complemented by two additional mutually coupled convection-diffusion-reaction equations [135]. For our purposes, it is worthwhile to introduce a linearization parameter $\gamma = \tau_T^{-1} = \tilde{\varepsilon}/k$, which is related to the turbulent time scale τ_T and which makes it possible to decouple the transport equations as in (4.1.5)–(4.1.6) [136].

$$\frac{\partial k}{\partial t} + \nabla\cdot\left(k\mathbf{u} - \frac{\nu_T}{\sigma_k}\nabla k\right) + \alpha k = P_k, \tag{4.1.5}$$

$$\frac{\partial \tilde{\varepsilon}}{\partial t} + \nabla\cdot\left(\tilde{\varepsilon}\mathbf{u} - \frac{\nu_T}{\sigma_\varepsilon}\nabla\tilde{\varepsilon}\right) + \beta\tilde{\varepsilon} = \gamma C_1 f_1 P_k. \tag{4.1.6}$$

The involved coefficients in equations (4.1.5)–(4.1.6) are given by

$$\begin{aligned} &\alpha = \gamma + \frac{2\nu}{y^2}, \quad \beta = C_2 f_2 \gamma + \frac{2\nu}{y^2}\exp(-0.5y^+), \quad P_k = \frac{\nu_T}{2}|\nabla\mathbf{u} + \nabla\mathbf{u}^T|^2, \\ &f_\mu = 1 - \exp(-0.0115y^+), \quad f_1 = 1, \quad f_2 = 1 - 0.22\exp -\left(\frac{k^2}{6\nu\tilde{\varepsilon}}\right)^2. \end{aligned} \tag{4.1.7}$$

In the one-way coupled approach the dispersed phase is considered to be advected with the same velocity as the continous phase, so the dispersed phase velocity $\mathbf{u}_\mathrm{D}$ in (4.1.1) can be replaced with $\mathbf{u}$; and, when the source and sink terms are written explicitly, the governing equation for the dispersed phase follows as

$$\begin{aligned} \frac{\partial f}{\partial t} + \mathbf{u}\cdot\nabla f = &\int_\upsilon^\infty r^B(\upsilon,\tilde{\upsilon}) f(\tilde{\upsilon})\, d\tilde{\upsilon} - \frac{f(\upsilon)}{\upsilon}\int_0^\upsilon \tilde{\upsilon} r^B(\tilde{\upsilon},\upsilon)\, d\tilde{\upsilon} \\ &+ \frac{1}{2}\int_0^\upsilon r^C(\tilde{\upsilon},\upsilon-\tilde{\upsilon}) f(\tilde{\upsilon}) f(\upsilon-\tilde{\upsilon})\, d\tilde{\upsilon} - f(\upsilon)\int_0^\infty r^C(\tilde{\upsilon},\upsilon) f(\tilde{\upsilon})\, d\tilde{\upsilon}. \end{aligned} \tag{4.1.8}$$

Nevertheless, the fluid dynamics has been described with a turbulence model; and according to the (temporal) averaging concepts, equation (4.1.8) has to be extended with the arising pseudo diffusion terms in analogy to the approach of the Reynolds stress tensor, $\nabla\cdot\overline{u'f'} = -\nabla\cdot(\frac{\nu_T}{\sigma_T}\nabla\overline{f})$, where σ_T is the so-called turbulent Schmidt number which is equal to 1 for spherical particles/drops. Then, the governing equation is extended with the diffusion term, even though the dispersed phase is not diffusive in nature.

$$\begin{aligned} \frac{\partial f}{\partial t} + \mathbf{u}\cdot\nabla f - \nabla\cdot(\nu_T\nabla f) = &\frac{1}{2}\int_0^\upsilon r^C(\tilde{\upsilon},\upsilon-\tilde{\upsilon}) f(\tilde{\upsilon}) f(\upsilon-\tilde{\upsilon})\, d\tilde{\upsilon} \\ &- f(\upsilon)\int_0^\infty r^C(\tilde{\upsilon},\upsilon) f(\tilde{\upsilon})\, d\tilde{\upsilon} + \int_\upsilon^\infty r^B(\upsilon,\tilde{\upsilon}) f(\tilde{\upsilon})\, d\tilde{\upsilon} - \frac{f(\upsilon)}{\upsilon}\int_0^\upsilon \tilde{\upsilon} r^B(\tilde{\upsilon},\upsilon)\, d\tilde{\upsilon} \end{aligned} \tag{4.1.9}$$

Equation (4.1.9) has to be closed with the appropriate definitions of the breakage and coalescence kernels (r^B and r^C respectively). In *Section 3*, we discussed this issue in detail and decided to employ the kernels from the study by Lehr et al. [20]. So that, the equation describing the turbulent dispersed phase motion in a one-way coupled fashion with Euler-Euler approach has been closed, and we can progress with a discussion on numerical solutions of (4.1.9).

4.1.1. Initial and boundary conditions

Governing equations are the mathematical description of physical phenomena; when they are prescribed with specific initial and boundary conditions in a certain spatial domain ($\Omega \subset \mathbb{R}^d$) and a given time interval ($[0,T]$), they describe a certain problem. Despite of their importance, initial and boundary conditions are rarely discussed in detail.

We followed the studies by Turek [137], Hysing [138] and Kuzmin et al [139] on the discussion of the initial and boundary conditions. Usually two distinct boundary conditions suffices to prescribe a problem: the Dirichlet condition and the Neumann condition. While the first one specify the value of a variable on the corresponding part of the boundary ($\partial\Omega_D$), the later determines the in- or out-flux at the respective part ($\partial\Omega_N$).

Boundary conditions for Navier-Stokes equations need to be given for the velocity variable and the pressure; the Dirichlet condition, usually, is used to prescribe the inflow and the (no-)slip condition at the inlet and on the impermeable walls, respectively (4.1.10).

$$\mathbf{u} = \mathbf{u}_D \quad \text{on} \quad \partial\Omega_D \tag{4.1.10}$$

On the other hand, it is a very common practice to set zero stress ($h^* = 0$) as a special case of Neumann condition on the outlet part of the domain in order to prescribe the outflow (4.1.11).

$$\hat{\mathbf{n}} \cdot (\nabla\mathbf{u} + \nabla\mathbf{u}^T) = h^* \quad \text{on} \quad \partial\Omega_N \tag{4.1.11}$$

The adopted Chien's turbulence model offers the advantage of simple boundary conditions on the walls ($\Gamma_w \subset \partial\Omega_D$):

$$\mathbf{u} = 0, \quad k = 0, \quad \tilde{\varepsilon} = 0 \quad \text{on} \quad \Gamma_w.$$

While the initial definition can be easily set for the velocity field (4.1.12), for turbulence variables it is not so; it is rather complicated to prescribe the proper initial conditions of the turbulence variables for a transient solution.

$$\mathbf{u}(\mathbf{x},0) = \mathbf{u}_0(\mathbf{x}) \tag{4.1.12}$$

If the velocity field is initialized with $\mathbf{u}_0(\mathbf{x}) = 0$, the flow is initially not turbulent and takes a certain time for the turbulent flow to develop, say t^*. When $t < t^*$, the flow is simulated by solving only incompressible nonstationary Navier-Stokes equations with a predefined constant effective viscosity ν_0. And, the initial values of k and ε at $t = t^*$ can be given depending on the default mixing length l_0 and ν_0 as follows,

$$k_0 = \left(\frac{\nu_0}{l_0}\right)^2, \qquad \varepsilon_0 = C_\mu \frac{k_0^{3/2}}{l_0} \qquad \text{for } t \le t^*. \tag{4.1.13}$$

4.2. Numerical treatment

The left hand side of equation (4.1.8) is very well known to researcher from CFD world, and the right hand side concerns the experts in the PBE field; and the researchers of these fields are engaged in the numerical solutions of these equations. The numerical solution of Navier-Stokes equations has been a research topic for more than half a century and many researchers with different backgrounds, e.g., mathematicians, physicists, engineers, computer scientists, have still been

active on this topic. The numerical solution of PBE is considered in numerous studies with an extensive interest since 1960s, as it is presented in detail at *Chapter 3*.

Mathematical aspects of the problem to which the researchers in the CFD field faced are: *(i)* highly nonlinear systems of equations which involves unsteady partial differential equations to be solved within sophisticated domains, *(ii)* arising saddle-point problems because of the incompressibility constraint, *(iii)* local changes of the problem character in space and time, *(iv)* temporarily stiff systems of differential equations. [137]. These characteristics cause great challenges in numerical and computational solutions of the problem. Sophisticated domains and boundary layers require that the computational domain is represented with anisotropic spatial meshes which lead to systems of equations with huge number of unknowns; the solution of those are possible with only efficient iterative solvers. Moreover, the pair of discrete spaces for the velocity and pressure unknowns should not be any but rather satisfying the *LBB-condition*. CFD experts have been working to over come these solutions for decades, and one of the most remarkable and comprehensive study is by Turek [137] who presents a guideline how to get through with these challenges and implements his methodologies within the FEATFLOW CFD solver package, which is developed further through this study with a coupled PBE solver.

Numerical solutions of the turbulence models have been a research topic since 1970s; however, very few studies presented the implementation details with all the aspects [139]. Each employed numerical technique may be decisive on the accuracy of the solution; nevertheless, a positivity-preserving discretization with a high-order accurate FEM stabilization scheme for the nasty convective term has a predominant importance while solving both the turbulence equations (4.1.5)–(4.1.6) and the governing equation (4.1.9).

Our approach to the numerical solution of the equations is first to (semi-)discretize unsteady equations in time by using the standard $\theta-$scheme; then, the spatial discretization follows within FEM. And, in case of the one-way coupled CFD-PBE (4.1.9) the right hand side of the equation is computed by using either MC or PPDC.

4.2.1. Time stepping technique

The temporal discretization is, as a common practice, the first step in the numerical solution of unsteady partial differential equation. It requires the choice of an appropriate time stepping technique which needs to be not only accurate but also stable, easily realizable, and computationally efficient and robust. One of the several candidates is $\theta-$scheme which depending on the choice of the θ's value, leads to one of the following schemes: *(i)* Forward-Euler ($\theta = 0$) *(ii)* Crank-Nicholson ($\theta = 0.5$) *(iii)* Backward-Euler ($\theta = 1$) After applying the $\theta-$scheme to (4.1.3), the semi-discrete Navier-Stokes equations read as follows:

$$\begin{aligned}&\text{At time } t = t^n \text{ with time step } \Delta t = t^{n+1} - t^n \text{ for a given } \mathbf{u}^n,\\ &\text{then solve for } \mathbf{u} = \mathbf{u}^{n+1} \text{ and } p = p^{n+1}\\ &\qquad \frac{\mathbf{u}-\mathbf{u}^n}{\Delta t} + \theta\big[(\mathbf{u}\cdot\nabla)\mathbf{u} - \nabla\cdot\big((\nu+\nu_T)(\nabla\mathbf{u}+\nabla\mathbf{u}^T)\big)\big] + \nabla p = \mathbf{v}^{n+1}\\ &\qquad \nabla\cdot\mathbf{u} = 0\end{aligned} \tag{4.2.1}$$

where the right hand side is given by

$$\mathbf{v}^{n+1} = \theta\mathbf{f}^{n+1} + (1-\theta)\mathbf{f}^n - (1-\theta)\big[(\mathbf{u}^n\cdot\nabla)\mathbf{u}^n - \nabla\cdot\big((\nu+\nu_T)(\nabla\mathbf{u}^n + \nabla(\mathbf{u}^n)^T)\big)\big] \tag{4.2.2}$$

The other equations, (4.1.5)–(4.1.6) and (4.1.9), are discretized in time analogously to the explained procedure yet the application of $\theta-$scheme to (4.1.9) is not as straightforward as for the others and it will be presented in detail when the fully-discrete counterpart of the equation is given in the *Section 4.2.3*.

4.2.2. Spatial discretization

The spatial discretization is commonly realized by employing one of the following methods: finite difference (FDM), finite volume (FVM), and finite element methods (FEM); the last two are generally employed methods in today's CFD solver packages. Bayraktar et al. [167] had a detailed comparison of CFD solver packages which employ FVM (OpenFOAM), element based FVM (Ansys-CFX) and FEM (FEATFLOW-Q_2/P_1); and it was shown that the FEM based CFD-solver has a significant superiority in terms of the accuracy and the efficiency.

In the finite element discretization, firstly, the weak or variational formulation of the problem is obtained by integrating the equations in whole domain after multiplying them with the test functions ($\mathbf{v} = [v_1 v_2 ... v_d]$ and $\mathbf{v} \in \mathbb{R}^d$) of an appropriate finite element space, namely test function space. In order to reduce the smoothness requirements of the variables, the terms involving higher order derivatives can be integrated by using the Gaussian theorem (integration-by-part).

In order to present the finite element formulation of Navier-Stokes equations, we firstly define an inner product:

$$(\mathbf{u}, \mathbf{w}) = \int_\Omega \mathbf{u} \cdot \mathbf{w} d\Omega \,.$$

And, the weak formulation of Navier-Stokes equations can be obtained by applying the test functions through the defined inner product to (4.1.3)

$$\begin{aligned} \int_\Omega \frac{\partial \mathbf{u}}{\partial t} \cdot \mathbf{v} d\Omega + \int_\Omega (\mathbf{u} \cdot \nabla)\mathbf{u} \cdot \mathbf{v} d\Omega = \int_\Omega \nabla p \cdot \mathbf{v} d\Omega + \\ \underbrace{\int_\Omega \nabla \cdot \left((\nu + \nu_T)[\nabla \mathbf{u} + \nabla \mathbf{u}^T] \right) \cdot \mathbf{v} d\Omega}_{\textbf{Diffusion term}} + \int_\Omega \mathbf{f} \cdot \mathbf{v} d\Omega \,, \\ \int_\Omega (\nabla \cdot \mathbf{u})\, q \, d\Omega = 0 \,. \end{aligned} \tag{4.2.3}$$

With the following definition of trilinear, bilinear and linear forms (in order)

$$\begin{aligned} c(\mathbf{u}, \mathbf{v}, \mathbf{w}) &:= \int_\Omega (\mathbf{u} \nabla)\mathbf{v}\, \mathbf{w} d\Omega \,, \\ a(\zeta, \mathbf{u}, \mathbf{v}) &:= \int_\Omega \zeta [\nabla \mathbf{u} + \nabla \mathbf{u}^T] \cdot \nabla \mathbf{v} d\Omega = (\zeta [\nabla \mathbf{u} + \nabla \mathbf{u}^T], \nabla \mathbf{v}) \,, \\ b(q, \mathbf{v}) &:= \int_\Omega q \nabla \cdot \mathbf{v} d\Omega \,, \end{aligned}$$

equation (4.2.3) can be written in a more compact form as

$$\begin{aligned} \left(\frac{\partial \mathbf{u}}{\partial t}, \mathbf{v} \right) + c(\mathbf{u}, \mathbf{u}, \mathbf{v}) + \overbrace{a(\nu, \mathbf{u}, \mathbf{v}) + f(h, \mathbf{v})}^{\textbf{Diffusion term}} - b(p, \mathbf{v}) = (\mathbf{f}, \mathbf{v}) \\ b(q, \mathbf{u}) = 0 \end{aligned} \tag{4.2.4}$$

where $f(h,v)$ is the arising surface/line integral as a result of applying integration by part on the diffusion term

$$f(h,\mathbf{v}) = \int_{\partial\Omega_N} h\cdot\mathbf{v}dS,$$

and the value of the flux $h = -(\nu\nabla\mathbf{u})\cdot\mathbf{n}$ is provided with the Neumann boundary condition on the boundary part $\partial\Omega_N$; we extend the discussion on the term f after the discrete counterpart is obtained.

First, the time-discretization is applied to (4.2.4) in accordance with (4.2.1)–(4.2.2) ($\mathbf{u} = \mathbf{u}^{n+1}$ and $p = p^{n+1}$).

$$\begin{aligned}(\mathbf{u},\mathbf{v}) + \Delta t\theta n(\nu,\mathbf{u},\mathbf{v}) - \Delta t\theta b(p,v) = \Delta t\theta\big((\mathbf{f}^{n+1},\mathbf{v}) - f(h^{n+1},\mathbf{v})\big)\\ + (\mathbf{u}^n,\mathbf{v}) + \Delta t(1-\theta)\big(b(p^n,v) + (\mathbf{f}^n,\mathbf{v}) + n(\nu,\mathbf{u}^n,\mathbf{v}) - f(h^n,\mathbf{v})\big)\end{aligned} \quad (4.2.5)$$

where $n(\nu,\mathbf{u},\mathbf{v}) := c(\mathbf{u},\mathbf{u},\mathbf{v}) + a(\nu,\mathbf{u},\mathbf{v})$. Treating explicitly the terms on the right hand side and denoting it with $\mathbf{r}$, gathering the terms with the same unknown together with defining $s(\mathbf{u},\mathbf{v}) = (\mathbf{u},\mathbf{v}) + n(\nu,\mathbf{u},\mathbf{v})$, and rewriting (4.2.5) yields to the formulation (4.2.6)–(4.2.7) for given ν, θ and Δt, which gives an idea about how the algebraic system of equations can be resembled on the matrix level after the discretization of (4.2.5) is realized. Since the solution $\mathbf{u}$ does not necessarily to be divergence free, g appears on the right side of the incompressibility condition; however, we will explicitly impose this constraint on $\mathbf{u}$ while seeking for an approximated solution for the pair $\{\mathbf{u},p\} \in H := \mathbf{H}^1_0(\Omega)\times L := \mathrm{L}^2_0(\Omega)$, where $\mathbf{H}^1_0(\Omega)\,\mathrm{L}^2_0(\Omega)$ are the usual Lebesgue and Sobolev spaces. Each term on the left hand side leads to a block matrix with the finite element approximation of the unknowns and test functions.

$$s(\mathbf{u},\mathbf{v}) - \theta\Delta t\, b(p,\mathbf{v}) = \mathbf{r} \qquad \forall\,\mathbf{v}\in H \quad (4.2.6)$$

$$b(q,\mathbf{u}) = g \qquad \forall\, q\in L. \quad (4.2.7)$$

Then, the domain must be decomposed, the approximate solution u_h has to be defined, and the test functions should be chosen from a suitable finite dimensional space.

The approximation of the problem can be obtained with the finite element spaces $H_h \subset H$ and $L_H \subset L$ which are spanned by piecewise polynomials with respect to a regular subdivision or triangulation $\mathbf{T}_h = \bigcup\{T\}$ of the domain Ω into simple cells T (triangles, quadrilaterals, etc. in $\mathbb{R}^2$ and tetrahedarals, hexahedrals in $\mathbb{R}^3$); the subscript h is a measure of the cell-size, e.g., diameter, width. Now, we need the choose an appropriate pair of finite element spaces for the pair $\{\mathbf{u},p\}$ representing the velocity and the pressure in a bounded region $\Omega\subset\mathbb{R}^d$ ($d\in\{2,3\}$) with sufficiently regular boundary $\partial\Omega$. There are numerous discrete spaces H_h and L_h which are proposed in the literature satisfying the stability estimate and the approximability property; however, not all leads to linear system of equations which can be efficiently solved [137].

Pairs of stokes elements, e.g., nonconforming linear or rotated multilinear for the approximated velocity solution and piecewise-constant pressure functions, can implicitly satisfy Babuška-Brezzi condition (stability estimate). Moreover, certain higher order elements, e.g, Q_2/P_1, P_2/P_1 (Taylor-Hood) element, can directly satisfy the stability estimate. All rigorous studies on the derivation of stable finite element pairs agree on one major result that the approximate velocity space H_h should have at least one higher degree than the pressure space L_h has [137].

The rotated bi/trilinear shape functions for the velocity and piecewise constants for pressure ($\tilde{Q}_1/Q_0$) which may be considered as the natural analog of the well-known Crouzeix-Raviart element is presented by Rannacher and Turek [140]. Rannacher-Turek element has shown that *(i)* sat-

isfying the stability condition without any additional stabilization being independent of the geometrical decomposition, in addition it can be supported with the upwind and streamline-diffusion stabilization schemes for higher Reynolds number flows; *(ii)* having comparable accuracy with other first order elements (Q_1/Q_0, Q_1/Q_1, P_1/P_1) yet being the only *unconditionally stable* one; *(iii)* leading to an "optimal" solution schemes with the *local* and the *global Multilevel Pressure Schur Complement solvers*, particularly for the transient simulation of unsteady flow problems.

In the solution of the Navier-Stokes equation, the velocity solution has been approximated with the rotated trilinear polynomial trial functions $\tilde{Q}_1$ which is defined as

$$\tilde{Q}_1(T) := \{q \circ \psi_T^{-1} | \ \in \langle 1, x, y, z, x^2 - y^2, x^2 - z^2, \rangle\}$$

with the corresponding multilinear 1-1-transformation $\psi_T : \hat{T} \to T$ holding for each $T \in \mathbf{T}_h$ where $\hat{T} = [-1,1]^3$ denoting the reference element. Depending on the choice, having either the mean values (^{a})or point-wise values (^{b}) on the faces, the degrees of freedom are determined with either following nodal functionals,

$$F_\Gamma^{(a)}(v) := |\Gamma|^{-1} \oiint_\Gamma v d\gamma \quad \text{or} \quad F_\Gamma^{(b)}(v) := v(m_\Gamma)$$

where $\Gamma \subset \partial \mathbf{T}_h$ which stands for all boundary faces Γ of the elements T; moreover, considering the accuracy purposes one can employ the non-parametric counterparts on the cost of increasing computational effort in case of triangulations with highly distorted and stretched cells.

The pressure shape functions are chosen from the finite element space of piecewise constant polynomial functions Q_0 such that

$$L_h = \{q_H \in \mathrm{L}_0^2(\Omega) \mid q_{h|T} = \text{const.}, \forall T \in \mathbf{T}_h\}$$

Consequently, the approximate solutions $\mathbf{u}_h \in \tilde{Q}_1$ and $\mathbf{p}_h \in Q_0$ can be given as

$$\mathbf{u}_h(\mathbf{x},t) = \sum_j \mathbf{u}_j(t)\varphi_j(\mathbf{x}), \quad \text{and} \quad p_h(\mathbf{x},t) = \sum_k p_k(t)\psi_k(\mathbf{x})$$

where φ_j basis functions span $\tilde{Q}_1$ finite element space. Then, following the conventional Galerkin method the test functions Ψ_i are chosen from the same space; which yields to the equal number of unknowns and equations; nevertheless, this is not the only option, e.g., for convection-dominated transport problems Petrov-Galerkin methods offer certain advantages [39].

Now, we are ready to present the discrete operators which arise when the finite element spatial discretization is applied to (4.2.3). First, let us write the semi-discrete problem according to (4.2.3) within Galerkin finite element approach for the nodal value $\mathbf{u}_i$,

$$\sum_j \left[\int_\Omega \varphi_i \varphi_j \, d\mathbf{x}\right] \frac{d\mathbf{u}_j}{dt} + \sum_j \left[\int_\Omega \nabla\varphi_i \cdot \left(\nu_{\text{eff}}[\nabla\varphi_j + (\nabla\varphi_j)^T]\right) d\mathbf{x}\right] \mathbf{u}_j + \sum_j \left[\int_\Omega \varphi_i (\mathbf{u}_j \cdot \nabla\varphi_j) \, d\mathbf{x}\right] \mathbf{u}_j + \sum_k \left[\int_\Omega \Psi_k \nabla\varphi_i \, d\mathbf{x}\right] p_k = \int_\Omega \varphi_i \mathbf{f} d\mathbf{x} - \int_{\partial\Omega_N} \varphi_i h \, dS \quad (4.2.8)$$

The first three terms on the left hand side yield to , so-called, the system matrix S; and the last term will result in the discrete gradient operator B, transpose of which is the discrete divergence operator B^T. The system matrix has 2 components: the mass matrix $M = m_{ij}$ and discrete transport operator

$K = k_{ij}$; the discrete transport operator involves discrete convective c_{ij} and diffusive operators d_{ij}.

$$\begin{aligned} M_C =(m_{ij}) = &\int_\Omega \varphi_i \varphi_j \, d\mathbf{x} \\ K =(k_{ij}) = &-(n_{ij}) - (d_{ij}) \\ \text{where} \quad n_{ij} = &\int_\Omega \varphi_i (\mathbf{u}_j \cdot \nabla \varphi_j) \, d\mathbf{x} \\ \text{and} \quad d_{ij} = &\int_\Omega \nabla \varphi_i \cdot \left(\nu_{\text{eff}} [\nabla \varphi_j + (\nabla \varphi_j)^T] \right) d\mathbf{x} \end{aligned}$$

The discrete gradient operator B and the discrete divergence operator B^T can be given within mixed finite element formulation as

$$B = \int_\Omega \Psi_k \nabla \varphi_i \, d\mathbf{x} \quad \text{and} \quad B^T = \int_\Omega \nabla \varphi_j \Psi_k \, d\mathbf{x} \tag{4.2.9}$$

By using the defined discrete operators we can write the discrete counterpart of (4.2.5), i.e. the fully-discretized momentum equation.

$$[M + \theta \Delta t K(\mathbf{u})] \, \mathbf{u} + \theta \Delta t B p = [M + \Delta t (1-\theta) K(\mathbf{u}^n)] \, \mathbf{u}^n + \Delta t (1-\theta)(B p^n + \mathbf{f}^n) + \mathbf{f}(\mathbf{u}) \tag{4.2.10}$$

The incompressibility constraint can be analogously written to (4.2.10),

$$B^T \mathbf{u} = 0 \tag{4.2.11}$$

Then, the problem which is formulated with (4.2.6)–(4.2.7) can be given on the matrix level as a coupled nonlinear problem in the form of

$$\begin{bmatrix} S & \theta \Delta t B \\ B^T & 0 \end{bmatrix} \begin{bmatrix} \mathbf{u} \\ p \end{bmatrix} = \begin{bmatrix} \mathbf{f} \\ 0 \end{bmatrix} \tag{4.2.12}$$

where the block matrix S is the so-called system matrix which consists of the mass matrix and the discrete transport operator, $S = [M + \theta \Delta t K(\mathbf{u})]$. The system matrix S has an analogous structure for all conventional unsteady transport-problems; and that is what we also need for numerical solutions of turbulence equations (4.1.5)–(4.1.6) and coupled CFD-PBE (4.1.9).

In case of the coupled equations of $k - \varepsilon$ turbulence model, the finite element approximation yields to a similar algebraic system of equations with the analogous mass M and transport K matrices. For the discretization of nonlinear scalar transport equations (4.1.5)–(4.1.6) we adopted the Q_1 finite element space within the Galerkin approach; so that, the discrete counterpart of (4.1.5)–(4.1.6) can be respectively given for the unknowns $k = k^{n+1}$ and $\tilde{\varepsilon} = \tilde{\varepsilon}^{n+1}$ as following,

$$[M - \theta \Delta t K(\mathbf{u})] \, k = [M + (1-\theta) \Delta t (K(\mathbf{u}^n))] \, k^n + \mathbf{r}(k) \,, \tag{4.2.13}$$

$$[M - \theta \Delta t K(\mathbf{u})] \, \tilde{\varepsilon} = [M + (1-\theta) \Delta t (K(\mathbf{u}^n))] \, \tilde{\varepsilon}^n + \mathbf{r}(\tilde{\varepsilon}) \,. \tag{4.2.14}$$

Actually, the fluid dynamics coupled PBE will lead to a very similar algebraic system, if the source and sink terms in (4.1.9) are discretized within MC; then, the scalar transport problem in space and the internal coordinate (4.1.9), however, yields to a number of coupled nonlinear algebraic systems which is as many as the number of classes and can be given in the following form for the i'th class;

$$[M - \theta \Delta t K(\mathbf{u})] \, f_i = [M + (1-\theta) \Delta t (K(\mathbf{u}^n))] \, f_i^n + \mathbf{r}(f_j) \,. \tag{4.2.15}$$

And, when the PPDC is employed resulting nonlinear algebraic systems are as large as the double number of parent classes.

As a conclusion, it is, now, clear how to achieve the space- and time-discretization of the equations, as well in the internal coordinate (regarding *Chapter 3*). However, the presented algebraic systems are strongly nonlinear, and the fully discretized Navier-Stokes equations (4.2.12) exhibit a saddle point problem for which the pressure can be considered as the Lagrange multiplier for the incompressibility constraint. Therefore, we should firstly focus on solutions of two different algebraic systems: *(i)* a saddle point problem being described with (4.2.12) *(ii)* multiple nonlinear algebraic systems of the generic form $\mathcal{S}(x^{(l)})x^{(l)} = r(x^{(l)})$ arising due to any of the equations (4.2.13)–(4.2.15); with regarding the internal and external couplings in the respected mathematical model, see Figure 2.1.

4.2.3. Solution of the discretized equations

When the complete system of equations is considered, as it is shown in Figure 2.1, the three "separate" systems of equations (the Navier-Stokes equations, the turbulence model and the multiphase model) are linked to each other with external couplings which are evident even at the level of continuous equations, whereas the internal couplings should be considered depending on the chosen numerical approach to solve the obtained discrete systems of equations, e.g., the velocity-pressure coupling (*C2*) in N-S can be handled in many different ways.

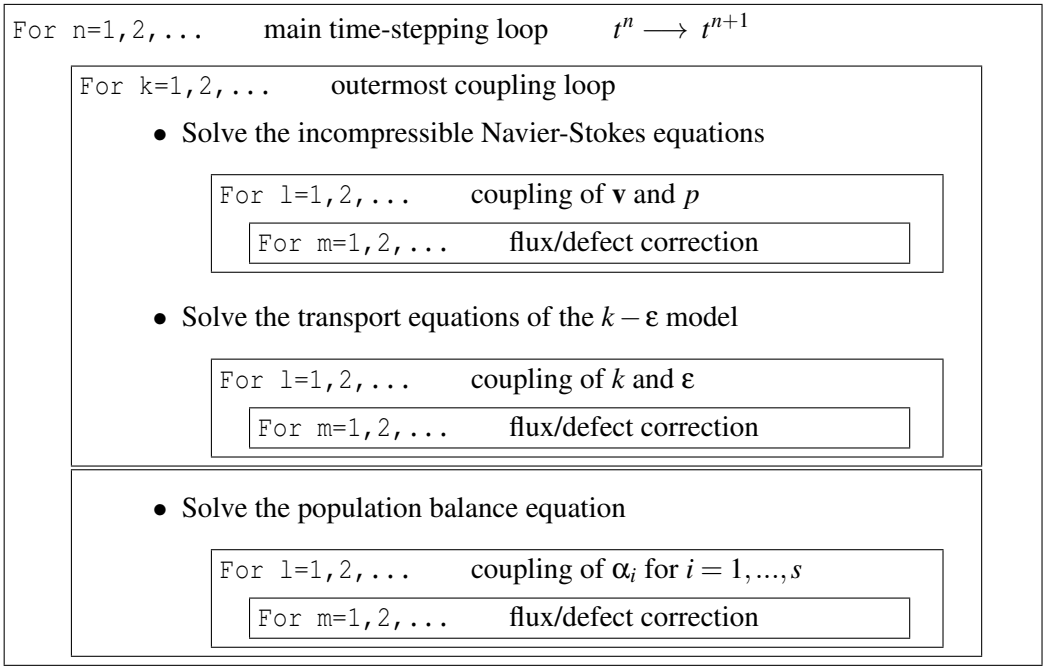

Figure 4.1: Developed computational algorithm consisting of nested iteration loops.

The existing external couplings in the adopted one-way coupled CFD-PBE approach leads to a nested iteration strategy, see Figure 4.1, which needs to be elaborated after specifying the solution methodologies for each part of the coupled model. In order to solve the complete model, first the discrete Navier-Stokes equations should be solved; followed by solving the turbulence model; however, since *C5* coupling is strong, the equations need to be solved in an outer-loop; and when a converged solution is obtained; the decoupled PBE needs to be solved by using the obtained

solutions for the velocity, the turbulent dissipation rate and the turbulent eddy viscosity. The adopted one-way coupled CFD-PBE approach also offers the advantage of solving the coupled CFD-PBE on a given quasi-stationary turbulent flow field.

Navier-Stokes equations

The discretized Navier-Stokes equations exhibit a saddle point problem; zeros exist on the diagonal of the matrix in (4.2.12) due to the incompressibility constraint. The matrices are indefinite and, often, with poor spectral properties; thus, the solution of this sort of algebraic systems requires special care.

The solution algorithm for generalized saddle point problems emerges in two broad categories: *(i)* coupled methods, *(ii)* and segregated methods. Coupled methods consider the saddle point system (4.2.12) as a whole and compute the unknowns simultaneously; all unknowns are treated implicitly without approximating any. Either direct solvers or iterative solvers can be employed within these methods. The direct solvers are based on triangular factorization of the global matrix $\mathcal{A}$ (the matrix on the left hand side of (4.2.12)), and the iterative solvers are usually chosen from the Krylov subspace methods, which all are applied to the whole system; commonly with an appropriate preconditioning. Segregated methods compute the two unknowns separately but in order; in some methods the first unknown is the first to be solved, later the second; and others do it in the other-way around. These methods involve the solution of the reduced linear systems, which involves only one of the unknowns, so the reduced system is smaller in size than the coupled system. The each reduced system can be solved by using direct or iterative solvers; the two most typical segregated methods are the *null space* method and *Schur Complement* method which is based on a block LU factorization of $\mathcal{A}$. The reader is referred to the study of Liesen et al. [141]; they comprehensively present the numerical solution of saddle point problems in their rather lengthy paper.

Turek throughly discusses the solution of the saddle point system (4.2.12) arising as an attempt to numerical solutions of Navier-Stokes equations in his book [137]. It can be deduced from his book that the segregated Navier-Stokes solvers which are constructed based on projection schemes are suitable to be employed for the simulation of two-/multi-phase flows which has to be studied on rather small time intervals; thus, in the numerical solution of Navier-Stokes equations maximum allowable time step sizes are naturally restricted.

The solution of equation (4.2.12) in a segregated fashion is based on the notion that the momentum equation is decoupled from the incompressibility constraint within the Schur complement method, which yields to the general *Pressure Schur Complement* approach by assuming that the operator S^{-1} exists. And the corresponding (linear) pressure Schur complement equation reads

$$B^T S^{-1} B p = \frac{1}{k} B^T S^{-1} \mathbf{f}; \tag{4.2.16}$$

and the corresponding velocity vector is given as $\mathbf{u} = S^{-1}(\mathbf{g} - kBp)$ for a known pressure p. The pressure complement equation can be solved by employing the preconditioned Richardson iteration [142].

$$p^{(l+1)} = p^{(l)} + \left[B^T S^{-1} B\right]^{-1} \Delta t^{-1} B^T S^{-1} (\mathbf{f} - \Delta t\, p^l) \tag{4.2.17}$$

However, from the computational aspect there still remains a challenge: to obtain the Schur complement matrix $C := B^T S^{-1} B$, which is not very likely because S is a full matrix and usually (computationally) not possible to be explicitly inverted.

The matrix S can be assumed, consistent with the previous definition in (4.2.12), to have the following form

$$S := \alpha M + \theta \Delta t K \tag{4.2.18}$$

where the coefficients α and k are spatial and temporal discretization related. Here, it is clear that S can be approximated with the mass matrix as the time step size decrease, $\Delta t \to 0$, which suits very well to our purposes since the nature of problems in our focus is very restrictive on the allowable maximum step sizes and characterized with high Re. Then, the mass matrix M can be substituted with its approximation M_L, the lumped mass matrix, which is a diagonal matrix assembled with the corresponding row-sums of M, or directly with an appropriate cubature formula for the numerical integration in the assembly of M. And, when (4.2.17) is rewritten within the discrete projection method, with $C := P = B^T M_L^{-1} B$ it yields to the following iterative scheme in Figure 4.2, where the matrix $P = B^T M_L^{-1} B$ can be considered as a discrete operator originating from the mixed finite element formulation of the continuous Poisson problem. Now, the problem is reduced to solving the linear equations in *Step 1* and *Step 2* where the Burgers' equation and the discrete pressure Poisson equation have to be solved.

1. Solve the Burgers equation for the velocity $\tilde{\mathbf{u}}$

$$S\tilde{\mathbf{u}} = \mathbf{f} - \Delta t B p^{(l)}$$

2. Compute the update q for the pressure from the 'Pressure-Poison' problem

$$Pq = \Delta t^{-1} B^T \tilde{\mathbf{u}}$$

3. Update the pressure p and project the intermediate velocity $\tilde{\mathbf{u}}$ to a divergence free space

$$p^{(l+1)} = p^{(l)} + q, \quad \mathbf{u}^{(l+1)} = \tilde{\mathbf{u}} - \Delta t M_L^{-1} B q$$

Figure 4.2: Conventional Projection methods

Solutions of the Burgers' equation require the solution of non-symmetric linear system which can be achieved by employing BiCGSTAB from Krylov subspace methods and/or by geometric multigrid methods. And, it is also well known that the geometric multigrid method is one of the most, if not the most, efficient methods for the solution of discrete pressure Poisson problem. For the chosen pair of elements it was shown that it is possible to construct an "optimal" flow solver with the geometric multigrid solvers [137]. Therefore, for the solution of linear problems we employ a multigrid solver of which one sweep to solve the linear problem $A_k u_k = f_k$ can be interpreted as

1. Perform m presmoothing steps to obtain a more accurate iterate for the initial guess u_k at level k

$$u_k^j = \mathcal{S}_k u_k^{j-1} \qquad \text{for} \quad j = 1, ..., m$$

where $\mathcal{S}_k$ is the smoothing operator.

2. Sufficient presmoothing steps yield to a solution which involves high frequency errors when it is restricted onto a coarser grid. Then, the residual on the k'th level is restricted

$$r_{k-1} = \tau_k^{k-1} \left(f_k - A_k u_k^m \right)$$

where τ_k^{k-1} is the restriction operator.

3. Compute the update term for the solution at the coarse grid level
$$A_{k-1}u^*_{k-1} = r_{k-1}$$

4. Interpolate calculated corrections to the fine grid and update the intermediate solution
$$u^{m+1}_k = u^k_m + \alpha_k \tau^k_{k-1} u^*_{k-1}$$
where α_k is a damping parameter and τ^k_{k-1} is the prolongation operator from level $k-1$ to level k.

5. Perform n postsmoothing steps to get the final solution u^{m+1+n}_k.
$$u^{j+1}_k = \mathcal{S}_k(u^j_k)$$

This multigrid sweep can be applied on successively refined/coarsened meshes such that distinct multigrid cycles e.g., V-cycle, W-cycle or F-cycle, having significantly different performance are obtained (regarding the computational cost and the linear convergence); the multigrid cycles are successively applied to ensure a converged solution with respect to a predefined tolerance.

Multigrid sweeps have four main components: the smoother, the restriction and prolongation (interpolation) operators, and the coarse grid solver; from those the most computationally demanding is the smoother. The smoothing-step is based on the iterative solvers, e.g., Jacobi, SOR, SSOR, and consists of several iterations of the chosen method; the incomplete LU factorization (ILU) also stands as an excellent candidate for the smoother; nevertheless, they can be unnecessarily expensive for the regular grids [138]. The prolongation and restriction operators are mostly built in two ways, either as a interpolation or discrete L^2-projection operators; and we have preferred the later for accuracy purposes on non-equidistant grids. The last component is the coarse grid solver which can be adopted as one of the mentioned iterative or the Krylov subspace methods, e.g., conjugate gradient (CG), biconjugate gradient (BiCG), biconjugate gradient stabilized (BiCGSTAB), depending on the symmetry of the linear system in the scope. Moreover, with up-to-date computers even the direct solvers can be employed to construct efficient multigrid solvers for fairly-fine coarse-grids (approx. 20,000 unknowns).

The efficiency/optimization of the multigrid solver has always been an interesting topic. The multigrid solver has many (in)dependent components which have several problem-dependent parameters to be set, e.g., number of pre-/post-smoothing steps, number of grid levels to be swept, type of multigrid cycle, the adopted solvers/smoothers and their own parameters. One rule of thumb can be postulated as the residual error does not need to be reduced by a great factor in the coarse-grid solver step, one digit gain usually suffices. There are many studies on the optimization of the multigrid solvers but the following study [142] stands out regarding how an efficient flow solver can be constructed within the Multilevel Pressure Schur Complement approach based on optimized multigrid solvers, which clearly states that the challenge is far larger than to only develop an optimal multigrid solver but to build an efficient rigorous approach for the accurate solution of Navier-Stokes equations.

Even the most-accurate flow solvers may fail to converge in the solution of flow problems when special care is not taken for the discrete convective operator. Depending on the high local Re (Re_h) and the mesh size, there may exist unresolved subgrid effects which sooner or later cause the numerical solution to prescribe unphysical flow field. The underlying fact in numerics is that with the chosen finite element discretization the obtained "central" discretization is, in principle, 2nd order accurate unless the local mesh size is larger than a certain mesh size, which is very restrictive and makes it impossible to obtain accurate results without special treatment of the convection term.

As a remedy, artificial diffusion is added to cancel out the dominating convective terms, which is not very straightforward and can be accomplished in many different ways.

A common way to introduce the "required" numerical diffusion is to follow the upwind strategies which are employed for different discretization methods, e.g., FVM, element based FVM, FDM, FEM. The implementation of the method varies but the idea remains the same: new lumping regions and lumping operators which are edge oriented should be incorporated. An upwind discretization for the employed $\tilde{Q}_1$ finite element is described in detail based on the works by Ohmori and Ushijima [143], and Tobiska and Schieweck [144]. This stabilization scheme is employed through this study. Nevertheless, this was not the only option and the so-called stream-line diffusion, namely the streamline upwind Petrov-Galerkin (SUPG) method in finite element method context, can be employed; it is a classical Petrov-Galerkin method and designed to mainly add diffusion in the streamline/flow direction. The method is based on the idea that is to locally modify test functions $\mathbf{v}_{PG} := \mathbf{v} + \delta\mathbf{u}\ cdot\nabla\mathbf{v}$, where δ varies with Re_h and h so that the accurate amount of artificial diffusion is added [145]. Moreover, the standard Galerkin method which is a centered scheme can be expected to remain still 2nd order accurate after it is modified with stabilization schemes [137]. Yet, these stabilized high-order schemes may lead to undershoots and overshoots in the region of steep gradients. These can deteriorate the solution and lead to unacceptable results in certain cases, such as, where the positivity of the unknowns is a must. Then, algebraic flux correction schemes can be employed, which are discussed in the next subsection while the solution of turbulence equations is in the scope.

The so-far discussed methods can be readily employed to solve linearized Navier-Stokes equations, namely Oseen equations, but we need another mathematical component to deal with the nonstationary Navier-Stokes equations which are nonlinear due to the convective term (C2 coupling). The nonlinear model problem $A(u)u = f$ can be solved efficiently within a defect correction loop. The unknown u can be expressed in the basic nonlinear iteration as

$$u_j = u_{j-1} + \omega C^{-1} r_{j-1}, \qquad j = 0, 1, 2, \ldots ;$$

where the defect is given as $r_k = f - A(u_k)u_k$ in k'th iteration, so is the damping factor ω which can be a fixed choice or adaptively determined with respect to a certain algorithm, for further discussion refer to the study [137]. In this iteration the choice of C is very crucial, depending on the choice one can obtain the standard Newton's method or fixed point defect correction schemes. The construction of the Newton matrix in each iteration is very costly, to obtain the exact derivative on discrete level is not the most affordable, and it is not very likely to obtain optimal solvers with the derivatives being calculated on the continuous level; therefore, we rule out this option despite the fact that quadratic convergence of Newton's method is very promising in terms of required number of iterations. And, we go for fixed point defect correction methods with a constant ω for which one can choose $C = A$ leading to the standard fixed point approach. Then, one iteration of the defect correction loop can be presented as in Figure 4.3. The unknown u_j is iterated within this loop until a converged solution with respect to a predefined criterion is obtained.

The nonlinear convective term is hereby linearized with the approximation $(u_j \cdot \nabla)u_j \approx (u_{j-1} \cdot \nabla)u_j$; however, this is not the only option but also backwards extrapolation in time can be used to linearize the convective term, e.g., $(u^n \cdot \nabla)u_j, \quad ((2u^n - u^{n-1}) \cdot \nabla)u_j$. These linearized convection terms are, indeed, computationally-favorable due to the reduced cost with the removed nonlinearity. Unless problems are strongly nonlinear, they can be safely employed. The problem in our scope is highly nonlinear; thus, even though the linearized convection terms by backwards extrapolating in time are advantageous in terms of computational performance, they can not be employed for our purposes.

1. Calculate the residual for the given u_{j-1}

$$r_{j-1} = f - A(u_{j-1})u_{j-1}$$

2. Solve an auxiliary problem for the update term z_{j-1}

$$A(u_{j-1})z_{j-1} = r_{j-1}$$

3. Obtain u_j by updating u_{j-1} with relaxing z_{j-1}

$$u_j = u_{j-1} + \omega z_{j-1}$$

Figure 4.3: Defect correction iteration.

As a summary, the numerical solution of discretized (both in time and space) Navier-Stokes equations have been discussed. The resulting algebraic system is of saddle point type and a Schur Complement method has been suggested for the solution, *Pressure Schur Complement Approach*. Solutions of the decoupled linearized algebraic equations have been considered in the framework of geometric multigrid methods of which components have been explained in detail, especially smoothers and coarse grid solvers. Linearization and stabilization of the nonlinear convection term have been introduced with the efficient solution of nonlinear equations in a fixed-point scheme. So that, we analyzed the solution of coupled problems of saddle-point type, the solution of nonlinear equations and the solution of linear equations, which are pretty much what is required while solving any transport problem.

The $k-\varepsilon$ transport equations

The $k-\varepsilon$ transport equations (4.1.5)–(4.1.6) are highly nonlinear, strong couplings arise due to the variables, e.g. ν_T, and the model coefficients γ, β and f_2. There are not many studies presenting all the details considering the numerical solution of these equations but studies by Kuzmin [34, 146, 147]. The main challenges are to efficiently solve computationally highly demanding coupled nonlinear problems, design of accurate "non-diffusive" stabilization schemes for convection dominated problems which avoids under- and over-shoots, and the positivity preserving linearization. The first difficulty has been discussed in detail in the previous section, and a fixed-point scheme is suggested for the numerical solution of non-linear equations which also allow us to treat the coupled equations in the same defect correction loop. Thus, we will stress the last two points of which the former has been partially discussed in the framework of numerical solution of the discretized Navier-Stokes equations.

As it has been mentioned in the previous section, the numerical treatment of convection is very difficult, especially for highly convection dominated problems. While the low-order methods introduce excessive artificial diffusion which causes to lose of accuracy, stabilized high-order schemes produce undesired overshoots and undershoots which can not be tolerated depending on the nature of the problem, even the stabilized high-order schemes can fail to provide accurate acceptable results in the vicinity of steep gradients. Therefore, we need a scheme which combines the advantages of high-order and low-order schemes so that excessive addition of numerical

diffusion and the formation of wiggles can be avoided.

Boris and Book are the first who presented a stabilization scheme which adaptively alternates between the high- and low-order methods, Flux-corrected-transport (FCT) [148]. Later, at the end of 1970s, their algorithm is generalized by Zalesak so that it can be employed with unstructured grids; nonetheless, Löhner et al. has published the first study on FCT for unstructured grids [149]. Total variation diminishing (TVD) schemes are introduced with a rigorous mathematical formulation as a robust high-resolution method by Harten; however, its application/implementation in finite element context had been unwieldy and the applications could be realized with only P_1/Q_1 continuous elements which provides the preeminent three-point stencil [146]. Then, an algebraic approach, Algebraic Flux Correction (AFC), which combines the advantages of both FCT and TVD is presented by Kuzmin et al., who also explains the underlying concepts of the AFC scheme within several publications citeKuzmin2004a, Kuzmin2004b, Kuzmin2006b.

In order to present a brief description of the employed AFC scheme, we firstly introduce principles of a low-order scheme. Let's recall the discrete transport operator $K = (k_{ij})$ and the lumped mass matrix $M_L = (m_i)$ and consider an unsteady convection problem, $M_L \frac{du}{dt} = Ku$ which can be rewritten as

$$m_i \frac{du_i}{dt} = \sum_{i \neq j} k_{ij}(u_j - u_i) + r_i u_i, \quad \text{where} \quad r_i = \sum_j k_{ij}.$$

When the entries of K are nonnegative but the diagonal ones, the scheme is local extremum diminishing (LED) with omitting the term $r_i u_i$ which naturally vanishes for a divergence free velocity field; otherwise, it represents the physical growth of local extrema. The transport operator K can be modified by introducing artificial diffusion; so, we obtain its stabilized and non-oscillatory counterpart $L = K + D$ where

$$d_{ij} = \max\{-k_{ij}, 0, -k_{ji}\} = d_{ji} \quad d_{ii} = -\sum_{k \neq i} d_{ik}\,. \tag{4.2.19}$$

It is obvious that the constructed numerical diffusion operator is conservative: diagonal terms are the sum of the off-diagonal terms with an opposite sign, and it can be considered as the coefficients of the inter-nodal fluxes.

It is preferred to work with fluxes to recapture the high-order scheme, and as a straightforward idea: one completely subtracts the contribution of the modification term on the flux-level and ends up with the initial high-order scheme. Then, one can define the numerical diffusive flux and can adaptively remove the contribution of the artificial diffusion by introducing a local blending factor $0 \leq \varsigma_{ij} \leq 1$, which yields to the low-order (high-order) scheme for the value 0 (1). The idea can be mathematically expressed as

$$m_i \frac{du_i}{dt} = \sum_{j \neq i} l_{ij}(u_j - u_i) + r_i u_i + \sum_{j \neq i} \varsigma_{ij} f_{ij}$$

where $f_{ij} = d_{ij}(u_i - u_j) = -f_{ij}$ is the raw antidiffusive flux which needs to be limited [152]. Consequently, two difficulties remain: defining a prelimited upwind-flux and a clever way to adaptively set ς_{ij} values.

First of all, an orientation convention has to be chosen, for which entries of L for the edge $\vec{e}_{ij}$ are such that $l_{ji} > l_{ij}$. The edge $\vec{e}_{ij}$ is specified between two adjacent nodes i and j of which basis functions have at least one overlapping support; as a result, node i is the upwind one. Later, a prelimited upwind-biased flux can be defined as $f_{ij} := \min\{l_{ji}, d_{ij}\}(u_j - u_i)$, and $f_{ij} := -f_{ji}$ [152].

Nevertheless, the prelimited flux does not ensure that the stabilized discrete convective operator is positivity preserving; hence, the row sum of antidiffusive fluxes are bounded.

The lower/upper bounds are determined such that

$$Q_i^{\pm} = \sum_{j \neq i} q_{ij} \overset{\max}{\min} \{0, u_j - u_i\} \tag{4.2.20}$$

where $q_{ij} := \frac{m_{ij}}{\Delta t} + l_{ij} \geq 0, \forall j \neq i$. Then, these bounds must be applied to the sum of antidiffusive fluxes which can be given by

$$P_i^{\pm} = \sum_{j \neq i} p_{ij} \overset{\min}{\max} \{0, u_j - u_i\} \tag{4.2.21}$$

with $p_{ij} := -\min\{l_{ji}, d_{ij}\} \leq 0$ and $p_{ji} := 0$, so it is ensured that the positivity of the off-diagonal coefficient l_{ji} is not deteriorated and larger time steps are allowed. Accordingly, the blending factor ς_{ij} can be defined as

$$\varsigma_{ij} = \begin{cases} R_i^+ & \text{if } f_{ij} > 0, \\ R_i^- & \text{if } f_{ij} < 0, \end{cases} \qquad \text{where} \quad R_i^{\pm} = \min\{1, Q_i^{\pm}/P_i^{\pm}\}. \tag{4.2.22}$$

which is also used to limit f_{ji}. As a consequence a positivity preserving stabilization scheme with adding as less as possible artificial diffusion can be obtained; nevertheless, this was the first challenge to overcome, and now a positivity preserving linearization must be applied to the nonlinear system.

The above explained high-resolution scheme can be safely employed to solve linear scalar transport problems without undershoots and overshoots; moreover, the scheme satisfies the positivity condition. However, securing the positivity of the (quasi-) linear transport problem's solution is not enough to preserve the positivity of the coupled turbulence equations (4.1.5)–(4.1.6). The equations are strongly non-linear; and due to the sink terms at the right hand sides the positivity of the solutions can be easily deteriorated unless a careful linearization is applied. The positivity of the solution is very important because, obviously, the negative values of k and ε are not physical, and since the exact solution of the k–ε equations remains non-negative for physically valid initial conditions so should the numerical scheme do [153].

The solution of the coupled equations evolves in time within four nested loops (see Figure 4.1), the solution marches in time in the main time-stepping loop, and each time step is solved within the outermost coupling loop where only the unknowns of the subproblems/steps are updated at each iteration, e.g, k and ε at *Step 2*. Hence, the dependent variables, such as γ and β, are treated explicitly; their values are calculated with the solutions of the previous time step. So that, the positivity of coefficients which is even more important than satisfying the positivity condition for the transported quantities is ensured with suitable initial conditions and a positivity preserving scheme [136, 146].

The application of the positivity preserving linearization has already started by writing the modified k–ε equations (4.1.6)–(4.1.5) according to Lew et al. [136] and introducing the linearization parameter γ. In this formulation, the equations can be already considered as linear if one explicitly treats the coefficients and the source terms. The linearization parameter also has a great advantage that the sink terms can be treated implicitly at the left hand side. Moreover, the source terms P_k and $\gamma C_1 f_1 P_k$ are always non-negative according to their definition. Consequently, we obtain two algebraic systems analogous to (4.2.13) and (4.2.14) which need to be solved successively

within an *outer iteration loop* of which index is denoted with l, see Figure 4.1:

$$[M_L - \theta \Delta t K^*(u^{(l)})]u^{(l+1)} = [M_L + (1-\theta)\Delta t K^*(u^{(l)})]u^{(l)} + q^{(k)} \tag{4.2.23}$$

K^* is the stabilization applied discrete transport operator and $q^{(k)}$ stands for the source term which are updated at every outermost iteration due to coupling with the Navier-Stokes equations. At each outer iteration, a linear problem is solved for a given u^l within a defect correction loop where also the flux correction is applied; all these intertwined steps can be clearly shown in Figure 4.1.

Hereby, we have discussed two more very crucial numerical ingredients in our solution methodology: a high-resolution scheme for the discretization of the convective terms which does not cause wiggles at the vicinity of steep gradients, and positivity-preserving linearization which is preeminent for the solution of nonlinear transport problems which do not admit negative solutions; these are also essential components which are required for the numerical solution of the coupled PBE-CFD problem (4.2.15). Additionally, the iterative solution algorithm which is realized within a nested-loop strategy has been discussed in detail.

Coupled PBE–CFD equations

The equation describing coupled PBE-CFD problems (4.1.9), from our aspect, can be considered as a convection-diffusion reaction (CDR) equation, which inherits all challenges related to this sort of problems additional to the difficulties regarding the PBE. The challenges in numerical solutions of a CDR equation have been inclusively discussed above, in the context of Navier-Stokes equations and the turbulence model. From our point of view, equation (4.1.9) describes the transport of an active scalar for a given flow field; nevertheless, the calculation of the reaction term is not trivial and can be realized with MC or PPDC.

The inherited difficulties can be recalled such as, the stabilization of the convective term with a bounded scheme since the nature of the problem do not admit overshoots and undershoots; and due to the fact that the transported quantities are "non-diffusive" but the turbulent eddy viscosity is responsible for the diffusion of the transported quantities, the stabilization scheme can be easily over-diffusive. The resulting algebraic systems is huge and highly nonlinear; moreover, the problem admits only non-negative solutions, which enforces the use of positivity-preserving linearization/schemes. Fortunately, these are already matched challenges which we have successfully overcome.

The reaction term is highly nonlinear and this leads to strongly coupled nonlinear algebraic systems when MC is employed. The nonlinearity/strong-coupling can be handled in an outer loop as it has been done for the turbulence model. However this time the number of equations need to be considered is much more than the two-equation turbulence models. When MC is applied to equation (4.1.9), it yields to the following semi-discrete form (the equations are discretized in the internal coordinate yet not in the external coordinate and time)

$$\begin{aligned}\frac{\partial f_i}{\partial t} + \mathbf{u}\cdot\nabla f_i - \nabla\cdot(\nu_T \nabla f_i) = \sum_{j=i}^{n} r^B_{i,j} f_j \Delta\upsilon_j - \frac{f_i}{\upsilon_i}\sum_{j=1}^{i}\upsilon_j r^B_{j,i}\Delta\upsilon_j \\ + \frac{1}{2}\sum_{j=1}^{i} r^C_{j,k} f_j f_k \Delta\upsilon_j - f_i \sum_{j=1}^{n} r^C_{j,i} f_j \Delta\upsilon_j \qquad \text{for} \quad i = 1,2,...n. \end{aligned} \tag{4.2.24}$$

Now, we see that while in the continuous formulation there has been only one nonlinear equation to solve, in its discrete form we have $n+1$ (number of classes and the total holdup of the classes)

coupled transport equations to solve, and this number is usually about 50 as we have found when the convergence analysis with respect to number of classes has been studied in *Section 3.4*. And now, we are left with numerous equations of the form (4.2.15) which have to be solved by employing efficient (non)linear solvers and positivity-preserving high-resolution schemes. The required numerical methods and techniques have been already developed for the solution of the turbulence model; then, they should be applied in the frame work of PBE.

Let us recall that we have chosen the MC with the fixed-pivot technique which enabled us to express the coupled CFD-PBE (4.1.9) and its discrete counterpart (4.2.15) in terms of the holdup values according to (3.1.5). So, the actual equation being solved is given in the semi-discrete form as

$$\frac{\partial \alpha_i}{\partial t} + \mathbf{u}\cdot\nabla\alpha_i - \nabla\cdot(\nu_T\nabla\alpha_i) = \sum_{j=i}^{n} r^B_{i,j}\alpha_j\Delta\upsilon_j - \frac{\alpha_i}{\upsilon_i}\sum_{j=1}^{i}\upsilon_j r^B_{j,i}\Delta\upsilon_j + \frac{1}{2}\sum_{j=1}^{i} r^C_{j,k}\alpha_j\alpha_k\Delta\upsilon_j - \alpha_i\sum_{j=1}^{n} r^C_{j,i}\alpha_j\Delta\upsilon_j \qquad \text{for} \quad i=1,2,...n. \tag{4.2.25}$$

Additionally, there the transport equation of the total holdup of classes is

$$\frac{\partial \alpha}{\partial t} + \mathbf{u}\cdot\nabla\alpha - \nabla\cdot(\nu_T\nabla\alpha) = 0 \tag{4.2.26}$$

The obtained FEM discretization with Q_1 conforming trilinear elements admits the explained high-resolution scheme, Algebraic Flux Correction (AFC). The considerable cost of employing AFC is due to the arising "numerical nonlinearity", even a linear problem needs to be treated in a nonlinear fashion; nevertheless, our problem is highly nonlinear in nature, and AFC turned out to be an efficient scheme as accurate as it is. Since employed AFC was not enough to ensure the positivity-condition, the above-explained (*Subsection 4.2.3*) positivity preserving linearization was employed as well. In order to linearize the equation (4.2.3), the source term and the sink term were treated explicitly and implicitly, respectively. The source term were calculated with the known values from the previous iteration (outer-iteration loop due to *C4* internal coupling which is caused by the dependency of classes' holdup on each other, see Figure 2.1); the sink terms are treated "implicitly" at the left hand side and thus modifies the system matrix. The "implicit" treatment (perhaps semi-implicit is more suitable than implicit), is obtained by considering α_i as unknown and the remaining part of the term is calculated for the given values of α_j from the previous outer-iteration as coefficients and are added to the system/global matrix A of the linearized equation (4.2.28). Later, the source and sink terms are updated at each outer-iteration. Then, by accordingly reformulating equation (4.2.27) the following algebraic system is obtained:

$$\left(M_L + \left(\theta K - B_i^- - C_i^-\right)\Delta t\right)\alpha^{(n+1)}_{i,(l+1)} = \left(M_L - (1-\theta)K\Delta t\right)\alpha^{(n+1)}_{i,0} + (B_i^+ + C_i^+)\Delta t\,\alpha^{(n+1)}_{i,(l)} \qquad \text{where} \quad \alpha^{(n+1)}_{i,0} = \alpha^n_i \quad \text{for} \quad i=1,2,...n, \tag{4.2.27}$$

Equation (4.2.27) (see Figure 4.1 for the indices) can be efficiently solved within a defect correction loop which is also very convenient for the application of flux-correction according to the employed AFC scheme, which yields to the algebraic system of the form

$$\begin{aligned} &A(\mathbf{u}^{(n)}, \nu_T^{(n)}, B_i^{\pm(l)}, C_i^{\pm(l)})\Delta\alpha_i^{(m+1)} = r^{(m)}, \\ &\alpha_i^{(m+1)} = \alpha_i^{(m)} + \omega\Delta\alpha_i^{(m+1)}, \end{aligned} \tag{4.2.28}$$

$r^{(m)}$ denotes the defect vector and the super-/sub-scripts refer to the loop in which the corresponding variable is updated, see Figure 4.1.

The solution of (4.2.26) is relatively straightforward as it describes a convection dominated transport problem of a passive scalar. The resulting algebraic system is in the form of equation (4.2.27) but with the *zero source and sink terms*, which is solved with a fixed-point defect correction method, that resulted in the same formulation with (4.2.28) for α instead of α_i.

The linear equation system (4.2.28) is, preferably, solved by employing SOR or SSOR schemes which are satisfactory for rather small time step sizes, as we mostly have to choose due to the nature of the problem. However, the condition number of the matrix is deteriorated for larger time steps; then, schemes which involve BiCGSTAB with ILU decomposition and suitable renumbering are satisfactory.

Another possibility is to consider the solution of coupled CFD-PBE problems in the framework of the PPDC method. The PPDC method has already been comprehensively presented and discussed for 0D applications and shown to a be very accurate method, in *Section 3* and *Subsection 3.4*; however, its application in 3D is not straightforward, and the suggested strategy by Bove et al. [9,97] has shown to be not "adequate" [154]. Therefore, first we discuss the suggested strategy by Bove for the convection in 3D; then, we suggest a novel implementation strategy so that an efficient and an accurate hybrid method which is based on MC and MOM is obtained.

The PPDC method is characterized as a "non-standard method of classes" by Bove; nevertheless, since it has much common with QMOM; and particularly the closure of each method is given by a Gaussian quadrature whose weight is the particle number density distribution function, it can be also considered as a moment based method, especially within the suggested approach in this study. When the quadrature approximation is adopted, most methods use the PDA algorithm (Gordon, 1967 [14]) which needs the first $2n$ moments of the distribution function. However, PPDC, QMOM and MC, they all have discrete representations of the particle size distribution with quadrature approximation, which is a common point for all.

Bove has suggested that the spatial transport of the dispersed phase can be described either analogously to DQMOM, or by solving a transport problem for the parent classes by strictly keeping track of transported quantities (number density, volume density, etc.) of each parent class and the class related properties (size, volume, etc.). He clearly pictures his idea with a sketch for 1D-convection in his study [9] but there is no rigorous mathematical description of how it was realized. His idea is to transport the expanded classes so that in each control volume to obtain a size distribution due to transport in space and in the internal coordinate. That, later, can be reduced to initial number of parent classes by using the PDA algorithm, which is the same step performed in 0D to reduce the increased number of quadrature points as a result of coalescence and breakage.

Bove employs an operator splitting approach to decouple PBE from the CFD part. Then, in one half of the time step $\frac{\Delta t}{2}$ PBE are solved and in the other half the parent classes are advected. Solving the decoupled problems for $\frac{\Delta t}{2}$ step size is not clearly reasoned neither we appreciate the application. And, advecting the classes which all have different sizes are also not very convincing. Therefore, we suggest reformulating the transport equation of classes in terms of the first $2n$ order of moments and transporting the moments. Once the moment distribution is updated, the rest is to obtain the quadrature approximation of size distribution for n points, i.e. n parent classes.

First, the transport equation (4.1.9) has to be rewritten in terms of moments according to the equation (3.1.6) which can be more explicitly written as

$$m_k = \int_0^\infty f(L,\mathbf{x},t)L^k \qquad k \in \mathbb{R}$$

where L denotes the diameter of drops, as very common in the literature; however, it may refer to the volume or area, or any *size*-related property; then, $k \in \mathbb{R}$. With this definition the transport equation can be given as,

$$\frac{\partial m_k(L,\mathbf{x},t)}{\partial t} + \mathbf{u}\cdot\nabla m_k(L,\mathbf{x},t) - \nabla\cdot(\nu_T \nabla m_k(L,\mathbf{x},t)) = \int_0^\infty \left\{ \frac{1}{2}\int_0^\upsilon r^C(\tilde{\upsilon},\upsilon-\tilde{\upsilon}) f(\tilde{\upsilon}) f(\upsilon-\tilde{\upsilon})\, d\tilde{\upsilon} - f(\upsilon)\int_0^\infty r^C(\tilde{\upsilon},\upsilon) f(\tilde{\upsilon})\, d\tilde{\upsilon} + \int_\upsilon^\infty r^B(\upsilon,\tilde{\upsilon}) f(\tilde{\upsilon})\, d\tilde{\upsilon} - \frac{f(\upsilon)}{\upsilon}\int_0^\upsilon \tilde{\upsilon} r^B(\tilde{\upsilon},\upsilon)\, d\tilde{\upsilon} \right\} L^k dL \quad (4.2.29)$$

For readability purposes, at the right hand side m_k is given as an explicit function of L whereas at the left hand side $f(v)$ has been used; and v is a one-to-one function of L. So that, (4.2.29) presents our approach: calculate the reaction term explicitly according to the MC (which is already explained for 0D in *Section 3*); and solve the transport problem with obtaining moment values from the calculated source and sink terms. Finally, we obtain the updated moment distribution from which the size distribution with the initial number of parent classes can be obtained according to the PDA. Consequently, the updated distribution is obtained with respect to the transport phenomena and the breakage and coalescence phenomena.

From the numerical point of view, this formulation does not allow the positivity-preserving linearization for which the sink terms have to be treated implicitly with the unknowns on the left hand side. Thus, we have two possibilities: *(i)* explicit treatment of the reaction so to insert the source and sink terms on the right hand side of (4.2.29) *(ii)* an operator splitting approach in which first the transport in the internal coordinate is solved, later is the spatial transport. It is well known that when the time step is chosen sufficiently small such that the positivity constrained is not violated, the first approach is more accurate. Nevertheless, the second approach allows to use different time step sizes for the solution of PBE and the transport problem, which indeed exhibits a great advantage for the cases of the spatial transport, and the breakage and coalescence phenomena occurring in different time scales. We will study the both approaches.

The challenge in the either suggested approaches is to *accurately* transport the moment values. Even if the secondary phase exhibits a smooth field for the lower order moments, there can, very well, be steep changes in the high-order moment field. Let's consider the case for which the distribution of first order moment values is described with a linear function; and the advection of this linear function can be accurately realized without a rigorous numerical treatment. However, when high order functions are advected, the transport problem turns out to be more challenging due to quick changes of values. Moreover, if it is considered that there may exist sharp fronts and jumps in the low order moment distribution, those will be even more prominent in the high order moment distribution, so to accurately solve the transport problem is a true challenge; we, hence, suppose that nobody has had an attempt on this yet.

The discussion can be concluded by presenting the suggested algorithm for the numerical solution of PBE within the frame work of modified PPDC:

1. Calculate the birth events according to PPDC (source term), *Steps 3–4* in Figure 3.5.
2. Calculate the death events due to the birth events (sink term).
3. Calculate the corresponding source and sink terms in terms of moments for the first $2n$ low-order moments $k = 0, 1, .., 2n-1$.

4. Solve the transport problem for the moments:

   (a) if *operator splitting approach*, first add the update terms to the moment fields and solve (4.2.29) with a *zero* right hand side for m_k.

   (b) if *explicit treatment of the reaction term*, solve (4.2.29) with the corresponding update term on the right hand side for m_k.

5. Obtain the new parent classes from the advected moment fields by using PDA, analogously to the *Step 5* in Figure 3.5.

The solution of the obtained/derived equations and the resulting algebraic systems are not further discussed for this new approach because they concern the solution of the (in-)homogeneous convection-diffusion equation regarding the chosen approach (*4a*) *4b*, which has been already discussed for MC; above the discussion on the solution of (4.2.3) or (4.2.26).

4.3. Computational studies for validation

The computational studies in this subsection concern, firstly, the validation of the implemented numerical methods and techniques for the solution of coupled CFD-PBE problems via comparing the accuracy of the obtained results and the robustness of the accordingly developed computational tool.

The first computational study deals with a steady 1D (in space) channel problem which is analogous to an unsteady 0D population balance problem. This problem is studied in both steady and unsteady fashions so to determine the accuracy of the adopted numerical methods: FE spatial discretization, positivity-preserving stabilization scheme and the time discretization techniques.

The oil-in-water dispersed flow is studied in a 3D pipe in an unsteady fashion in order to verify the solution of the flow solver and to obtain a framework for the comparison of MC and PPDC. The available comprehensive CFD results for pipe-flows make this case a suitable validation and verification study. Since there is neither experimental nor numerical reference-results for turbulent dispersed flows (up to the author's knowledge) regarding either flow field or size distribution of the secondary phase; we consider it as very important to firstly study the coupled problem with verified flow-field's results so to avoid the discrepancies which may arise due to the inaccurate CFD results.

Once the simple geometries are studied and the results are found to be satisfactory, the next step is to compare MC and PPDC within an industrial problem regarding the robustness because it is well known that the implementations which involve the moment transport and the PDA are prone to abruptly fail. The complex geometry of SMV™ leads to steep changes of the flow-field variables as, velocity and turbulent energy dissipation rate. The great changes in the flow-field make solving the spatial transport problem very challenging; moreover, since the different ε values result in distinct size distributions, there will be sharp fronts for the moment fields, especially for the high order moments. The comparison will be conclusive for the final decision on choosing the methodology to study the verification cases.

4.3.1. 1D Channel Problem

Analytical solutions of population balance coupled CFD problems are not available; therefore, how to validate an implementation which concerns solutions of CFD-PBE problems is not clear. However, Silva et al. had the idea to study the time dependent 0D PBE as a steady 1D problem by transforming the related equation [40]. This idea inspired us to restudy the transient 0D case from McCoy and Madras [42], which is the simultaneous breakage-coalescence case in *Section 3.4.1*.

The transformation of the equation for a general variable ϕ follows as

$$\frac{d\phi}{dt} = \varphi \quad \Rightarrow \quad u_\xi \frac{d\phi}{d\xi} = \varphi \tag{4.3.1}$$

where ξ is channel's longitudinal direction and the u_ξ is the magnitude of the steady uniform velocity in this direction; this way the time axis is substituted with ξ so to obtain a 1D steady problem which is analogous of a transient 0D problem. Moreover, when the 1D unsteady-convection problem (4.3.2) is solved for the steady-state, the obtained results should be the same with the ones for the steady problem (4.3.1).

$$\frac{d\phi}{dt} + u_\xi \frac{d\phi}{d\xi} = \varphi \tag{4.3.2}$$

The 1D problems have been solved with our implementation for 3D. The solution of the unsteady problem is straightforward with the developed computational tool; one needs to set the viscosity parameter to 0 and the solver will do the job. Nevertheless, for the steady problem the solver strategy has to be altered. The issue is the employed iterative linear solvers tends to diverge or hardly converge (luckily) for convection problems when the initial guess is poor; and, this is exactly what happens when one tries to solve the steady problem with the developed solver strategy for transient problems. Therefore, we suggest the following strategy: first, we assemble all the required discrete operators and the right hand side; then we solved auxiliary problems in order to obtain a better initial guess for the solution. The auxiliary problems were nothing but considering the same problem with an under-relaxed right hand side. Our strategy for the solution of the steady problem can be given as:

1. Build the discrete operator A and r
2. Solve auxiliary problems for the update term z_i until $\omega_i = \omega_n = 1$.

   $$A(\omega_i r_i - A u_{i-1}) = z_i, \quad \text{for } i = 1, 2, ..., n$$

   where $u_i = u_{i-1} + z_i$ and $\omega_i = \omega_{i-1} + \Delta\omega_i$ is an adaptive or a constant under-relaxation parameter, $0 < \Delta\omega \leq \omega_1 \ll 1$; u_0 is the initial guess for the first auxiliary problem $i = 1$.

Figure 4.4: Solver strategy for the steady convection problem.

Let us recall the studied test case and its analytical solution; the numerically simulated phenomenon is simultaneous breakage-coalescence of droplets, and the events are modeled with hypothetical kernels (3.3.1) and (3.3.6). The closures are chosen by McCoy and Madras [42] such simple that they yield to the analytical solution (3.3.9). The provided analytical solution can be

extended to obtain the evolution of moment orders in time [40] as follows:

$$m_k(\tau) = \left[\frac{\varphi(\infty) + \tanh(\varphi(\infty)\tau/2)}{\varphi(\infty)\,(1+\tanh(\varphi(\infty)\tau/2))}\right]^{k-1} \Gamma(k+1) \tag{4.3.3}$$

So that, the initial moments of the dimensionless distribution can be simply written as [40]

$$m_k(0) = \Gamma(k+1) \tag{4.3.4}$$

The computational domain is a square channel with the dimensions $1\,\mathrm{m} \times 0.1\,\mathrm{m} \times 0.1\,\mathrm{m}$. The x-direction is the longitudinal direction which is also the direction of the advection velocity whose magnitude is equal to $0.05\,\mathrm{ms}^{-1}$. The chosen convection velocity provides a steady size distribution in the computational domain; the previous calculations in *Section 3.4* helped us to adjust the length of the channel and the velocity. The computational domain (see Figure 4.5) is meshed 3 times such that the equidistant mesh size h is equal to 0.025 m, 0.00625 m, and 0.001 m. In these computational domains steady and transient simulations are performed to obtain the steady size distribution.

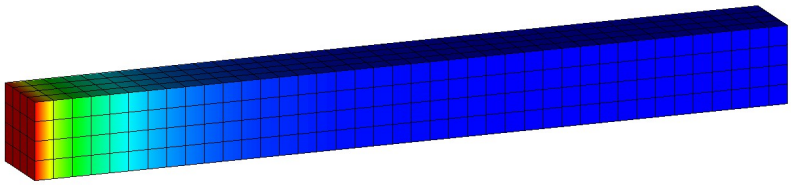

Figure 4.5: The computationally modeled channel.

The breakage (3.3.6) and coalescence (3.3.1) kernels are closed with $S = 1$ and $C = 0.1$, respectively. The chosen values of the free-parameters leaded to a breakage dominant case of which 20 seconds simulations have provided the steady-state results within the transient-0D approach; this is the equivalent time of one complete flow-through in 1D steady simulations. The boundary condition is set at $x = 0$ with the same values for the initial condition of the transient case; and the initial values of the size and weight fields are set to the same values in both simulation, as well. Firstly, we wished to set zero initial-condition but we observed in the simulations that due to the sharp front the accuracy of the transported moment values decreases leading to a failure in the solution of the PDA: The PDA always provide a solution for $2n$ unknowns and $2n$ equations providing a system which has a unique solution but when the quantities are not transported sufficiently accurate, the solution may include negative values for the size or the weight; indeed, they are not acceptable. Thus, we preferred an homogeneous initial condition (same as the boundary condition); however, the initial condition is not crucial regarding the final results, since the steady state is sought.

The first computations involve the three grids with the mentioned different mesh sizes: L1 ($h = 1/40$), L2 ($h = 1/160$) and L3 ($h = 1/1000$). The Sauter mean diameter (d_{32}) which can be defined as the diameter of a sphere that has the same volume-surface ratio as a particle of interest is an accurate representative size for the particle ensemble and is equal to the ratio of m_3 to m_2, which is also an important variable of interest in chemical engineering applications. Therefore, we have computed the analytical solution of dimensionless d_{32} according to (4.3.3) and have compared the obtained numerical results against those.

The qualitative comparison shows that results of the finest grid (L3) computation and the analytical solution are visually indistinguishable; nonetheless, results of the lowest level (L1) computations slightly differ from the reference one. Thus, we have calculated means of absolute errors

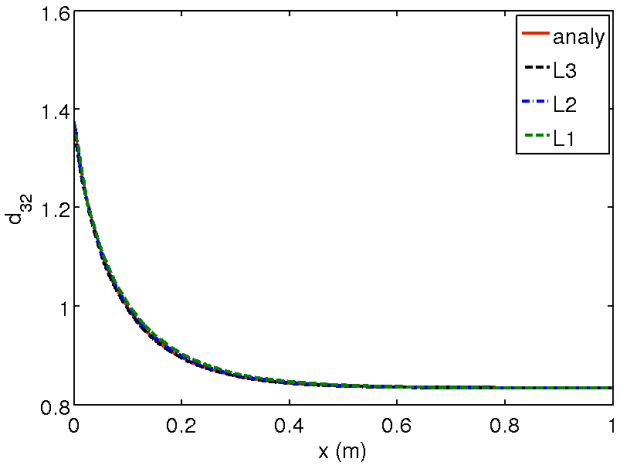

Figure 4.6: Evolution of dimensionless d_{32} in the channel for the steady-state at different grid levels, with steady solver.

and mean of percentage errors, aErr $:= \frac{1}{n}\sum_i^n |x_i - x_i^*|$ and pErr $:= \frac{1}{n}\sum_i^n \left|\frac{x_i - x_i^*}{x_i}\right| \times 100$ respectively, see Table 4.1.

Table 4.1: Mean absolute errors and mean percentage errors in the numerical results for different grid levels.

Level	aErr	pErr (%)
L1	1.40E-3	0.151
L2	5.77E-4	0.061
L3	5.69E-4	0.056

The calculated errors justify that our implementation is valid and the convection term is accurately discretized; nevertheless, the accuracy of the discrete convection operator decreases when a sharp front appears; indeed, this is due to the fact that the adopted AFC scheme mimics a low-order stabilization scheme in order to avoid under-/over-shoots in the vicinity of steep gradients.

Later, the same case has been studied with the developed transient solver; however, this time we adopted the *operator splitting approach* which can be more preferable within transient solvers, based on our preliminary studies. The same computational grids are used in these numerical computations, as well. We expect that since the steady-state results are sought, for which the time derivative vanishes, the obtained results should be independent of the chosen time-step size; though, we study the 2nd level computations with two different time-step sizes. First, a time-step size corresponding to the CFL number $C = 1$ has been chosen; later for L2 computation it has been chosen as 0.5 s ($C = 4$). The results of the computations at different grid levels for $C = 1$ are presented in Figure 4.7.

The first conclusion is that the coarse-level results are visibly different from the other two computations; moreover, it differs from the reference results more than L1 steady-computations. The quantitative analysis will be more helpful to draw more certain conclusions, see Table 4.2.

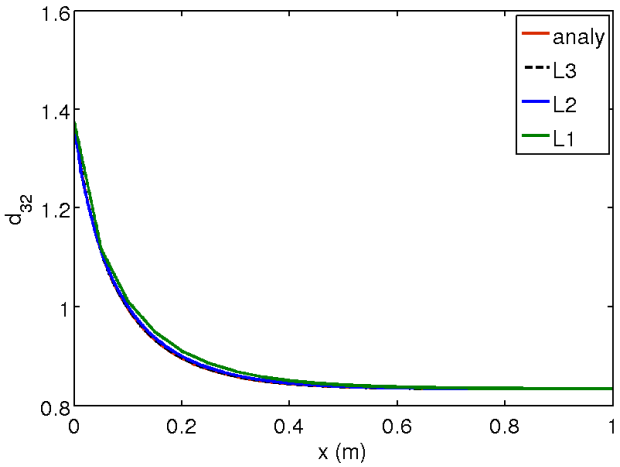

Figure 4.7: Evolution of dimensionless d_{32} in the channel for the steady-state at different grid levels, with transient solver.

Table 4.2: Mean absolute errors and mean percentage errors in the numerical results for different grid levels.

Level	aErr	pErr (%)
L1	3.5E-3	0.36
L2	7.4E-4	0.08
L3	5.7E-4	0.02

The mean absolute errors and the mean percentage errors nicely decrease with the grid refinement in the transient simulations, as well; especially, the mean percentage errors are very indicative. By comparing the mean error values in Table 4.1 and Table 4.2, we can say that adopting the operator splitting approach has reduced the accuracy for the lower mesh levels; nevertheless, at the finest grid it almost had no effect on the mean absolute error and reduced the mean percentage error. A conclusion is that operator splitting approach can cause loss of accuracy, in our approach, when the computational grid is not sufficiently fine; this conclusion can be extended to other approaches but it needs to be supported with more numerical experiments. Since the goal is only to study the accuracy of the developed computational tools so to validate them, this issue is not discussed further; and we conclude the discussion hereby stating that both approaches (explicit treatment and operator splitting approach) have been validated and they are highly accurate, even for very coarse grids.

Another point to be discussed is how accurate the time discretization shall be; since the steady state results should be free of error arising due to the time discretization, we reconsider L2 simulation with a four times large time step, see Figure 4.8.

As we have expected, the steady-state results are free of time discretization error, equal within the single-precision (7 significant digits); however, when intermediate results are compared, e.g., see Figure 4.8 for $t = 5\,s$, it is visible that the results slightly differ. The interesting point is that the discrepancy, which is not very significant, aErr=2.0E-3 and pErr=%0.23 (regarding the results

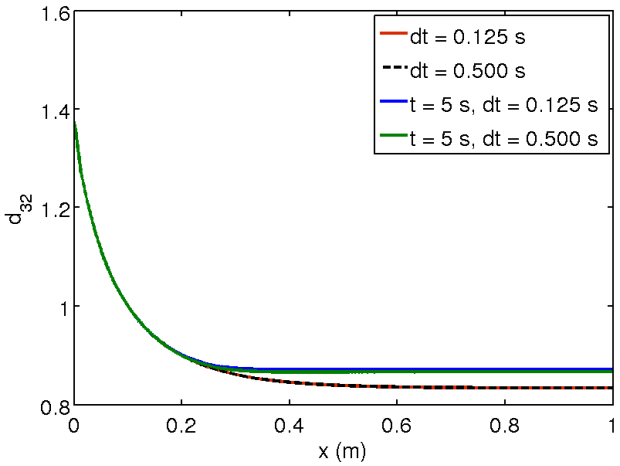

Figure 4.8: Evolution of dimensionless d_{32} in the channel for the steady-state at different grid levels, with transient solver.

with small time step as reference), is mostly through the outlet part which has not been influenced yet by the inflow. We can say that this loss of accuracy with the increased time step size is not due to the discrete reaction operator but it is caused by the explicit treatment of the PBE in the operator splitting approach. This is a consequence which was foreseen, yet is not a severe one; and, this amount of loss of accuracy is acceptable by considering the provided advantages by the operator splitting approach.

4.3.2. Comparison of PPDC vs MC within 3D Pipe-Flow

Accurately resolving the underlying turbulent flow field is a prerequisite for a subsequent population balance modeling in the framework of dispersed flows; moreover, there is no published benchmarked computational result for full 3D problems combining CFD and PBE [1]. Hence, we restricted our focus firstly to a relatively simple 3D problem. The 3D pipe-flow problem offers advantages: the validation of the flow field and distribution of turbulent quantities such as the dissipation rate of the turbulent kinetic energy (ε) to which the coalescence and breakage models are very sensitive.

The flow is characterized by the Reynolds number, $Re = \frac{dw}{\nu} = 114,000$ (w stands for the bulk velocity), that is influenced by the study of Hu et al. [41] who focused on one dimensional dispersed pipe flow modeling. All presented computational results in this section have been obtained by means of an extruded (2D to 3D) unstructured mesh employing 1344 hexahedral elements at each layer. The computationally obtained radial distributions of the temporally and spatially developed velocity- and turbulence-quantities are given in Figure 4.9 for dispersed flow simulations in a 1 m long pipe of diameter 3.8 cm and they are in agreement with the reference study [133].

The dispersed phase system is water which contains droplets of another immiscible liquid with similar physical properties to water, say oil (the physical properties are given in Table 4.3). This assumption and the fact that the flow is not driven by buoyancy but by the pressure drop enabled us *(i)* to neglect the buoyancy force, *(ii)* to approximate the dispersed phase velocity with the mixture velocity; so that, the developed one-way coupled PBE-CFD approach could be applied to simulate the dispersed pipe-flow. Additionally, the case study provides a good basis to compare different numerical methods to solve PBE, MC and PPDC in this study.

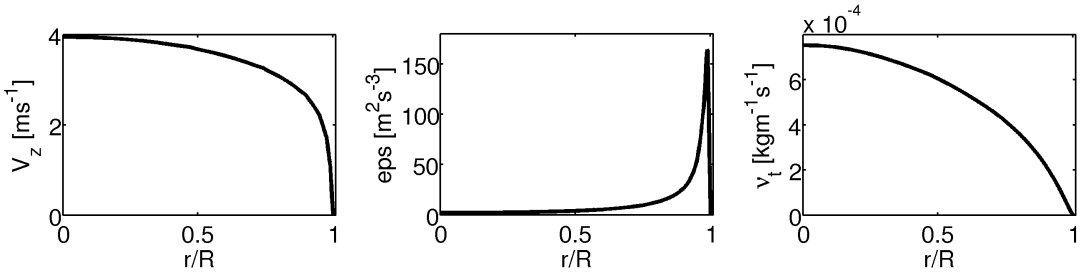

Figure 4.9: Radial profiles of the axial velocity component (left), turbulent dissipation rate (middle) and turbulent viscosity (right).

Table 4.3: Physical properties of the phases

Physical properties	Water	Oil
ρ (kgm^{-3})	1000	847
ν (kgm^{-1}s^{-1})	1×10^{-3}	32×10^{-3}
σ (Nm^{-1})	72×10^{-3}	21×10^{-3}
d_{32} (m)	–	1×10^{-3}

The CFD-PBE simulations involved 30 classes initialized by the discretization factor $q = 1.7$, which according to the previous 0D convergence studies turned out to be fine enough to reach approximately grid (internal coordinate) independent solutions. The feed stream is modeled as a circular sparger of a diameter of 2.82 cm containing droplets of a certain size ($d_{in} = 1.19$ mm) and of a certain holdup, $\alpha_{in} = 0.55$. Such an inflow holdup condition after reaching developed conditions ensures a flat total holdup distribution of a value $\alpha_{tot} = 0.30$. The same case is simulated with 3 parent classes by employing PPDC, as well; and the results are compared, see Figure 4.10–4.12 and Table 4.4.

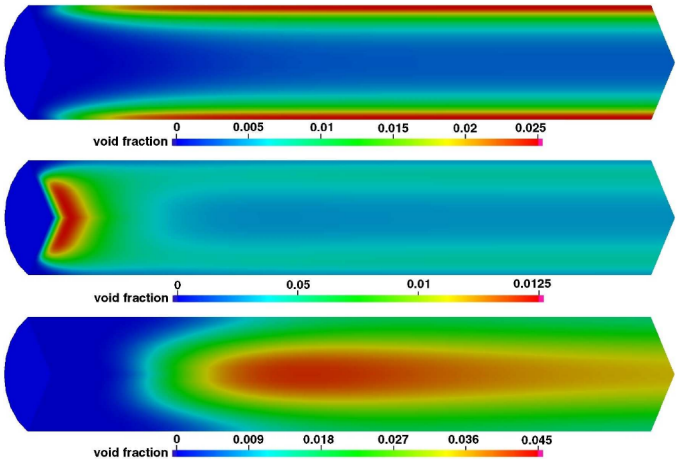

Figure 4.10: Holdup distributions of certain classes: 10, 17 and 23 (top to bottom).

In Figure 4.10, holdup distribution of the certain classes are shown; the holdup of small droplets, e.g. class 10, has higher holdup values in the vicinity of walls where the turbulent kinetic energy has the largest values. As ε values decrease in the inward radial direction, the coalescence

phenomenon dominates the breakage; so the droplet sizes enlarge, and the void fraction of larger classes increases far away from the wall region, see Figure 4.10. These results are also, indirectly, visible in the results of the simulation with PPDC, see Figure 4.11. In the wall region the number density of the particles is the largest since the Sauter mean diameter of the particles are the smallest (see Figure 4.12), and this result is justified with the 0'th order moment distribution in Figure 4.11 which corresponds to the number density distribution.

Both methods (MC and PPDC) yield to qualitatively almost the same results, it is visible if one compares, regardless of the color scale, the presented results in Figure 4.12. Nevertheless, the d_{32} value, which is an accurate representative value of a drop/bubble ensemble, the other statistical values as number density, interfacial area density and volume averaged diameter d_{43} have certain discrepancies, see Table 4.4. This result was expected regarding the previous comparison studies with the methods. The results differ because the suggested MC preserves only the 3rd order moment, which corresponds to the mass/volume conservation (with incompressible fluids), other moment-orders are preserved within only PPDC. The both methods predict the same evaluation of the secondary phase but with different accuracies. In *Section 3*, we have shown that the results obtained with MC converges to the ones with PPDC as the grid in the internal coordinate is refined. However, since it is not feasible to use so fine grids in 3D computations, and as the uncertainty/disparity in the population balance models can be larger than the errors due to the inaccuracy of the adopted numerical method, we conclude that the results which are obtained with both methods

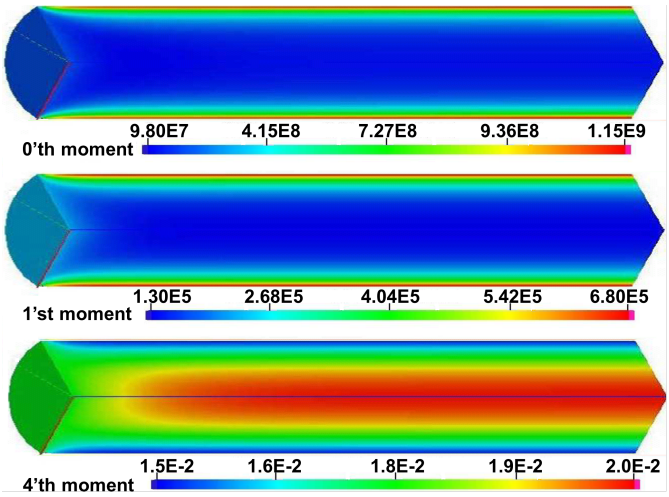

Figure 4.11: Fields of certain moment orders.

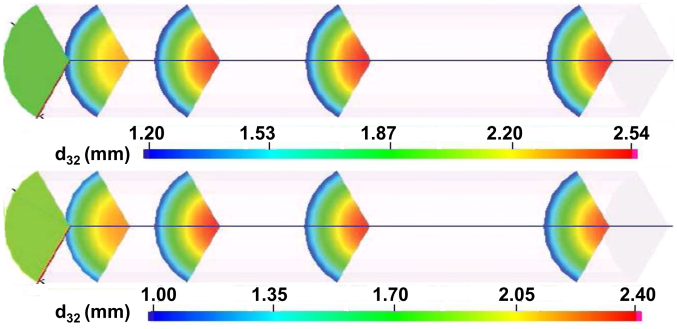

Figure 4.12: Sauter mean diameter distribution of the dispersed phase at different locations, $x = \{0, 0.06, 0.18, 0.33, 0.6\}$.

Table 4.4: Comparison of MC vs PPDC regarding to substantial variables.

$\begin{pmatrix} \text{MC} \\ \text{PPDC} \end{pmatrix}$	Cut-plane 1	Cut-plane 2	Cut-plane 3	Outlet
number	4.926E8	5.439E8	5.586E8	5.614E8
density (m^{-3})	2.782E8	3.338E8	3.511E8	3.536E8
interfacial area	1.064E3	1.094E3	1.114E3	1.125E3
density (m^{-1})	0.967E3	0.961E3	0.963E3	0.964E3
d_{32} (m)	1.51E-3	1.75E-3	1.80E-3	1.82E-3
	1.62E-3	1.83E-3	1.87E-3	1.95E-3
d_{43} (m)	2.81E-3	2.66E-3	2.72E-3	2.91E-3
	3.02E-3	3.08E-3	3.10E-3	3.10E-3

are acceptable.

During the computations with PPDC mainly two difficulties are encountered: when there is a sharp front in moment values, they are not transported sufficiently accurate, such that the reduced parent classes had negative values as the result of PDA. And, the time step size has to be smaller than the one which is adopted in the simulations with MC. In the simulation with MC, we had no difficulties and the required computational time was comparable; so that, although simulations with MC require solution of a larger number of scalar transport problem than with PPDC, the computations are equally affordable.

4.3.3. Comparison of PPDC vs MC within SMV™

Static mixers are tubular internals with optimized geometries to obtain desired dispersions/mixtures while the pressure driven flow is passing through the stationary mixer elements. Dispersion by static mixers is industrially preferable to dispersion by rotating impellers because it is mechanically simpler and frictional energy dissipation in the packing is more uniform, favoring a more uniform drop size distribution [155]. Thus, static mixers are very common applications in the industry; nevertheless, the numerical simulation of the dispersed systems in static mixer applications is very challenging due to the underlying complex turbulent flow field and the numerical computation of PBE.

Sulzer Chemtech Ltd. is a major producer of static mixers for various applications. This case study concerns the numerical simulation of a dispersed flow in Sulzer SMV™ static mixers, see Figure 4.13, which is used to obtain homogeneous dispersions within a short mixing-length and on the cost of an additional certain pressure-drop, for mainly oil–water dispersed systems. Narrow size distribution of droplets can be achieved due to the relatively homogeneous flow-field so to optimize and to control chemical processes. The Sulzer SMV™ mixing elements consist of intersecting corrugated plates and channels which lead to an efficient and rapid mixing action

in turbulent flow through the mixer. Therefore, they are ideal for a distributive and homogeneous dispersive mixing and blending action in the turbulent flow regime.

Figure 4.13: Laboratory scale Sulzer SMV™ static mixers, 3 adjacent mixer elements relatively rotated by 90°.

In literature there are many experimental and computational studies on static mixers in laminar and turbulent flow-regimes, a detailed review about static mixers is given in the study [156]; nevertheless, there is hardly any study which focuses on the numerical simulation of coupled CFD-PBE in static mixers. Moreover, there is no study which presents some results considering the size distribution; nonetheless, fortunately, Sulzer Chemtech Ltd. provided us experimental results for a certain case. In the scope of this section, the SMV^{TM} static mixer is studied in order to show the capabilities of the developed computational tools and compare the MC and PPDC methods for an industrial application.

The developed one-way coupled CFD-PBE approach makes it possible to numerically study the flow field and size distribution of droplets in static mixer applications by avoiding the excessive computational cost. Since the size distribution of the secondary phase is assumed not to influence the momentum field of the dispersion, it is possible to solve PBE for a given "frozen" flow field which is the quasi-stationary result of the turbulent flow simulations. Therefore, we will not discuss the CFD results but consider that they are given, and only numerical solutions of PBE (4.1.9) on this flow field is studied, i.e. simulation of the transport phenomenon in the internal and external coordinate on a given flow field is considered.

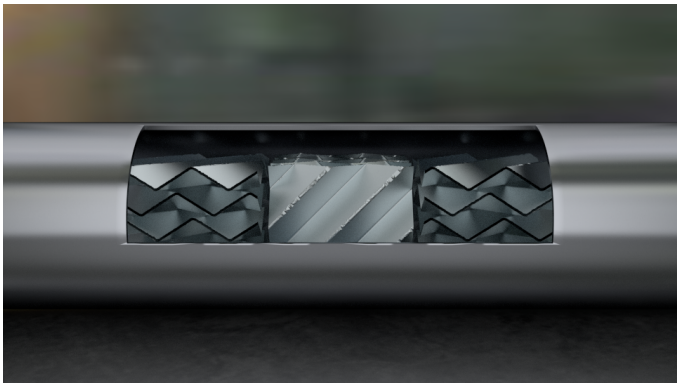

Figure 4.14: Computer modeled SMV™ static mixers.

The computational domain, see Figure 4.15, is meshed with $\approx 50,000$ hexahedral elements. The CFD results are interpolated onto a coarser grid with which the coupled problem is solved, see Figure 4.16. The coupled problem is studied with MC and PPDC; three parent-classes are employed with PPDC while forty-five classes are used with MC for which discretization constant q is 1.4, and the smallest class has the size of 0.5 mm.

The inflow condition is a flat velocity profile of value 1 ms^{-1}. *Do-nothing* and *no-slip* boundary

conditions are prescribed at the outlet and on the walls, respectively. The dispersed phase system is oil-in-water with 0.1 volumetric ratio of oil to mixture. In CFD simulations, the mixture is considered as a single phase whose physical property is a weighted average value of phases' physical properties with weight factors being volumetric ratios. Physical properties of the phases are the same with the ones given in Table 4.3. The initial droplets are introduced as a mono-dispersed phase with the Sauter mean diameter of 1.22 mm which corresponds to the 9th class. The same initial condition is applied for the simulation with PPDC such that one of the parent classes' size is chosen to match the desired size.

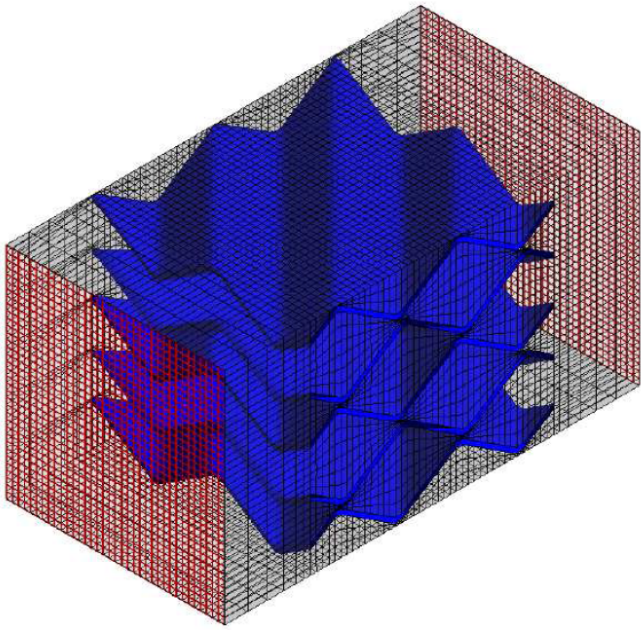

Figure 4.15: Computational domain for one SMV™ mixer element.

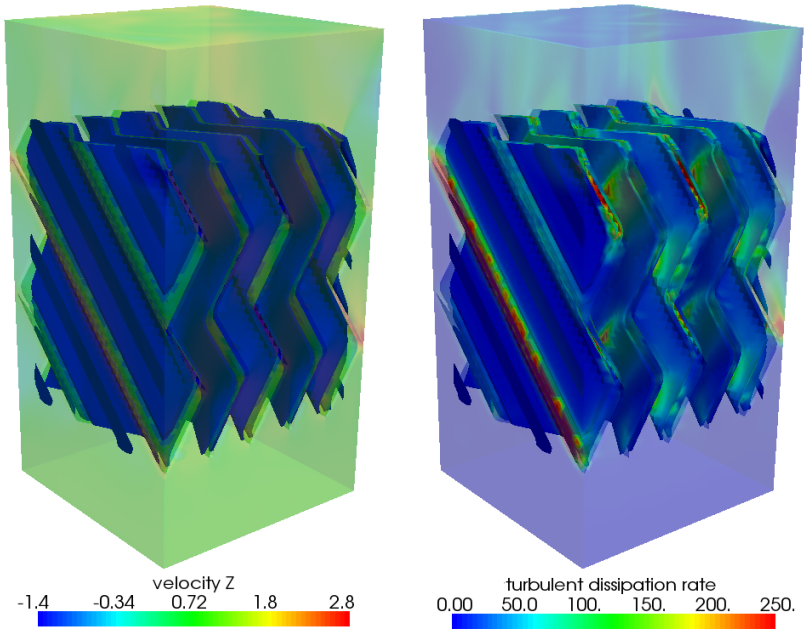

Figure 4.16: CFD results of the case with a flat inflow-profile of 1 ms^{-1}.

For the comparison of the cases, the solution of the PBE at the outlet has been several times prescribed as the inflow boundary condition such that the average Sauter mean diameter at the outlet does not change any more. Then, the Sauter mean diameters of the "stationary" results have been qualitatively compared, see Figure 4.17.

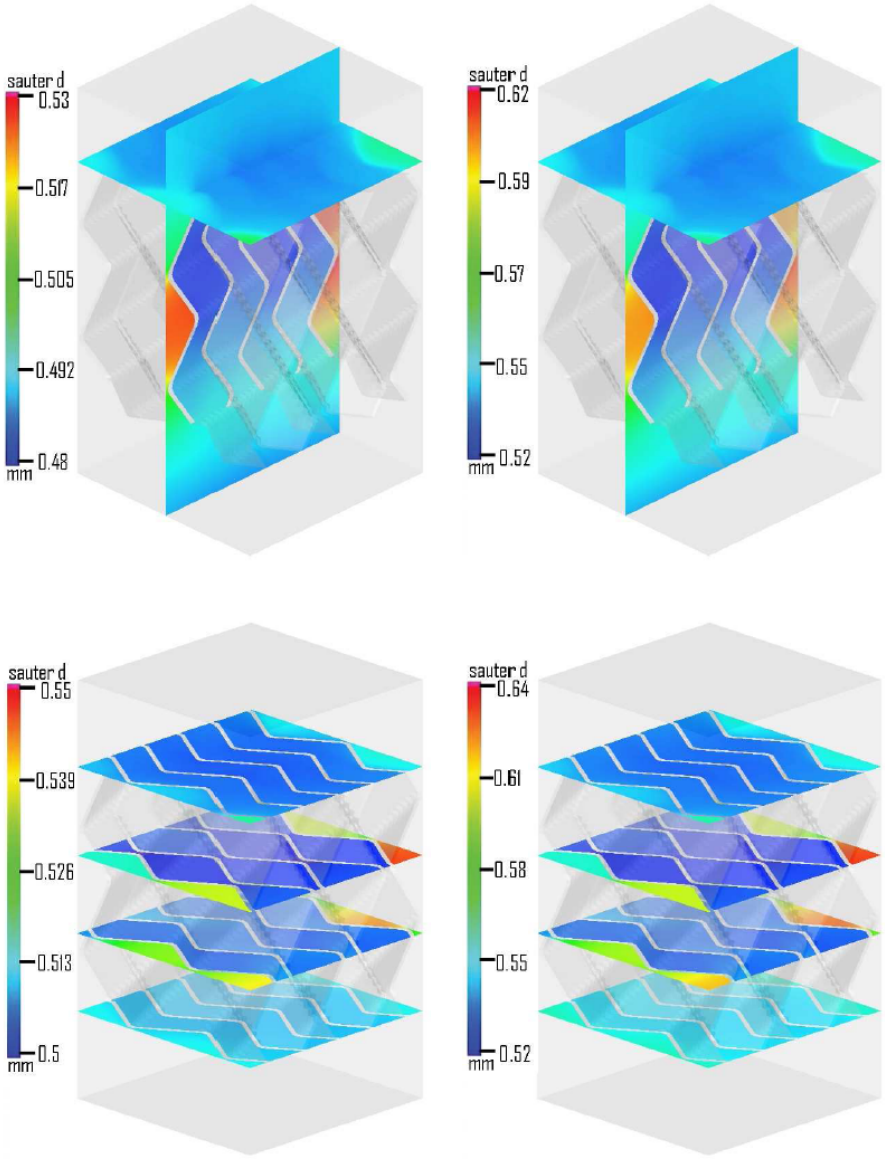

Figure 4.17: Comparison of MC and PPDC d_{32}values at certain cutplanes.

The qualitative comparison has yielded the same conclusion as in the case of pipe-flow, the evaluation of the secondary phase is predicted identically with both methods; nevertheless, as we have observed in the case of pipe-flow, PPDC has predicted d_{32} values slightly larger up to 10%. With these consistent results the implementation has been validated; nevertheless, we can not judge on the accuracy of the results due to lack of the reference/experimental results.

The simulations with PPDC have been troublesome, the negative results were arising due to insufficiently accurate transport of the moment values. In order to increase the accuracy of the transport step considerably small time step sizes had to be employed, one tenth of the time step used in the simulations with MC. On the other hand, without deteriorating the positivity

condition relatively fairly large time steps could have been employed in simulations with MC, and the simulations have never crashed. The MC is known to be less accurate and requiring the solution of larger number of scalar transport problems (one transport problem for each class), which leads to a large computational costs. On the other hand, since the time step sizes are restricted within PPDC, both methods requires equally expensive computations. One clear finding is that MC implementation is very robust; moreover, MC can directly provide the size distribution which is needed to be recovered from the existing moments in case of PPDC. Thus, we conclude that MC is a more favorable method than PPDC for the solution of coupled CFD-PBE problems in our scope.

4.4. Computational Studies for Verification

The developed computational tool needs to be verified for challenging cases, which can be, very well, industrial applications. Thus, numerically and computationally challenging cases which offer comprehensive and reliable experimental data are required. Unfortunately, there were no such cases; therefore, we needed to design experiments and conducted them at Sulzer Chemtech Ltd. laboratories, Winterthur, Switzerland.

Sulzer SMV™ static mixers are used as dispersers to obtain "steady" homogeneous dispersed flows. First, experiments with only one SMV™ mixer element have been conducted for varying inflow rates and holdup values of the secondary phase. Later, computationally and experimentally more difficult cases have been studied, three SMV™ mixer elements have been adjacently placed with 90°rotations (relative to the preceding one, see Figure 4.14). The mean droplet size distributions and the corresponding Sauter mean diameter values behind the mixer elements are compared for experimental data against numerical results. While we explain the numerical studies in detail at the coming subsections, details of experimental studies, such as, experimental rig, measurement devices and methods, evaluation of the measurements, and the accuracy of the experimental data, are discussed in *Appendix A*.

4.4.1. SMV™mixer applications

The dispersion by a single static mixer element is not a very common application, mostly several mixer elements are used adjacently; nevertheless, since the flow field can be resolved more accurately for one mixer element which has less complexity regarding the geometry, this case study concerns dispersed flow through a single static mixer element.

The developed one-way coupled CFD–PBE approach is employed to simulate the evaluation of the dispersed phase system on stationary flow fields which is obtained for the given inflow profiles as it has been explained in *Section 4.3.3*. Once the stationary solution of PBE is obtained, the space averaged size distributions and the corresponding Sauter mean diameters are calculated.

The computational domain is the same one which has been used in *Subsection 4.3.3*, see Figure 4.15. The numerically simulated experiments consist of cases for flat inflow profile with varying velocities and holdup values. Three inflow velocities $1\,\mathrm{ms}^{-1}$, $1.25\,\mathrm{ms}^{-1}$ and $1.5\,\mathrm{ms}^{-1}$ are chosen, and three holdup values of the secondary phase 0.05%, 0.10% and 0.15% have been studied for each inflow profile. The chosen values, for both velocity and holdup, mostly cover the moderate operating conditions. The experimental set-up is based on visual observation, and the

extreme operation conditions yield to dispersions which are not possible to accurately observe; therefore, the higher values of holdup, and inflow profiles with larger velocities are not studied.

The discretization in the internal coordinate is achieved with 45 classes such that the smallest class-size is 0.03 mm and the discretization constant q is set to 1.38. The initial size of the droplets is 1.2 mm which corresponds to the size of the 35th class. The physical properties of the phases are as given in Table 4.3, and the interfacial tension value is $0.043\,\mathrm{kgs}^{-2}$.

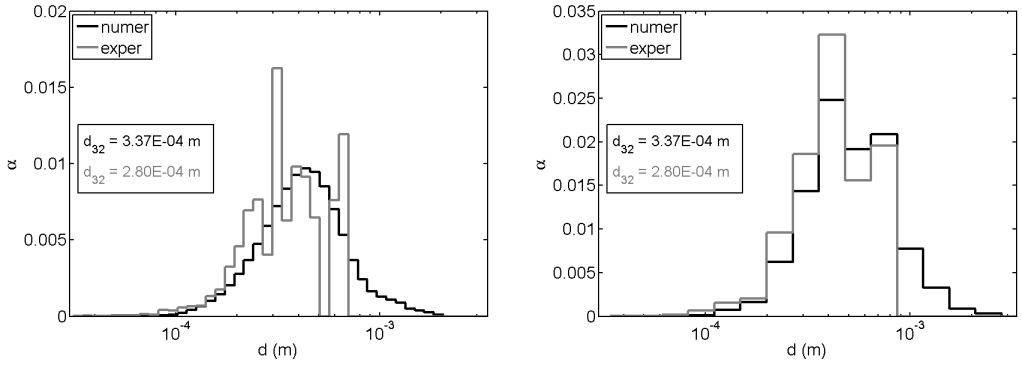

Figure 4.18: An example for mapped results from fine grid to coarse, inflow of $1.5\,\mathrm{ms}^{-1}$ and $\alpha = 10\%$.

A very large number of droplets was required to be manually measured in order to obtain a "smooth" distribution curve such that in all the classes there would be enough number of droplets to represent the size distribution. On the other hand, while we are evaluating the experimental results, we have seen that ensembles of 300-350 bubbles have almost the same Sauter mean diameter value, with 15×10^{-6} m discrepancy, for more details see *Appendix A*. Therefore, a coarser internal grid is obtained by adopting 17 classes (the coarse and internal grids cover the same range of size coordinate) so that 300-350 counted droplets yield to a "smooth" size distribution, see Figure 4.18. Then, both numerical and experimental results are evaluated on this coarse grid, see Figure 4.19; however, results with fine grid are used to plot the cumulative holdup values with respect to size, see Figure 4.20.

When the plots at the first row and the first column in Figure 4.19 or Figure 4.20 are considered, the agreement in the results is more than being satisfactory; especially, for the cases with 5% holdup (the first column), the discrepancy between the numerical and experimental results remain less than %12 which is a surprisingly small disagreement regarding the complexity of the problem, or the results in *Section 3.4.2* which present comparison of different closures. This good agreement of the results motivated us to study more challenging cases with multiple mixer elements.

Applications with static mixers to obtain the desired dispersed phase system usually involve multiple static mixer elements which may be placed adjacently or with certain distances between each other. In case of Sulzer SMV™ static mixers, it is very common to have several mixer elements adjacently and relatively rotated with 90°, which exhibits a very complicated geometry and a highly turbulent flow field; therefore, we have also studied the cases with three mixer-elements to see the prediction capability of the developed computational tool, see the geometry in Figure 4.14. The new geometry is studied analogously to the single mixer-element studies, and three inflow-velocities $1\,\mathrm{ms}^{-1}$, $1.25\,\mathrm{ms}^{-1}$ and $1.5\ \mathrm{ms}^{-1}$ are chosen, and three holdup values of the secondary phase 0.05%, 0.10% and 0.15% have been studied for each inflow profile; the results are given in Figure 4.21–Figure 4.22.

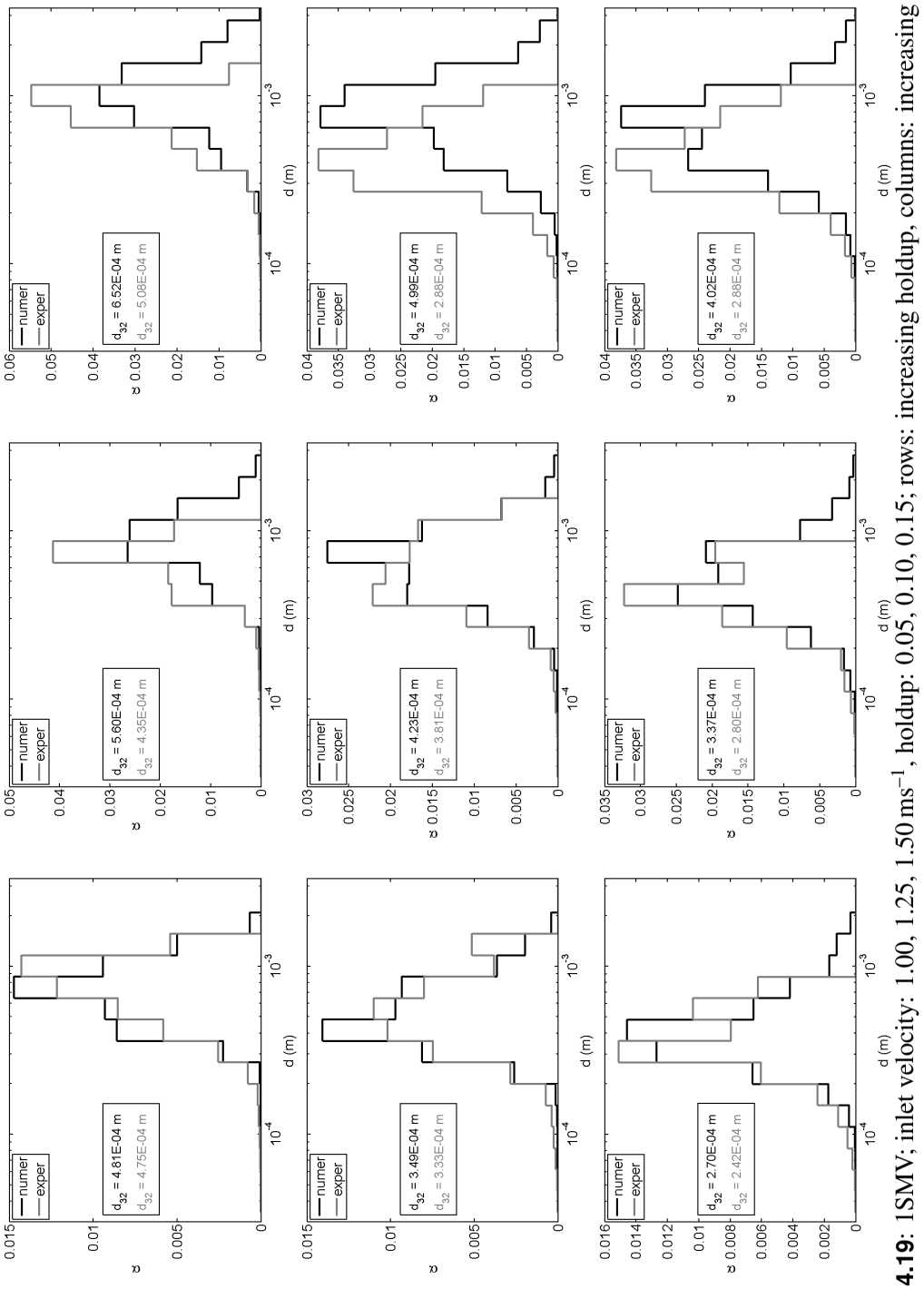

Figure 4.19: 1SMV; inlet velocity: 1.00, 1.25, 1.50 ms^{-1}, holdup: 0.05, 0.10, 0.15; rows: increasing holdup, columns: increasing velocity.

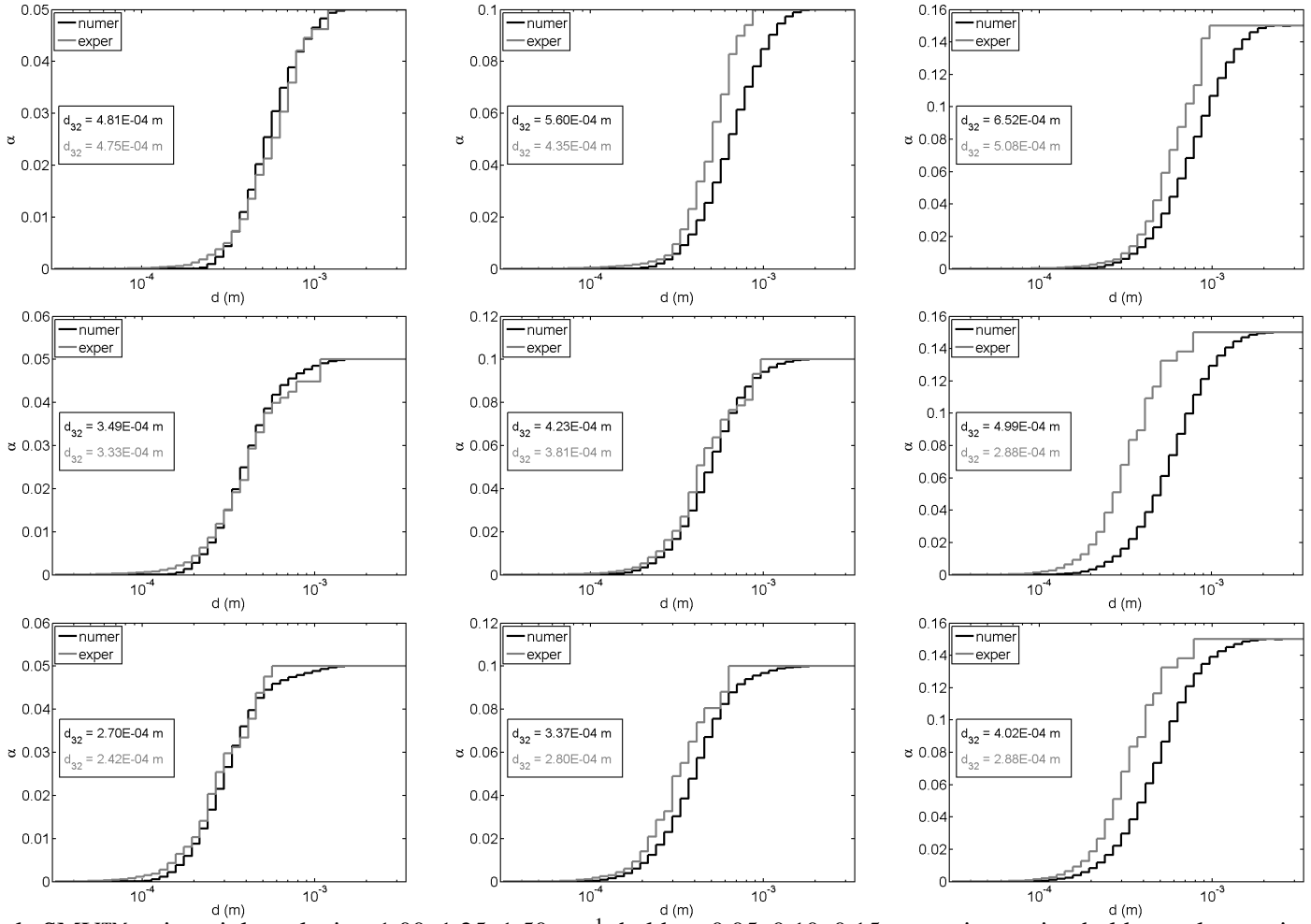

Figure 4.20: Single SMV™ mixer; inlet velocity: 1.00, 1.25, 1.50 ms^{-1}, holdup: 0.05, 0.10, 0.15; rows: increasing holdup, columns: increasing velocity.

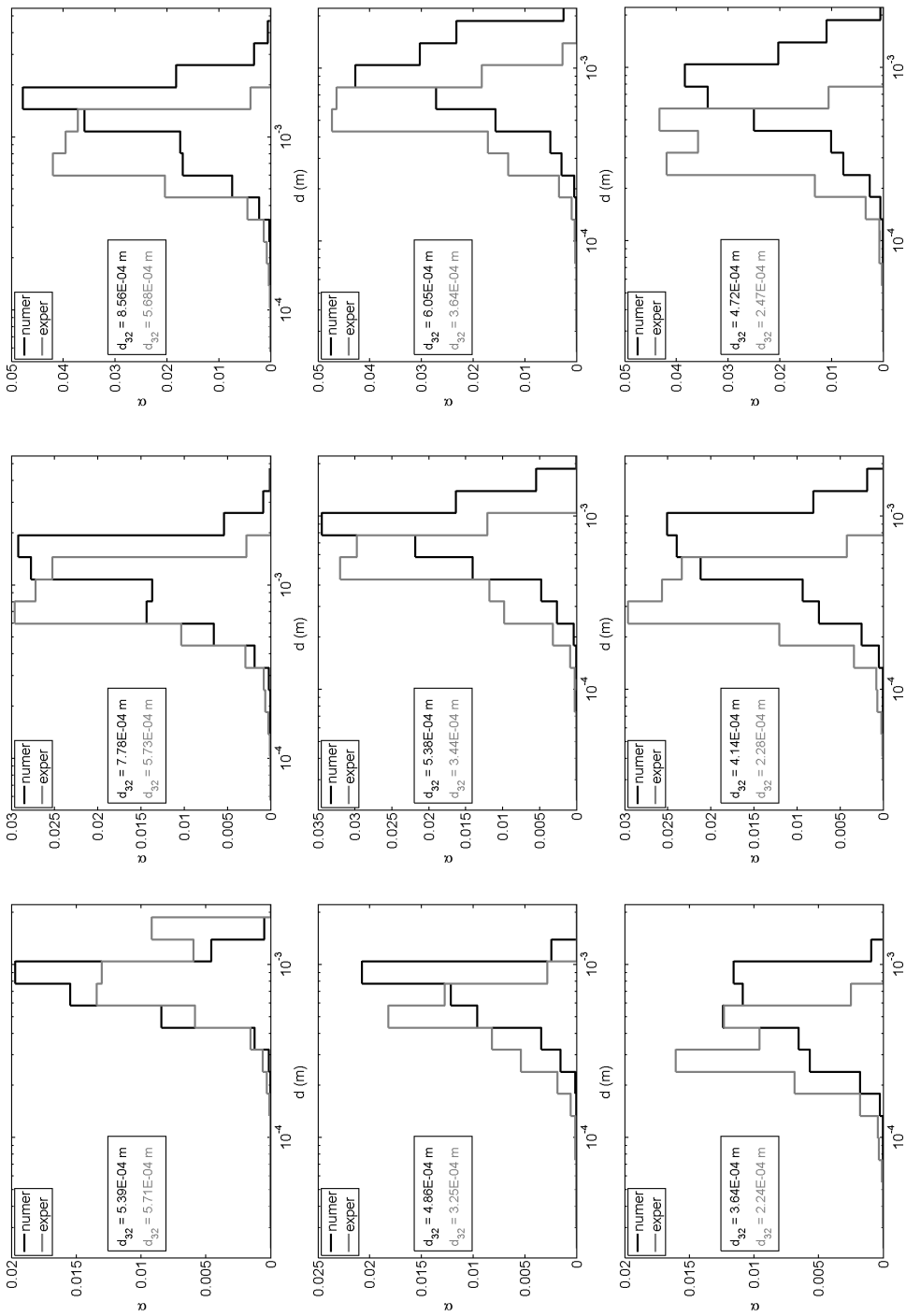

Figure 4.21: 3SMV; inlet velocity: 0.75 1.00, 1.25 ms^{-1}, holdup: 0.05, 0.10, 0.15; rows: increasing holdup, columns: increasing velocity.

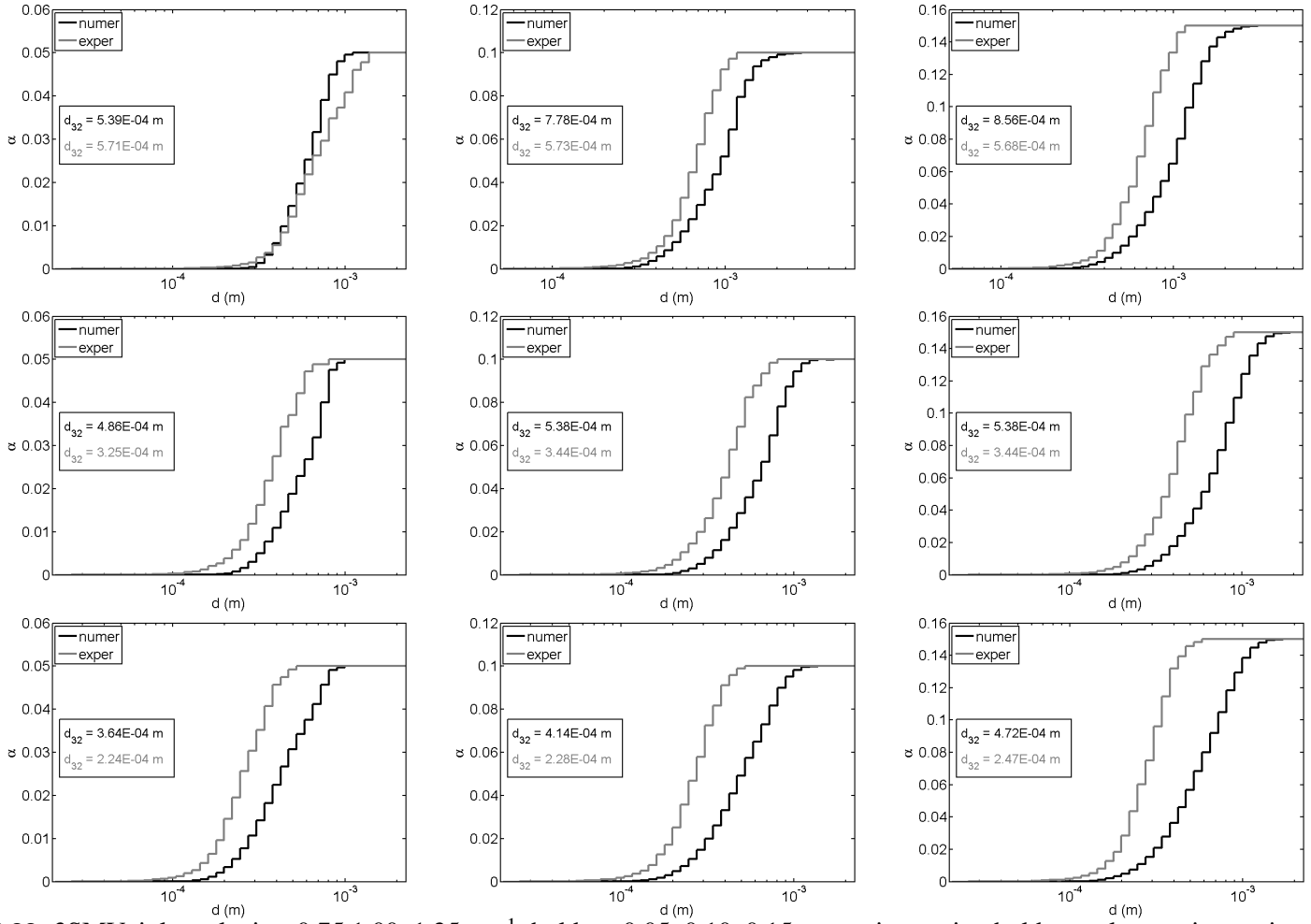

Figure 4.22: 3SMV; inlet velocity: 0.75 1.00, 1.25 ms^{-1}, holdup: 0.05, 0.10, 0.15; rows: increasing holdup, columns: increasing velocity.

Even the results show that the later cases (3SMV) are more challenging. For the case $v = 1\,\mathrm{ms}^{-1}$ and $\alpha = 5\%$ the results are in a surprisingly good agreement, with a 5% discrepancy. Not only the Sauter mean diameter is obtained very accurately, the size distribution of the droplets is precisely captured, see Figure 4.21. On the other hand, for the case with three mixer-elements (3SMV) the accuracy of the numerical results is clearly less than the one for the single mixer-element case (1SMV), see differences between the curves at the plots for cumulative holdup values in Figure 4.20 and Figure 4.22. Considering this is the first study which compares numerically and experimentally obtained size distributions of dispersed phase systems in static-mixer applications, the results are very satisfactory; especially for 1SMV cases and the cases with low holdups and low velocities for 3SMV.

The closures of PBE, breakage and coalescence kernels, are mostly modeled for lean dispersions, and their prediction capabilities get worse with the increasing holdup values. Researchers have still been working on developing coalescence and breakage kernels which will be good for higher holdup values and the mostly encountered difficulty is to obtain accurate measurements and data in experiments with high holdup values.

CFD results of less turbulent flows are more reliable because as the Reynolds number increases, the effect of the unresolved subgrid scales becomes more influential on the main flow, which leads to more uncertainty and lack of accuracy in the results. Moreover, we have assumed that momentum interchanges between the phases are negligible so the discussed single phase model was used in CFD calculations; thus, the effect of change of the holdup value on the flow field could not be accurately simulated. Although the physical qualities of the fluids are very similar, this assumption is certainly less accurate for the high volume fractions of the secondary phase than it is for lean dispersions.

The modeling assumptions and kernel-related-inaccuracies are not the only reasons of discrepancies between the results; the experimental results also have certain inaccuracies. First of all, the pictured droplets can be more accurately evaluated for low hold up and velocity values. Figure 4.23 shows two pictures captured for high and low holdup values.

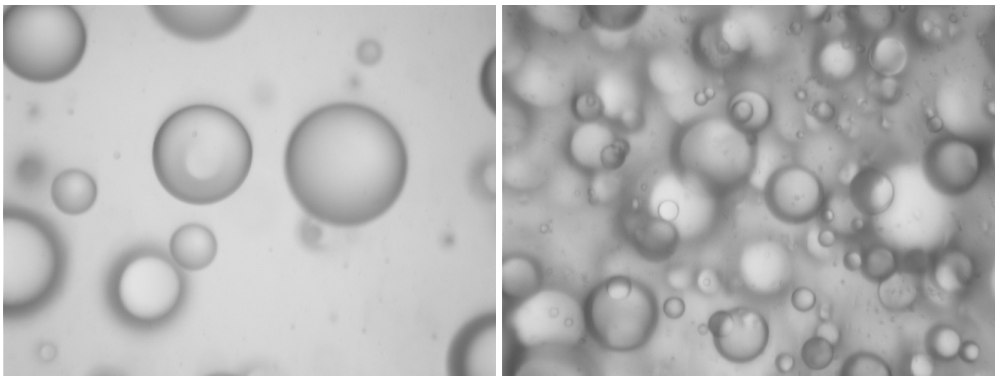

Figure 4.23: Pictures are taken during experiments by LLISA; left: $v = 1.00\,\mathrm{ms}^{-1}$ and $\alpha = 0.05$, right: $v = 1.50\,\mathrm{ms}^{-1}$ ms^{-1} $\alpha = 0.20$.

The droplets are sharper and can be more easily and accurately measured in Figure 4.23 on the left (see *Appendix A* for details on evaluating the pictures) whereas on the right the evaluation of the droplets is very troublesome. In addition, the distance between the flash and camera windows of LLISA should be small to obtain clear pictures for higher holdup values or when the flow is highly turbulent but this can be a crucial mistake to do. Since the distance between the two windows is not sufficiently large, the large droplets can not pass through the control volume so

they are not captured in snapshots. This argument is supported with the experimental results in Figure 4.21. When the cases for the same velocity and different holdups are (column-wise) compared, the largest measured droplet is getting smaller in the experimental results. However, there is no physical explanation of this consequence; actually, it should be the other way around according to population balance models. It is clear that there is a limitation for the largest droplet which can be measured; and, most probably, this restriction is the distance between two windows of LLISA. While taking pictures for the case with higher holdup, the distance was narrowed down in order to shot clear pictures; hence, it had not been possible to capture the large droplets.

The differences in the results can not be explained only with the fact of not being able to capture the large droplets. The calculated size distribution of droplets shifts through large classes much faster than the measured ones do when the secondary phase has higher holdup; compare the plots row-wise in Figure 4.19 and Figure 4.21. The coalescence rate should increase faster comparing to the breakage rate with the increase of holdup value; and, the breakage rate of the large droplets is slower than their coalescence rate. The comparisons show that there is a certain difference between the measured and computed smallest droplet sizes, numerical solutions always predict the existing smallest droplet to be larger than in the experiments; see Figure 4.19 and Figure 4.21, especially for the the largest velocity case. This consequence arises due to the daughter size distribution (DSD) of the breakage kernel (3.2.11), DSD provides a distribution curve starting from a large minimum size. These issues can be resolved by further modeling of the adopted kernels or by employing more suitable kernels, which we have not been able to determine yet.

Briefly, the accuracy of the numerical results are satisfactory; nevertheless, in certain cases there are large discrepancies, especially for the dispersed systems with large holdup and highly turbulent flow-fields. According to our discussion, the disarrangement of the results are mostly due to the systematic errors in the experimental studies, but also the closures of PBE and turbulent flow simulations have certain inaccuracies. To judge on the accuracy of the employed numerical methods is not possible with these experimental results, due to the mentioned uncertainties; however, the numerical methods on which the computational tool is based provided a very robust and acceptably efficient solver for CFD-PBE coupled problems, even for very challenging cases like industrially used static-mixer applications.

5

PBE and CFD: Two-way coupling

The dynamics of bubble columns has been a very interesting topic to researchers in the field of CFD for the last several decades, and many different methods have been developed. The process is very elaborate, and our understanding on different parts of the problem is very limited. Therefore, there is no unified framework of mathematical modeling or the numerical approaches for bubbly flows.

A comprehensive review of the studies in modeling of bubble columns and on the numerical solution approaches is given by Jakobsen et al. [13]. Numerical simulations of bubbly flows are generally realized by adopting either the Euler-Lagrange approach or the Euler-Euler approach. For practical reasons, e.g., high numerical efforts and computational costs which are related to tracking and calculating the motion of each bubble individually in the flow field, the former method is restricted to be applied on lean dispersions for small systems while the later method requires less effort in both numerics and computation and can be employed for large scale systems, as well. Nevertheless, both of the methods lead to the same results if the problems are handled with accurate numerics and adequate computational effort, as it has been reported by Sokolichin et al. [134]. We followed Sokolichin et al. and adopted the Euler-Euler approach to solve the fluid equations coupled with PBE.

In the Euler-Euler approach, one should employ one of the following models: mixture model, two- and multi-fluid model. Solving the continuity equation for two-/multi-fluid models is very troublesome because the continuity has to be satisfied with the numerical solutions of the weakly coupled phase velocities, that exhibit a great numerical challenge for Navier-Stokes solvers [10], especially for segregated ones. The choice of the fluid model is not independent of how the PBE are coupled to the flow part. One-way coupled CFD-PBE models can not comprehensively describe the dynamics of bubble columns. Therefore, a two-way coupled CFD-PBE model is required and beginning from the employed discretization method for the internal coordinate, each adopted approach influences the decision on the fluid model.

The numerical simulations which assume the dispersed flows to be laminar are not able to

produce mesh independent results. The finer the grid, the more vortices are resolved; this is more typical for turbulent flows [161, 162]. Turbulence models which are applicable to produce results with an acceptable accuracy and reasonable computational cost generally originate from the family of two-equation eddy viscosity models. In this sense, most preferred models are related to the standard or modified k-ε turbulence models which have been implemented in several commercial CFD programs and in-house codes, including FEATFLOW [1]. This is another reason that we adopted the Euler-Euler approach; otherwise, to be able to fully resolve the flow field by using direct numerical simulation and by tracking the each bubble with an appropriate method – naming the most widely used: volume of fluid, level-set – would require unaffordable computational cost.

The turbulent flow simulations, especially standard k-ε turbulence models, require relatively coarse grids compared to direct numerical simulations; moreover, PBE require even coarser grids and they do not need to be solved on same computational grids (in space, and in time as well) with the flow equations due to excessive computational costs. The first attempt to reduce the required computational afford may be the compartment method [127] which is based on the idea of dividing the computational domain into very large units, namely compartments, and solving the PBE in each compartment with mean values of flow-field variables. This method can be employed to simulate liquid-liquid dispersions in stirred tanks for which certain regions have quasi-steady flow behavior [43] whereas for the applications like bubble columns, i.e., when the interaction of the phases should be considered in a two-way direction, the compartment method is not good anymore; and, the PBE must be solved for the flow problem's number of degrees of freedom (dof). If one considers that the number of required compartments is on the order of 10 but numbers of dof is on the order of 10^4 and more, it is clear that the computational cost dramatically increases. Moreover, now the non-linear scalar transport problem needs to be solved for the dispersed phase. And, all these add up to an enormous computational effort hence the use of efficient numerical techniques are of predominant importance.

A comprehensive PBE-CFD model involves a two- or multi-fluid model for the momentum balance [13]. If all the bubbles are assumed to share the same velocity field, only one momentum equation is solved for the dispersed phase, which is very common when a moment based method is adopted to solve PBE; it is also used with MC [101, 102]. Nevertheless, additional convection-diffusion-reaction (CDR) problems have to be solved when either method is employed. These problems are either transport of the low-order moments or certain property (properties) of classes (multi-dimensional PBE); and, the number scales with the required number of moments or the employed number of classes. However, multi-fluid models can be more preferable when MC is chosen; then, a separate momentum equation is solved for each class. Then, there are three main difficulties which are inherited from multi-fluid models independent of PBE: *(i)* satisfying the continuity equation, *(ii)* excessive computational costs of the matrix assembly, *(iii)* determining the interphase forces. There are many studies on how to write continuity equation for multiphase flows such that the incompressibility constraint is satisfied with the solution of separate momentum equations for each phase. Moreover, not only solving a large number of transport problems is challenging, another problem is to determine the appropriate advection velocity, especially for the moment based methods [163, 164]. The size of the second difficulty can be understood better, if it is considered that each class is a separate phase, for each one the discrete convection operator has to be assembled, and the cost of assembling the convection matrix is much more than solving the associated linear equation with the CDR problem.

The third difficulty should be considered in detail since it is the coupling term between the momentum of the phases. There are three main interphase forces, the virtual mass force (f_{VM}), the lift force (f_{L}) and the drag force (f_{D}); and, we prefer to work only with the drag force. The drag

force is the only force which has significant influence and a clear definition even tough there are various definition of it. On the other hand, f_{VM} is not very influential and can be freely neglected for the sake of reducing the computational cost.The lift force has extremely deviating formulations; moreover, it is frequently abused for fitting numerical results to experimental data [146, 165].

We preferred a simplified model and tackled the problem within the Euler-Euler approach. The dispersed system is considered as a mixture and a single momentum equation is solved for the fluid in the framework of the mixture-model and the algebraic slip relation is employed to recover the gas phase velocity. Discretized PBE with MC are coupled to turbulent flow equations in a two-way fashion. While the hydrodynamic variables are coupling the PBE equation to flow solutions, the formulation of the drag force requires the solution of PBE. The turbulence is modeled with the standard turbulence model and buoyancy induced turbulence; buoyancy is handled with a relaxed Boussinesq approximation. Then, the continuity equation of the mixture is solved with the constant density assumption, the local gas holdup is calculated regarding the ideal gas law. We assume that all the bubbles share the same velocity field, which is obtained by using the Sauter mean diameter of the population within the algebraic slip relation.

Next, we present the governing equations and our approach to the numerical solution of these equations with specifying the employed numerical methods; the discussion will be focused more on the mathematical model and rewriting it such that it can be solved with the computational tools that we have so far developed. Later, we study the Becker's experiment which concerns bubbly flows (particularly, bubble swarm motion) in a flat bubble column which yields a flow field characterized by 2D motion of bubble swarm.

5.1. Mathematical model and numerical approaches

The developed complete mathematical model is based on an Euler-Euler approach and consists of three parts: *(i)* the hydrodynamic core, a model to solve "incompressible" Navier-Stokes equations; *(ii)* the simplified two-fluid model based on an analog of Boussinesq approximation for natural convection problems; *(iii)* PBE to describe the size distribution of the dispersed phase; the schematic view of how these models are connected is given in Figure 2.1 (it is recalled below).

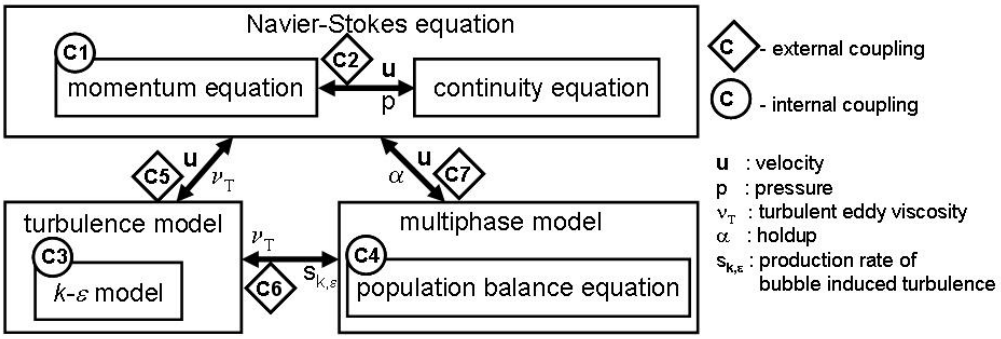

The second part restricts the model to be valid for bubbly flows with moderate gas holdups (up to 10%). Under such circumstances, incompressible Navier-Stokes equations are enriched with an extra buoyancy force term, that characterizes the gas-liquid mixture as a weakly compressible fluid. Consequently, the dispersed phase system can be considered as space-sharing interpenetrating continua. The major advantage of this approach is that the computational cost is independent

of the number of bubbles to be simulated.

Replacing the effective density $\tilde{\rho}_L$ by the liquid density ρ_L except for the gravity force leads the Navier-Stokes equations for the liquid phase in the following:

$$\begin{aligned} &\frac{\partial \mathbf{u}_L}{\partial t} + \mathbf{u}_L \cdot \nabla \mathbf{u}_L = -\nabla p_* + \nabla \cdot (\nu_T \mathcal{D}(\mathbf{u}_L)) + e\mathbf{g}, \\ &\nabla \cdot \mathbf{u}_L = 0, \qquad p_* = \frac{p - p_{\text{atm}}}{\rho_L} + \mathbf{g} \cdot \mathbf{x}, \qquad e = \frac{\tilde{\rho}_L}{\rho_L} \end{aligned} \tag{5.1.1}$$

where $\mathcal{D}(\mathbf{u}) = \nabla \mathbf{u} + \nabla \mathbf{u}^T$ and the effective viscosity $\nu_T = C_\mu \frac{k^2}{\varepsilon}$ is a function of the turbulent kinetic energy k and its dissipation rate ε. The continuity equation of the gas phase and the evolution of these quantities are described, respectively, by the following transport equations:

$$\frac{\partial \tilde{\rho}_G}{\partial t} + \nabla \cdot (\tilde{\rho}_G \mathbf{u}_G) = 0 \tag{5.1.2}$$

$$\frac{\partial k}{\partial t} + \nabla \cdot \left(k\mathbf{u}_L - \frac{\nu_T}{\sigma_k} \nabla k \right) = P_k + S_k - \varepsilon, \tag{5.1.3}$$

$$\frac{\partial \varepsilon}{\partial t} + \nabla \cdot \left(\varepsilon \mathbf{u}_L - \frac{\nu_T}{\sigma_\varepsilon} \nabla \varepsilon \right) = \frac{\varepsilon}{k} (C_1 P_k + C_\varepsilon S_k - C_2 \varepsilon). \tag{5.1.4}$$

The production terms $P_k = \frac{\nu_T}{2} |\nabla \mathbf{u} + \nabla \mathbf{u}^T|^2$ and $S_k = -C_k e \nabla p \cdot \mathbf{u}_{\text{slip}}$ are due to the shear and bubble-induced turbulence (BIT), respectively. The involved constants $C_\mu = 0.09$, $C_1 = 1.44$, $C_2 = 1.92$, $\sigma_k = 1.0$ and $\sigma_\varepsilon = 1.3$ for the standard $k-\varepsilon$ model are known with high precision, whereas the BIT parameters $C_k \in [0.01, 1]$ and $C_\varepsilon \in [1, 1.92]$ are highly problem-dependent. After decomposition of the interphase force term responsible for momentum exchange between the present two phases and using the assumptions introduced by Sokolichin et al. [165, 166], the momentum balance of the gas phase reduces to:

$$0 = -\alpha \nabla p - \alpha C_W \mathbf{u}_{\text{slip}}, \qquad C_W = C_D \frac{3}{8} \frac{\rho_L}{r} |\mathbf{u}_{\text{slip}}|. \tag{5.1.5}$$

And the term r (radii of bubbles), appearing in the definition of the C_W linearization parameter, couples the system to PBE. One common practice is to adopt a certain value for r and having a model without PBE; however, this is not a general solution, even though it may lead to acceptable results for specific cases. Moreover, even $\mathbf{u}_{\text{slip}}$ can be considered having a certain value depending on the initial and boundary conditions so that the model is further simplified. Nevertheless, we wish to investigate the effect of size distribution of the bubbles on the bubble swarm motion hence we incorporate our fluid model with PBE which yields to again (4.1.9). Let us recall this equation in the conservative form:

$$\begin{aligned} \frac{\partial f}{\partial t} + \nabla \cdot (\mathbf{u}_G f) - (\nabla \cdot \frac{\nu_T}{\sigma_T} \nabla f) \; = \; & \int_\upsilon^\infty r^B(\upsilon, \tilde{\upsilon}) f(\tilde{\upsilon})\, d\tilde{\upsilon} - \frac{f(\upsilon)}{\upsilon} \int_0^\upsilon \tilde{\upsilon} r^B(\tilde{\upsilon}, \upsilon)\, d\tilde{\upsilon} \\ & + \frac{1}{2} \int_0^\upsilon r^C(\tilde{\upsilon}, \upsilon - \tilde{\upsilon}) f(\tilde{\upsilon}) f(\upsilon - \tilde{\upsilon})\, d\tilde{\upsilon} - f(\upsilon) \int_0^\infty r^C(\tilde{\upsilon}, \upsilon) f(\tilde{\upsilon})\, d\tilde{\upsilon}. \end{aligned}$$

We comprehensively discussed the numerical solution of this integro-partial differential equation in *Chapter 4* by specifying the required numerical methods and the algorithms. In two-way coupled fashion, this equation exhibits strong internal and external couplings, *C4*, *C6*, and *C7* (see Figure 2.1). The external couplings are due to the turbulent diffusivity and the velocity which are given with $\frac{\nu_T}{\sigma_T}$ and $\mathbf{u}$. The internal couplings are more apparent when the discrete counter part of (4.1.9) is considered, (4.2.24). One important remark here is about the treatment of the diffusivity;

as the air bubbles are accepted non-diffusive in water, there should have been no diffusion in our model; however, since the fluid dynamics is modeled with RANS model, the turbulent viscosity arises which is responsible for the diffusive term in (4.1.9).

As in the case of oil-in-water dispersions, the turbulent diffusivity can be very small such that with an over-diffusive stabilization scheme for the convection term the introduced numerical diffusion to the solution can be much more than the calculated/physical one. Therefore, high-resolution positivity preserving schemes are required, which have been already developed and employed for the solution of this sort of problems in *Chapter 4*. Here, we have employed again the implicit high order finite elements method with AFC and positivity preserving linearization scheme for the spatial discretization.

PBE can be coupled to fluid dynamics equations either in one-way fashion or two-way fashion. In one-way fashion, the underlying presumption is that the dispersed phase do not influence the fluid dynamics but the flow field has an influence on the evolution of the secondary phase; that is very suitable to model, for instance, moderately mixed oil-water systems or similar dispersed systems, as it was studied in *Chapter 4*. Our studies on the one-way coupled PBE-CFD models have shown that with the proper implementation these models leads to acceptable results for the flows of oil-in-water dispersions in complex geometries like static-mixers (see the results in the previous chapter) [1, 167]. In case of air-in-water dispersed systems, it is not possible to assume that the dispersed system has no influence on the dynamics of the primary-phase. Therefore, we realized the coupling of PBE and CFD in a two-way fashion so the $C7$ and $C6$ external couplings were taken into account in both directions. In the mathematical model, back coupling (influence of PBE on fluid model) arises due to the definition of the slip velocity which is obtained from (5.1.5) as,

$$\mathbf{u}_{\text{slip}} = -\frac{1}{C_D \frac{3}{8}\frac{\rho_L}{r}|\mathbf{u}_{\text{slip}}|}\nabla p, \qquad \text{where} \quad C_D = 0.666\,. \tag{5.1.6}$$

Before discussing further how to obtain the slip velocity, we introduce the gas velocity (5.1.7) and the drift velocity (5.1.8) for the completeness.

$$\mathbf{u}_G = \mathbf{u}_L + \mathbf{u}_{\text{slip}} + \mathbf{u}_{\text{drift}}. \tag{5.1.7}$$

$$\mathbf{u}_{\text{drift}} = -\frac{\nu_T}{\sigma_G}\frac{\nabla\alpha}{\alpha}. \tag{5.1.8}$$

With this formulation of drift velocity, now it is all clear how the diffusive term arises in (4.1.9). While it is a purely convection problem, when the gas velocity is obtained according to (5.1.7)–(5.1.8), and the convective term is rewritten; the diffusion term appears and the gas velocity remains only as a function of the liquid and slip velocities.

The slip velocity (5.1.6) has the opposite direction of the gradient of the pressure, and its magnitude is quadratically proportional to the magnitude of the pressure-gradient unless the drag coefficient C_D is a function of $\mathbf{u}_{\text{slip}}$. There are various definitions of C_D; since our focus is mostly on investigating the couplings between PBE and equations of fluid dynamics, we prefer to adopt a constant drag coefficient in order to keep the model less non-linear and less demanding in computational costs. C_D (5.1.6) is adopted from the study by Bannari et al. [101] in which several other formulations are comprehensively discussed. Even though the chosen drag coefficient does not provide the most accurate results, it has the advantage that it yields to a linear formulation of $\mathbf{u}_{\text{slip}}$ after some manipulation of the equation (5.1.6). Additional nonlinearities arise with other formulations of C_D which involve $\mathbf{u}_{\text{slip}}$; then, computations get even more demanding.

Once the gas-phase velocity is obtained with the solution of turbulent fluid dynamics; in order to progress with the solution of PBE, we have all the required variables: $\mathbf{u}_g$, ε and ν_T. Then, we

can safely employ the developed solver for the PBE-CFD coupled problems (see *Chapter 4*) which is nicely suited to our purposes. The case study in our scope did not require to cover a wide range of the internal coordinate so with relatively small number of classes the required domain could be covered, i.e. solution of fewer transport equations are required. And, since we considered that all the classes/bubbles share the same velocity field, the convective operator needed to be assembled only once at the each outermost iteration (see Figure 5.1), which leaded to a great reduction in the computational cost. The problem could be solved with large time steps since the whole scheme is treated implicitly with positivity preserving linearization within Crank-Nicolson time stepping technique; therefore, the solution of PBE with MC was not a bottle-neck in this manner even though for the simulation of bubble columns they are found to be computationally costly. Moreover, since we could use the same time step sizes while marching in the solutions of the transport equations and PBE, we did not need to adopt an operator splitting approach; so that, we could modify the system matrix which we obtained after our high-order finite element discretization with the implicit treatment of the sink terms.

A last point worth to be discussed is the implementation of boundary conditions which is not a trivial subject; we follow the prescriptions by Kuzmin et al. [159]. At the inflow boundary, all velocity components and turbulent quantities, k and ε, are prescribed as Dirchlet boundary condition. At the outlet "do-nothing" boundary condition is employed which states that all the normal gradients of all the related variables vanish. The walls are modeled with the free-slip boundary condition, this requires the computation of walls' normal which can be cumbersome when the walls are not aligned with the chosen coordinate system. The gas inflow rate can be incorporated as a source into the gas phase continuity equation, and bubbles are introduced at the sparger having a size of 1 mm which corresponds to the median class (4th/6th class) for simulations with seven/eleven classes. For the further implementation details of boundary and initial conditions, and the wall functions, we encourage the reader to refer to the following studies [146, 158, 159]. Hereby, we have completed our discussion on the mathematical model and the numerical approaches and now we can present our algorithm which explains our approach to the solution within the time step t^n:

1. Solve the Navier-Stokes equations.
2. Obtain the gas velocity.
3. Solve the transport equation for the gas holdup α.
4. Solve the coupled equations of the k–ε model.
5. Check the convergence criteria for the outer-loop (1–4) for the solution of the CFD equations,
   (a) YES: pass the necessary values to population balance model and progress to solve PBE, go to 6.
   (b) NO: go on with the next iteration in the outer-loop, go to 1.
6. Solve internally coupled PBE in the outer-loop,
   (a) Calculate the sink and source terms for PBE.
   (b) Solve the transport problem for each class.
7. Check the convergence criteria for the outer-loop (*6*).
   (a) YES: calculate the d_{32} of the population and pass it to the fluid dynamics part (2) for t^{n+1}.
   (b) NO: go on with the next iteration in the outer-loop, go to (6.a).

The internal and external couplings, which are implemented according to the presented computational recipe, give rise to the nested iteration loops, Figure 5.1. It is important to see how the couplings have been realized within the nested iteration strategy; additionally, it gives an idea about the computational demand of the accordingly developed computational tool.

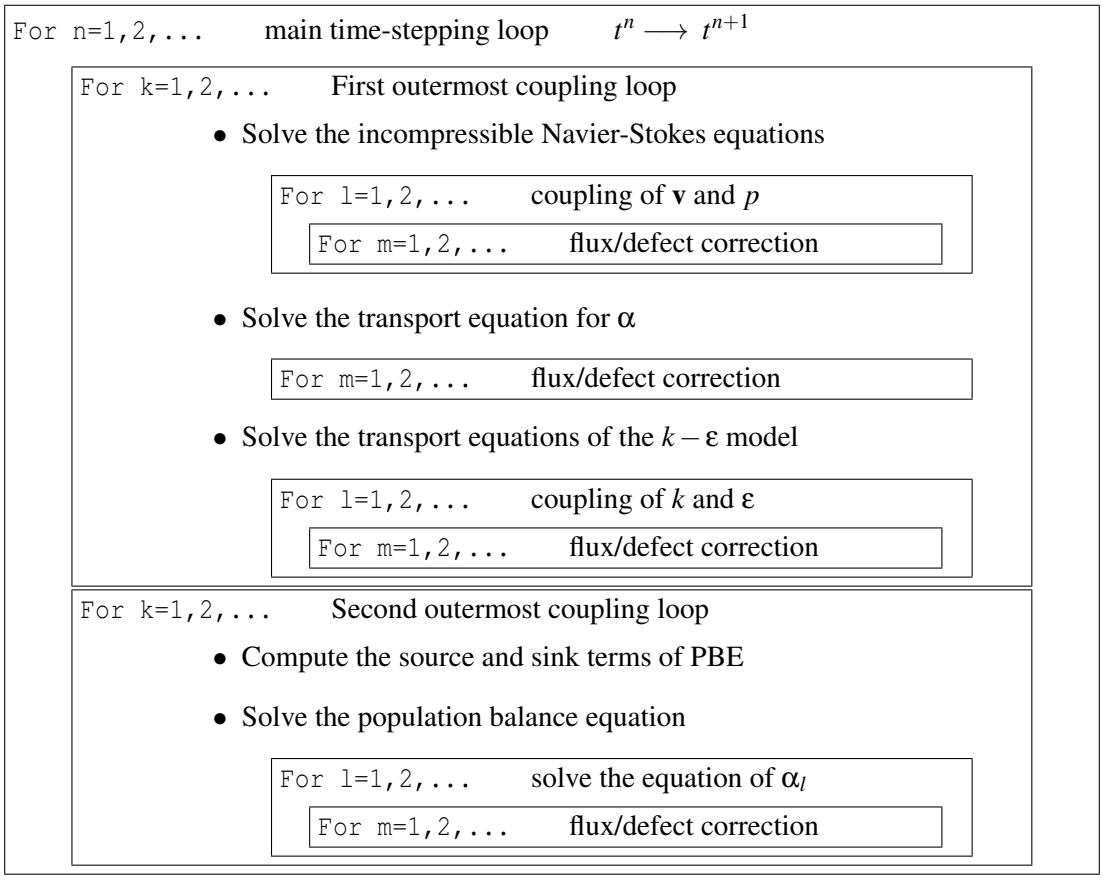

Figure 5.1: Developed computational algorithm consisting of nested iteration loops.

As a summary, the computational approach shall be explained with all details for one time step: At the time step t^n, one should first solve the Navier-Stokes equations which are modified with Boussinesq approximation (5.1.1). In order to solve these equations, the employed numerical methods methods are: FEM on unstructured grid, Pressure-Schur-Complement approach which yields to the *C2* external coupling, the loop with the l index (loop_l), see Figure 5.1.

The Burgers' equation is solved in a decoupled fashion for each velocity component, which caused the *C1* internal coupling with the nonlinear convection term. The obtained linear equations for the velocity and pressure unknowns are solved with an efficient geometrical multigrid solver in a defect correction loop (loop_m).

Then, the transport equation for the total gas holdup, α, is solved with the obtained gas velocity being computed with d_{32} from the PB part. Since this equation and the other scalar transport equations in our model are convection dominated, an SOR-solver on the finest computational grid is employed with an Algebraic Flux Correction (AFC) scheme additional to the positivity-preserving linearization in order to ensure valid non-negative solutions. Then, the coupled system of $k-\varepsilon$ equations is analogously solved in a $loop_l$. So far, *Steps 1–4* have been realized. Since all the involved equations are strongly coupled, *Steps 1–4* have to be performed in the first outermost

coupling loop. We consider that the coupling between PBE and CFD is weak, i.e., we assumed that the bubble size distribution changes negligibly while solving the CFD equations in one time-step. Thus, the slip velocity remains constant in the first outermost coupling, and we can solve PBE after we obtain a converged solution of the flow problem at the certain time-step. This assumption reduces the computational cost significantly such that we are able to simulate our problems with the developed sequential computational tool. Once the converged solution of the CFD part is obtained, the next step is the solution of PBE. First, the sink and source terms are computed with MC in a fixed-pivot fashion, *Step 6.a*; then, the related terms are incorporated into the transport equation of α_l, which is solved analogously to the previous scalar transport equations. Since the values of the classes strongly depend on each other, the equations have to be solved non-linearly in the second outermost coupling loop. When the converged solution of PBE is obtained, the corresponding d_{32} field of the population is calculated and passed to the CFD part for the computation of the slip velocity in the next time step t^{n+1}; and the discretization of equations in time is obtained according to the Crank-Nicolson method.

5.2. Numerical simulation: Becker's experiment

Becker et al. conducted elaborated experiments on the motion of bubble swarms in a partially aerated flat rectangular bubble column [160]; their studies are both experimentally and numerically very interesting and challenging.

The choice of flat geometry is due to fact that 3D flow field can be almost exactly characterized by 2D flow structures; so that, the observation of the flow field and measuring the relevant variables were easier and more accurate than doing it for 3D flow structures. On the other hand, even, when the sparger is relocated from the middle of the column to be closer to one of the side walls, the bubble swarm-motion remains unsteady [160]. However, to numerically simulate the unsteady bubble swarm-motion is very challenging for long-runs; usually, after several oscillations the bubble swarm tends approaching to the closer wall, and later it exhibits a quasi-steady flow field. Indeed, this is not an acceptable result.

The bubble column is numerically simulated within a computational domain $\Omega = (0, 0.5) \times (0, 1.5) \times (0, 0.08)\,[\mathrm{m}]$, which is a cartesian mesh of 6,912 hexahedral elements. The spatial discretization resulted in 22848×3 degrees of freedom (dof) for velocity (Ranacher-Turek element, nonconforming trilinear $\tilde{Q}_1$ FE [168]), 6912 dof for pressure (piecewise-constant Q_0 FE), and $(2+11) \times 9125$ dof for $k-\varepsilon$ equations additional to PBE (conforming trilinear Q_1 FE). The circular gas sparger with 0.06 m diameter is located at the point $(0.15, 0.00, 0.04)$ and the prescribed volumetric flow rate is $1.61/\mathrm{min}$.

We prefer to simulate breakage and coalescence on a developed flow field; hence, we obtain a flow field, firstly, with a constant slip velocity; $|\mathbf{u}_{\mathrm{slip}}| = 0.2\,\mathrm{ms}^{-1}$ in the opposite direction to gravity, as Kuzmin et al. have done [4, 146]. After time $t = 10\,\mathrm{s}$, the flow field is simulated with the population balance model coupled and the initial bubble size $d = 1\,\mathrm{mm}$. The initial bubble size is determined according to (5.1.5), the linearization parameter $C_w \approx 5 \times 10^4\,\mathrm{kgm}^{-3}\mathrm{s}^{-1}$ corresponding to the initially adopted constant $\mathbf{u}_{\mathrm{slip}}$ is considered [146].

The simulation results are similar to the observations in the experiment, the meandering bubble swarm is numerically simulated until time $t = 60\,\mathrm{s}$, see Figure 5.2. In the experiments it is observed that the flow field does not tend to be steady in the long term. Our numerical simulations show that after the 15th second the bubble swarms approaches to the near side wall, see Figure 5.2 at $t = 15\,\mathrm{s}$;

later, leading to a quasi-steady flow field at $t = 60\,\mathrm{s}$, see Figure 5.2. Although, these results are more unsteady compared to the simulations without PBE, they are not satisfactory. Nonetheless, we think that a computation that is performed on a finer spatial grid can yield to more agreeable results.

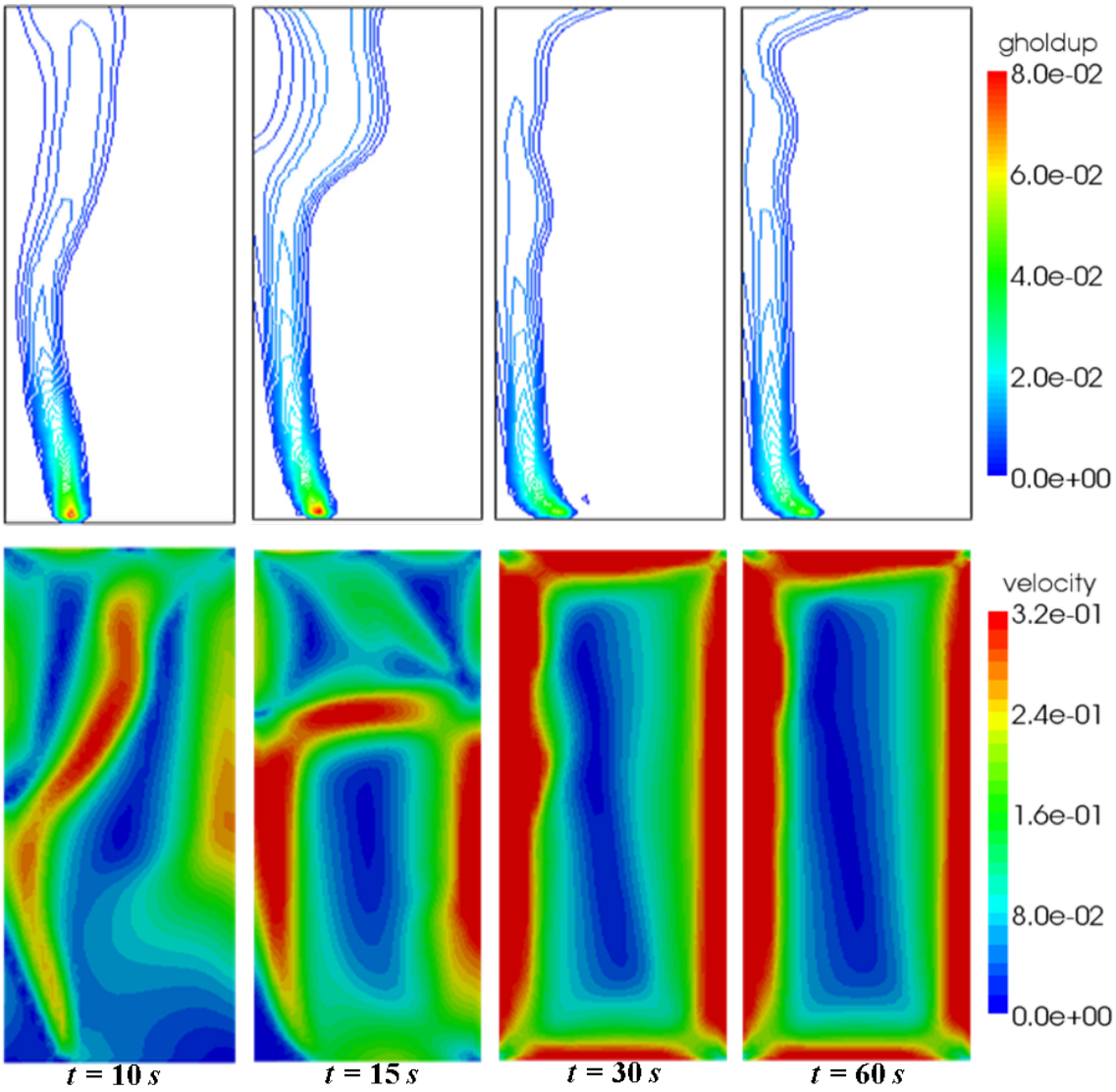

Figure 5.2: Holdup- and velocity-magnitude-field (ms^{-1}) solutions with the coarse mesh at various time-instants.

The slip velocity is one of the most influential variables on the flow field of the gas phase, and it requires that the gradient of the pressure is accurately recovered. If the flow field is resolved on a finer grid, it can be more accurately recovered; hence, we homogeneously refined our hexahedral mesh and obtained a mesh of 55,296 hexahedral elements. The simulation results are able, even in the long run, to capture the unsteady meandering bubble-swarm motion, see Figure 5.3.

We could successfully simulate the observed motion of the bubble swarm in experiments; the numerical simulation predicts a qualitatively similar meandering behavior. A great challenge, to obtain a "non-diffusive" numerical scheme so that the dynamic behavior of bubbly flows can be numerically simulated for long-runs, is achieved within an efficient implementation of PBE

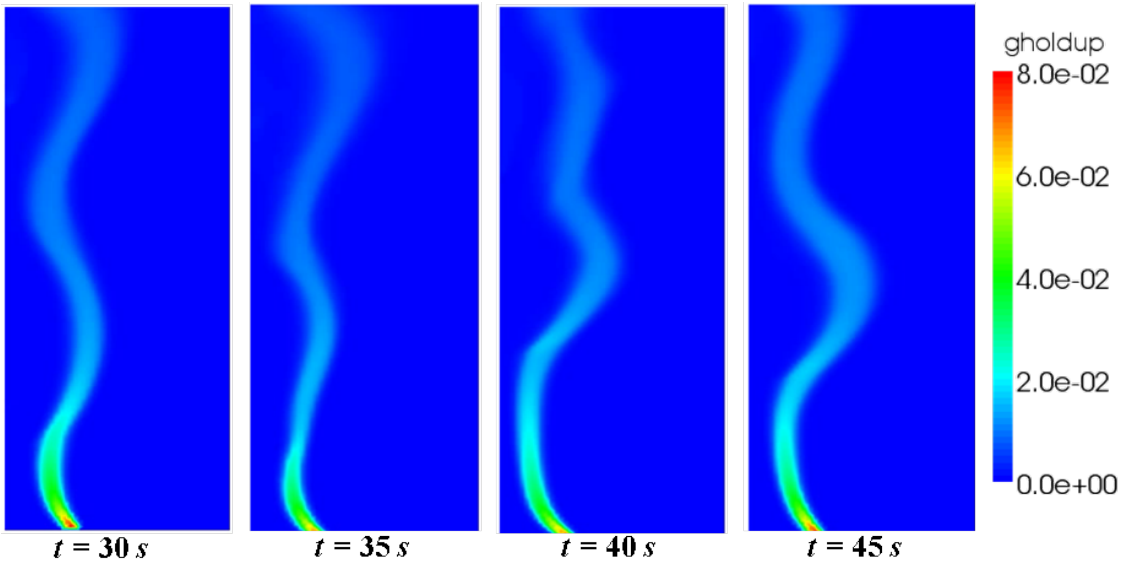

Figure 5.3: Holdup-field solutions with the fine mesh at various time-instants.

coupled to CFD. In Table 5.1, the required computational time by different parts of the PBE-CFD solver is presented for 60 s of the flow simulation which is performed on the coarse computational grid with 7 classes. The simulation is performed within a sequential computation on the AMD Opteron 250 CPU with 2.4 GHz frequency. The additional cost due to the incorporation of PBE is affordable and the required computational time remains on the same order with or without the PBE. The computation on the fine grid requires approximately 10 times larger computational time (approx. 1 week), which is at the edge of acceptable computational time for us. Therefore, although the Navier Stokes solver and the population balance solvers are efficiently parallelized within the domain decomposition method, a computation on a finer grid which would be good for the completeness of the results is currently not possible with our state-of-art turbulent-flow solver; and we leave it as a future task in our coming studies, particularly in combination with hardware-oriented techniques and GPU computing.

Table 5.1: Computational time required for the solution of different part of the model. (NS: Navier-Stokes Equ.; KE: Turbulence Equ.; α: Gas phase cont. Equ.; MP: Multiphase Equ.).

Equation	Time (s)	Time (%)
NS	33500	55.4
α	4270	7.1
KE	13200	21.8
PBE	9475	15.7
MP (PBE & α)	13745	22.8

5.3. Conclusions and outlook

PBE coupled with CFD simulations lead to agreeable results on reasonably fine computational grids. The highly nonlinear coupled-model is very demanding with respect to computational efforts and, hence, requires very accurate and efficient numerical methods. The method of classes has shown to be a good choice, being able to describe the population with few classes, 7, that adds up to an affordable computational cost. The modified models, e.g., Chien's Low-Reynolds number turbulence model [1], should be tested since the resolved flow field was mildly turbulent. The spatial discretization is of great importance: both considering the employed finite element spaces and the mesh size. Positivity preserving linearization and high-order stabilization schemes are very crucial to avoid undershoots and overshoots. In this manner, a parallel implementation of the Q2/P1 solver for the incompressible multi-fluid model and a parallel high-order FEM-AFC solver with Q1 elements for scalar transport equations (the PBE and the turbulence equations) is very promising to simulate bubbly flows. Moreover, simulations will be more comprehensive if the motion of the water surface is resolved with a surface tracking or surface capturing method, e.g., level set method [169]. In case of highly turbulent bubbly flows for which the dispersion can exhibit a wide distribution in the internal coordinate, the method of classes might be less efficient; then, another numerical method to compute PBE can be employed, e.g. DQMOM, QMOM.

A

Experimental Studies on Static Mixers

The experimental work has been executed in Sulzer Chemtech Ltd. laboratories, Winterthur, Switzerland by Evren Bayraktar. Liquid-Liquid In-Line Sizing Apparatus (LLISA) has been developed in these laboratories and has been used for measuring the size distribution of dispersed phase systems, particularly oil-in-water and water-in-oil systems; a schema of the experimental set-up is given in Figure A.1.

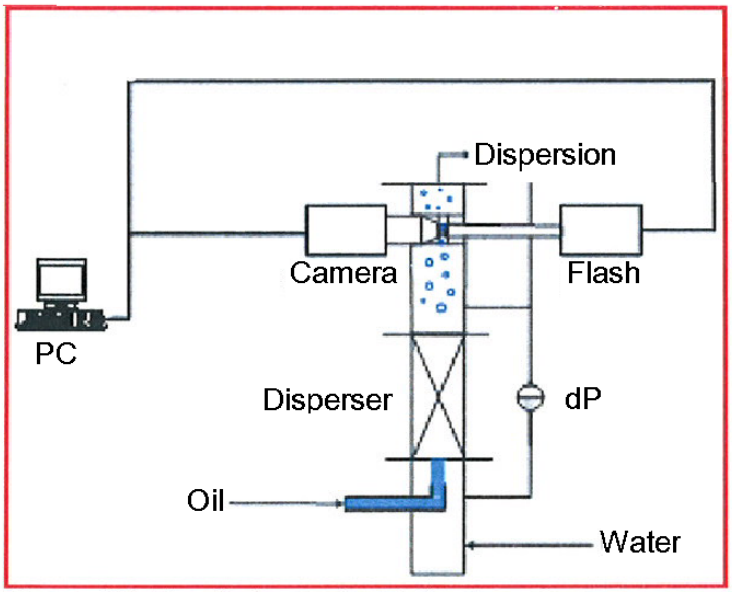

Figure A.1: Experimental setup in Sulzer Chemtech laboratories.

LLISA was designed modularly, allowing to use different sized mixers as well as altering the position of the measurement section. It has enhanced magnification features through the microscope lens, so that very small droplets (on the microscale) can be accurately measured by capturing them on the sharp focal plane. In this measurement technique, the underlying assumption is: time

integrated count of bubbles/droplets which are captured in the photographed volume represent time averaged size distribution of population in the cross section where LLISA is placed. Thus, the gap between the two windows of LLISA (at the bottom of the hallow threads where the flash and camera are placed) should always be more than a certain width such that even the largest droplets should pass with ease.

The opening width between the windows is also important to obtain sufficient illumination; so that, the droplets can be pictured sharply. Indeed, it is very difficult to obtain sharp and clear pictures for dispersed phase systems with high void fraction of the secondary phase and/or for highly turbulent flows due to increasing reflection and deflection of light rays; under these circumstances, the illumination is not the optimal for optical measurements. In order to have a better illumination so to take better pictures, one can adjust the gap between the windows of LLISA. Nevertheless, this may be a faulty solution because when the gap narrows down less than a certain width, large bubbles can be filtered out, and this causes a systematic error in measurements.

The droplet capturing apparatus is automated but evaluation of the droplet size is manual. The camera and the flash of LLISA are triggered simultaneously, and the taken pictures are saved in the disc drive of the attached computer. Then, the pictures are processed manually to evaluate the droplet size by “Bubble Count" software which is provided by Sulzer Chemtech. First, the picture-files are opened with this software, and every sharp droplet is marked with a circle; a sample picture taken by LLISA and evaluated with the Bubble Count software is shown in Figure A.2.

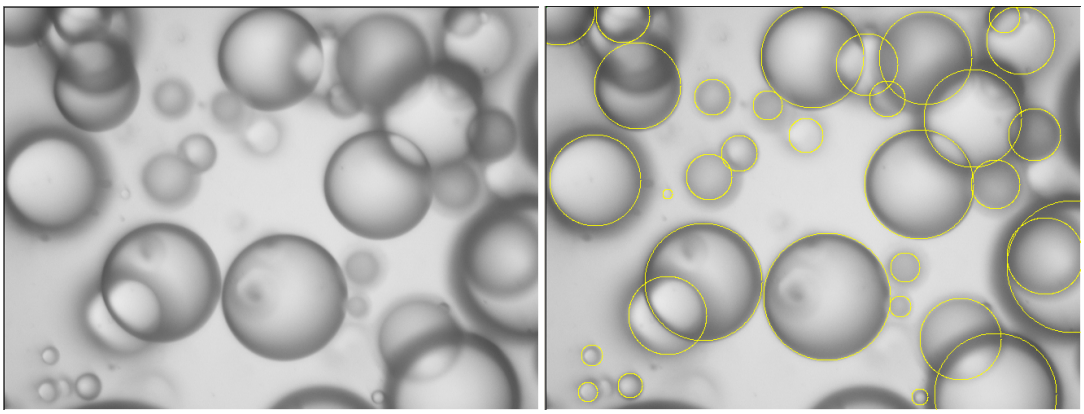

Figure A.2: Left: taken by LLISA; Right: evaluated by Bubble Count.

The evaluation of droplet sizes is rather a time consuming process because all the work has to be done manually. Nevertheless, a better alternative was not available and the Bubble Count software was the only solution. Data which are produced during evaluation of bubble sizes are saved in comma-delimited ascii files for each picture; then, the data exported from related files by a Matlab script. Later, the imported data are filtered and only radii of measured droplets are saved.

The measured radii are in pixel unit, and they have to be converted to actual sizes with a conversion factor. The required factor obtained by taking several pictures of the calibration slide (see Figure A.3) and processing them with the software. Pictures were taken by replacing the camera and flash several times so we took thirty pictures. Then, the mean value and the standard deviation of the measurements were calculated in order to determine the conversion factor and the accuracy of our measurements. The conversion factor and the standard deviation were found, respectively, to be 2.5×10^{-6} m px^{-1} and 2 px, which is equal to 5×10^{-6} m.

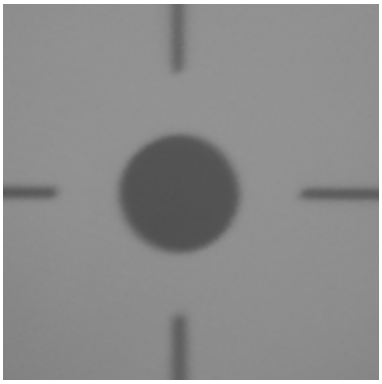

Figure A.3: Calibration slide (measured size: 80 px, actual size: 200×10^{-6} m) by LLISA.

After obtaining the conversion factor, all results were converted to the meter unit; then, mean diameter and standard deviation of the mean is calculated for each case. Nevertheless, extracting only this information from the available data was not very efficient. Besides, obtaining some distributions, e.g. Gaussian distribution, with these statistical values was not a good idea, as the physics in the problem is neglected; moreover, no evidence suggests that the size distribution of dispersed phase obeys to a predefined distribution. Therefore, we suggest a simple and reasonable post-processing without adding any more assumptions to the problem. The measured droplets (v_m) are assigned to certain classes (with υ_i^{min} and υ_i^{max} being lower and upper limit of the i'th class, respectively), as it has been done in numerical simulations; for details refer to *Section 3*.

$$if \;\; \upsilon_m \in [\upsilon_i^{min}, \upsilon_i^{max}), \quad \upsilon_m = n_{im}\upsilon_i$$

where n_{im} is the weight factor of droplet υ_m for i'th class. Then, the volume of the measured droplets is added to their corresponding classes. Finally, we obtain a size distribution for an arbitrary volume of the secondary phase. However, we know that this arbitrary volume should actually be the total-volume of the secondary phase in a certain control volume in time, because all the measurement set-up was developed based on this assumption. This knowledge leads us to calculate a discrete probability distribution (DPD) of the holdup (or volume, DPD is the same for both); dividing the volume assigned to each class by the total volume of the measured secondary phase yields to DPD:

$$Pr_i = \frac{\upsilon_i^T}{\upsilon^T}, \quad \sum \upsilon_i Pr(X = \upsilon_i) = 1$$

Then, the holdup distribution of i'th class is calculated as:

$$\alpha_i = Pr_i \alpha$$

As a consequence, the measured droplet sizes are evaluated in a way which allows to compare size distributions obtained in numerical simulations and experiments.

Bibliography

[1] Bayraktar E., Mierka O., Platte F., Kuzmin D. and Turek S., *Numerical aspects and implementation of population balance equations coupled with turbulent fluid dynamics*, Computers & Chemical Engineering, **35**-11, 2011, pp.2204–2217.

[2] Ramkrishna D., Population Balances: Theory and Applications to Particulate Systems Engineering, Academic Press, USA, 2000.

[3] Millies M. and Mewes D., *Interfacial area density in bubbly flow*, Chemical Engineering and Processing, **38**, 1999, pp.307–319.

[4] Kuzmin D. and Turek S., *Numerical simulation of turbulent bubbly flows*, In Proceedings of the Third International Symposium on Two-Phase Flow Modeling and Experimentation, Pisa, Italy, 2004.

[5] Hulburt H. M. and Katz S., *Some problems in particle technology: A statistical mechanical formulation*, Chemical Engineering Science, **19**, 1964, pp.555–574.

[6] McGraw R. and Wright D. L., *Chemically resolved aerosol dynamics for internal mixtures by the quadrature method of moments*, Journal of Aerosol Science, **34**, 2003, pp.189–209.

[7] McGraw R., *Description of aerosol dynamics by the quadrature method of moments*, Aerosol Science and Technology, **27**, 1997, pp.255–265.

[8] Fan R., Marchisio D. L. and Fox R. O., *Application of the direct quadrature method of moments to polydisperse gas–solid fluidized beds*, Journal of Aerosol Science, **139**, 2004, pp.7–20.

[9] Bove S., *Computational fluid dynamics of gas–liquid flows including bubble population balances*, PhD Thesis, Aalborg University, Denmark, 2005.

[10] Kumar S. and Ramkrishna D., *On the solution of population balance equations by discretization - I. A fixed pivot technique*, Chemical Engineering Science, **51**-8, 1996, pp.1311–1332.

[11] Kumar S. and Ramkrishna D., *On the solution of population balance equations by discretization - II. A moving pivot technique*, Chemical Engineering Science, **51**-8, 1996, pp.1333–1342.

[12] Chen P., Sanyal J., Dudukovic̀ M. P., *Numerical simulation of bubble columns flows: effect of different breakup and coalescence closures*, Chemical Engineering Science, **60**, 2005, pp.1085–1101.

[13] Jakobsen H. A., Lindborg H., and Dorao C. A., *Modeling of bubble column reactors: progress and limitations*, Industrial Engineering and Chemical Research, **44**, 2005, pp.5107–5151.

[14] Gordon G. R., *Error bounds in equilibrium statistical mechanics*, Journal of Mathematical Physics, **9**-5, 1967, pp.655–663.

[15] Coulaloglou C. A. and Tavlarides L. L., *Drop size distributions and coalescence frequencies of liquid-liquid dispersions in flow vessels*, AIChE Journal, **22**-2, 1976, pp.289–297.

[16] Tsouris C. and Tavlarides L. L., *Breakage and coalescence models for drops in turbulent dispersions*, AIChE Journal, **40**, 1994, pp.395–406.

[17] Prince M. J. and Blanch H. W., *Bubble coalescence and break-up in air-sparged bubble columns*, AIChE Journal, **36**, 1990, pp.1485–1499.

[18] H. Luo, *Coalescence, break–up and liquid circulation in bubble column reactors*, PhD Thesis, The Norwegian Institute of Technology, Norway, 1993.

[19] Buwa V. V. and Ranade V. V., *Dynamics of gas–liquid flow in a rectangular bubble column: experiments and single/multi-group CFD simulations*, Chemical Engineering Science, **57**, 2002, pp.4715–4736.

[20] Lehr F., Millies M. and Mewes D., *Bubble size distribution and flow fields in bubble columns*, AIChE Journal, **48**-11, 2002, pp.2426–2442.

[21] Hinze J. O., *Fundamentals of the hydrodynamic mechanism of splitting in dispersion processes*, AIChE Journal, **1**, 1955, pp.289–295.

[22] Kolmogorov A. N., *On the breakage of drops in a turbulent flow*, Dokl. Akad. Navk. SSSR, **66**, 1949, pp.825–828.

[23] Martínez-Baźan C., Montañés J. L., and Lasheras J. C., *On the breakup of an air bubble injected into a fully developed turbulent flow. Part 1. Breakup frequency*, Journal of Fluid Mechanics, **401**, 1999, pp.157–182.

[24] Martínez-Baźan C., Montañés J. L., and Lasheras J. C., *On the breakup of an air bubble injected into a fully developed turbulent flow. Part 2. Size PDF of the resulting daughter bubbles*, Journal of Fluid Mechanics, **401**, 1999, pp.183–207.

[25] Lee C. H., Erickson L. E., and Glasgow L. A., *Dynamics of bubble size distribution in turbulent gas liquid dispersions*, Chemical Engineering Communications, **61**, 1987, pp.181–195.

[26] Valentas K. J., Bilous O., and Amundson N.R., *Analysis of breakage in dispersed phase systems*, Industrial Engineering Chemistry Fundamentals, **5**, 1966, pp.271–279.

[27] Luo H. and Svendsen H. F., *Theoretical model for drop and bubble breakup in turbulent dispersions*, AIChE Journal, **42**, 1996, pp.1225–1233.

[28] F. Lehr and D. Mewes, *A transport equation for interfacial area density applied to bubble columns*, Chemical Engineering Science, **56**, 2001, pp.1159–1166.

[29] Wang T., Wang J. and Jin Y., *A novel theoretical breakup kernel function for bubbles/droplets in a turbulent flow*, Chemical Engineering Science, **58**, 2003, pp.4629–4637.

[30] Alexiadis A., Gardin P. and Domgin J. F., *Probabilistic approach for breakup and coalescence in bubbly-flow and coupling with CFD codes*, Applied Mathematical Modeling, **31**, 2007, pp.2051–2061.

[31] Marchisio D. L., Vigil R. D. and Fox R. O., *Implementation of the quadrature method of moments in CFD codes for aggregation breakage problems*, Chemical Engineering Science, **58**, 2003, pp.3337–3351.

[32] Öncül A. A., Niemannb B., Sundmacher K. and Thévenin D., *CFD modelling of BaSO4 precipitation inside microemulsion droplets in a semibatch reactor*, Chemical Engineering Journal, **138**, 2008, pp.498–509.

[33] Cheung S. C. P., Yeoh G. H. and Tu J. Y., *On the modelling of population balance in isothermal vertical bubbly flows. Average bubble number density approach*, Chemical Engineering and Processing, **46**, 2007, pp.742–756.

[34] Kuzmin D., Mierka O. and Turek S., *On the implementation of the k-epsilon turbulence model in incompressible flow solvers based on a finite element discretization*, International Journal of Computing Science and Mathematics, **1**-2/3/4, 2007, pp.193–206.

[35] Mierka O., *CFD modelling of chemical reactions in turbulent liquid flows*, PhD Thesis, Slovak Technical University, Slovakia, 2005.

[36] Bhole M.R., Joshi J.B. and Ramkrishna D., *CFD simulation of bubble columns incorporating population balance modeling*, Chemical Engineering Science, **63**, 2008, pp.2267–2282.

[37] Lo S., *Application of MUSIG model to bubbly flows*, AEAT-1096, AEA Technology.

[38] Cheung C., Yeoh G. and Tu J., *A review of population balance modelling for multiphase flows: approaches, applications and future aspects* in D. Matos and C. Valerio, Fluid mechanics and pipe flow: Turbulence, simulation and dynamics, Nova Science Publishers, Hauppauge, United States, 2009, pp.117–170.

[39] Kuzmin D., A guide to numerical methods for transport equations, Friedrich-Alexander-Universität, Erlangen-Nürnberg, Germany, 2010.

[40] Silva L. F. L. R., Damian R. B. and Lage P. L. C., *Implementation and analysis of numerical solution of the population balance equation in CFD packages*, Computers & Chemical Engineering, **32**-2, 2008, pp.2933-2945.

[41] Hu B., Matar O. K., Hewitt G. F. and Angeli P., *Population balance modelling of phase inversion in liquid–liquid pipeline flows*, Chemical Engineering Science, **61**-15, 2006, pp.4994–4997.

[42] McCoy B. J. and Madras G., *Analytical solution for a population balance equation wiht aggregation and fragmentation*, Chemical Engineering Science, **58**, 2003, pp.3049–3051.

[43] Schlauch S., *Modeling and Simulation of Drop Size Distributions in Stirred Liquid-Liquid Systems*, PhD Thesis, Technischen Universität Berlin, Germany, 2007.

[44] Poon J. M.H., Immanuel C. D., Doyle-III F. J. and Litster J. D., *A three-dimensional population balance model of granulation with a mechanistic representation of the nucleation and aggregation phenomena*, Chemical Engineering Science, **63**-5, 2008, pp.1315-1329.

[45] Marshall Jr. C. L. , Rajniak P. and Matsoukas T., *Multi-component population balance modeling of granulation with continuous addition of binder*, Powder Technology, **236**, 2013, pp. 211-220.

[46] Fox R.O., *Bivariate direct quadrature method of moments for coagulation and sintering of particle populations*, Journal of Aerosol Science, **37**-11, 2006, pp.1562–1580.

[47] Roussos A.I.and Kiparissides C., *A bivariate population balance model for the microbial production of poly(3-hydroxybutyrate)*, Chemical Engineering Science, **70**, 2012, pp.45–53.

[48] Briesen H., *Simulation of crystal size and shape by means of a reduced two-dimensional population balance model*, Chemical Engineering Science, **61**, 2006, pp.104–112.

[49] Buffo A., Vanni M. and Marchisio D.L., *Multidimensional population balance model for the simulation of turbulent gas–liquid systems in stirred tank reactors*, Chemical Engineering Science, **70**, 2012, pp.31–44.

[50] Rollié S., Briesen H. and Kai S., *Discrete bivariate population balance modeling of heteroaggregation processes*, Journal of Colloid and Interface Science, **336**-2, 2009, pp.551–564.

[51] Krallis A. and Kiparissides C., *Mathematical modeling of the bivariate molecular weight–long chain branching distribution of highly branched polymers.: A population balance approach*, Chemical Engineering Science, **62**-18–20, 2007, pp.5304–5311.

[52] Marchisio D. L. and Barresi A. A., *Investigation of soot formation in turbulent flames with a pseudo-bivariate population balance model*, Chemical Engineering Science, **64**-2, 2009, pp.294–303.

[53] Niemann B. and Sundmacher K., *Nanoparticle precipitation in microemulsions: Population balance model and identification of bivariate droplet exchange kernel*, Journal of Colloid and Interface Science, **342**-2, 2010, pp.361–371.

[54] Diemer Jr. R. B. and Olson J. H., *Bivariate moment methods for simultaneous coagulation, coalescence and breakup*, Journal of Aerosol Science, **37**-3, 2006, pp.363–385.

[55] Björn I. N., Jansson A., Karlsson M., Folestad S. and Rasmuson A., *Empirical to mechanistic modelling in high shear granulation*, Chemical Engineering Science, **60**-14, 2005, pp.3795–3803.

[56] Smagala T. G. and McCoy B. J., *Population balance modeling of polymer branching and hyperbranching*, Chemical Engineering Science, **61**-1, 2006, pp.3–17.

[57] Terrazas-Velarde K., Peglow M. and Tsotsas E., *Stochastic simulation of agglomerate formation in fluidized bed spray drying: A micro-scale approach*, Chemical Engineering Science, **64**-11, 2009, pp.2631–2643.

[58] Braumann A. and Kraft M., *Incorporating experimental uncertainties into multivariate granulation modelling*, Chemical Engineering Science, **65**-3, 2010, pp.1088–1100.

[59] Lakatos B. G., Bárkányi A. and Németh S., *Continuous stirred tank coalescence/redispersion reactor: A simulation study*, Chemical Engineering Journal, **169**-1–3, 2011, pp.247–257.

[60] Chauhan S. S., Chiney A. and Kumar S., *On the solution of bivariate population balance equations for aggregation: Xâdiscretization of space for expansion and contraction of computational domain*, Chemical Engineering Science, **70**-5, 2012, pp.135–145.

[61] Alexopoulos H. A. and Kiparissides C., *Solution of the bivariate dynamic population balance equation in batch particulate systems: Combined aggregation and breakage*, Chemical Engineering Science, **62**-18–20, 2007, pp.5048–5053.

[62] Wright D. L., McGraw R. and Rosner D. E., *Bivariate extension of the quadrature method of moments for modeling simultaneous coagulation and sintering of particle populations*, Journal of Colloid and Interface Science, **236**-2, 2001, pp.242–251.

[63] Alexopoulos A.H., Roussos A. and Kiparissides C., *Part V: Dynamic evolution of the multivariate particle size distribution undergoing combined particle growth and aggregation*, Chemical Engineering Science, **64**-14, 2009, pp.3260–3269.

[64] Favero J.L. and Lage P.L.C., *The dual-quadrature method of generalized moments using automatic integration packages*, Computers & Chemical Engineering, **38**-5, 2012, pp.1–10.

[65] Irizarry R., *Fast Monte Carlo methodology for multivariate particulate systems-I: Point ensemble Monte Carlo*, Chemical Engineering Science, **63**-1, 2008, pp.95–110.

[66] Irizarry R., *Fast Monte Carlo methodology for multivariate particulate systems-II: –PEMC*, Chemical Engineering Science, **63**-1, 2008, pp.111–121.

[67] Chakraborty J. and Kumar S., *A new framework for solution of multidimensional population balance equations*, Chemical Engineering Science, **62**-15, 2007, pp.4112–4125.

[68] Heineken W., Flockerzi D., Voigt A. and Sundmacher K., *Dimension reduction of bivariate population balances using the quadrature method of moments*, Computers & Chemical Engineering, **35**-1, 2011, pp.50–62.

[69] John V., Mitkova T., Roland M., Sundmacher K., Tobiska L. and Voigt A., *Simulations of population balance systems with one internal coordinate using finite element methods*, Chemical Engineering Science, **64**-4, 2009, pp.733–741.

[70] Meimaroglou D. and Kiparissides C., *Monte Carlo simulation for the solution of the bi-variate dynamic population balance equation in batch particulate systems*, Chemical Engineering Science, **62**-18–20, 2007, pp.5295–5299.

[71] van Peborgh Gooch J. R. and Hounslow M. J., *Monte Carlo simulation of size-enlargement mechanisms in crystallization*, AIChE J., **42**, 1996, pp.1864–1874.

[72] Spielman L. A. and Levenspiel O., *A Monte Carlo treatment for reacting and coalescing dispersed phase systems*, Chemical Engineering Science, **20**-3, 1965, pp.247–254.

[73] Ramkrishna .D, *Analysis of population balance–IV: The precise connection between Monte Carlo simulation and population balances*, Chemical Engineering Science, **36**-7, 1981, pp.1203–1209.

[74] Goodson M. and Kraft M., *Simulation of coalescence and breakage: an assessment of two stochastic methods suitable for simulating liquid–liquid extraction*, Chemical Engineering Science, **59**-18, 2004, pp.3865–3881.

[75] Zucca A., Marchisio D. L., Vanni M. and Barresi A. A., *Validation of bivariate DQMOM for nanoparticle processes simulation*, AIChE J., **53**, 2007, pp.918–931.

[76] Kruis E. F., Wei J., van der Zwaag T. and Haep S., *Computational fluid dynamics based stochastic aerosol modeling: Combination of a cell-based weighted random walk method and a constant-number Monte-Carlo method for aerosol dynamics*, Chemical Engineering Science, **70**-5, 2012, pp.109–120.

[77] Attarakih M., *Solution methodologies for the population balance equations describing the hydrodynamics of liquid-liquid extraction contactors*, PhD Thesis, Technischen Universit at Kaiserslautern, Germany, 2004.

[78] Bleck, R., *A Fast, Approximative Method for Integrating the Stochastic Coalescence Equation*, J. Geophys. Res., **75**-27, 1970, pp.5165–5171.

[79] Gelbard F. and Seinfeld J. H., *Numerical solution of the dynamic equation for particulate systems*, Journal of Computational Physics, **28**-3, 1978, pp.357-375.

[80] Hounslow, M. J., Ryall, R. L. and Marshall, V. R., *A discretized population balance for nucleation, growth, and aggregation*, AIChE J., **34**, 1988, pp.1821–1832.

[81] Mahoney A. W. and Ramkrishna D., *Efficient solution of population balance equations with discontinuities by finite elements*, Chemical Engineering Science, **57**-7, 2002, pp.1107-1119. doi: 10.1016/S0009-2509(01)00427-4.

[82] Batterham, R. J., Hall, J. S. and Barton, G., Pelletizing kinetics and simulation of full scale balling circuits, *Proceedings of the Third International Symposium on Agglomeration*, 1981, A316–A150, Nürnberg, Germany.

[83] Kumar S. and Ramkrishna D., *On the solution of population balance equations by discretization - I. A fixed pivot technique*, Chemical Engineering Science, **51**-8, 1996, pp.1311–1332.

[84] Kumar S. and Ramkrishna D., *On the solution of population balance equations by discretization - II. A moving pivot technique*, Chemical Engineering Science, **51**-8, 1996, pp.1333–1342.

[85] M. Kostoglou and A.J. Karabelas, *Evaluation of Zero Order Methods for Simulating Particle Coagulation*, Journal of Colloid and Interface Science, **163**-2, 1994, pp.420–431.

[86] Marchal P., David R., Klein J.P., Villermaux J., *Crystallization and precipitation engineering–I. An efficient method for solving population balance in crystallization with agglomeration*, Chemical Engineering Science, **43**-1, 1988, pp.59–67.

[87] Gelbard F., Seinfeld J. H., *Simulation of multicomponent aerosol dynamics*, Journal of Colloid and Interface Science, **78**-2, 1980, pp.4850–501.

[88] Nicmanis, M. and Hounslow, M. J., *Finite-element methods for steady-state population balance equations*, AIChE J., **44**, 1998, pp.2258–2272.

[89] Wulkow M., Gerstlauer A. and Nieken U., *Modeling and simulation of crystallization processes using parsival*, Chemical Engineering Science, **56**-7, 2001, pp.2575–2588.

[90] Vanni, M., *Discretization procedure for the breakage equation*, AIChE J., **45**, 1999, pp.916–919.

[91] Lister J. D., Smit D. J. and Hounslow M. J., *Adjustable discretized population balance for growth and aggregation*, AIChE J., **41**, 1995, pp.591–603.

[92] Vanni M., *Approximate population balance equations for aggregation–breakage processes*, Journal of Colloid and Interface Science, **221**-2, 2000, pp.143–160.

[93] Puel F., Févotte G. and Klein J.P., *Simulation and analysis of industrial crystallization processes through multidimensional population balance equations. Part 1: a resolution algorithm based on the method of classes*, Chemical Engineering Science, **58**-16, 2003, pp.3715–3727.

[94] Attarakih M. M., Bart H.-J. and Faqir N. M., *Solution of the population balance equation for liquid-liquid extraction columns using a generalized fixed-pivot and central difference schemes*, In Andrzej Kraslawski and Ilkka Turunen (Eds.), Computer Aided Chemical Engineering, **14**, 2003, pp.557–562.

[95] Attarakih M. M., Bart H.-J. and Faqir N. M., *Solution of the droplet breakage equation for interacting liquid–liquid dispersions: a conservative discretization approach*, Chemical Engineering Science, **59**-12, 2004, pp.2547-2565.

[96] Attarakih M. M., Bart H.-J. and Faqir N. M., *Numerical solution of the spatially distributed population balance equation describing the hydrodynamics of interacting liquid–liquid dispersions*, Chemical Engineering Science, **59**-12, 2004, pp.2567–2592.

[97] Bove S., Solberg T., Hjertager B. H., *A novel algorithm for solving population balance equations: the parallel parent and daughter classes. Derivation, analysis and testing*, Chemical Engineering Science, **60**-5, 2005, pp.1449–1464,

[98] Alopaeus V., Laakkonen M. and Aittamaa J., *Solution of population balances with breakage and agglomeration by high-order moment-conserving method of classes*, Chemical Engineering Science, **61**-20, 2006, pp.6732–6752.

[99] Alopaeus V., Laakkonen M. and Aittamaa J., *Solution of population balances with growth and nucleation by high order moment-conserving method of classes*, Chemical Engineering Science, **62**-8, 2007, pp.2277–2289.

[100] Alopaeus V., Laakkonen M. and Aittamaa J., *Solution of population balances by high order moment-conserving method of classes: reconstruction of a non-negative density distribution*, Chemical Engineering Science, **63**-10, 2008, pp.2741–2751.

[101] Bannari R., Kerdouss F., Selma B., Bannari A. and Proulx P., *Three-dimensional mathematical modeling of dispersed two-phase flow using class method of population balance in bubble columns*, Computers & Chemical Engineering, **32**-12, 2008, pp.3224–3237.

[102] Selma B., Bannari R., Proulx P., *Simulation of bubbly flows: Comparison between direct quadrature method of moments (DQMOM) and method of classes (CM)*, Chemical Engineering Science, **65**-6, 2010, pp.1925–1941.

[103] McGraw R. and Saunders H. J., *A condensation feedback mechanism for oscillatory nucleation and growth*, Aerosol Science Technology, 1984, pp.367–380.

[104] Frenklach M. and Harris S. J., *Aerosol dynamics modeling using the method of moments*, Journal of Colloid and Interface Science, **118**-1, 1987, pp.252–261.

[105] Pratsinis S. E., *Simultaneous nucleation, condensation, and coagulation in aerosol reactors*, Journal of Colloid and Interface Science, **124**-2, 1988, pp.416-427.

[106] Melikhov I.V. and Berliner I.V., *Simulation of batch crystallization*, Chemical Engineering Science, **36**-6, 1981, pp.1021–1034.

[107] Wey J.S, *analysis of batch crystallization processes*, Chemical Engineering Communications, **35**-1–6, 1985, pp.231–252.

[108] Nagy Z.K., Fujiwara M. and Braatz R.D., *Modelling and control of combined cooling and antisolvent crystallization processes*, Journal of Process Control, **18**-9, 2008, pp.856–864.

[109] K.W Lee, *Conservation of particle size distribution parameters during Brownian coagulation*, Journal of Colloid and Interface Science, **108**-1, 1985, pp.199–206.

[110] Madras N. and Sokal A.D., *The pivot algorithm: A highly efficient Monte Carlo method for the self-avoiding walk*, Journal of Statistical Physics, **50**-1, 1998, pp.109–186.

[111] Frenklach M., *Method of moments with interpolative closure*, Chemical Engineering Science, **57**-12, 2002, pp.2229–2239.

[112] Diemer R. B. and Olson J. H., *A moment methodology for coagulation and breakage problems: Part I–analytical solution of the steady-state population balance*, Chemical Engineering Science, **57**-12, 2002, pp.2193–2209.

[113] Barrett J. C. and Webb N. A., *A comparison of some approximate methods for solving the aerosol general dynamic equation*, Journal of Aerosol Science, **29**-1–2, 1998, pp.31–39.

[114] Marchisio D. L., Pikturna J. T., Fox R. O., Vigil R. D. and Barresi A. A., *Quadrature method of moments for population-balance equations*, AIChE J., **49**, 2003, pp.1266–1276.

[115] Marchisio D. L., Vigil R. D. and Fox R. O., *Quadrature method of moments for aggregationâbreakage processes*, Journal of Colloid and Interface Science, **258**-2, 2003, pp.322–334.

[116] Marchisio D. L., Vigil R. D. and Fox R. O., *Implementation of the quadrature method of moments in CFD codes for aggregation breakage problems*, Chemical Engineering Science, **58**, 2003, pp.3337–3351.

[117] Marchisio D. L. and Fox R. O., *Solution of population balance equations using the direct quadrature method of moments*, Journal of Aerosol Science, **36**-1, 2005, pp.43–73.

[118] Frontini M., Rodriguez G. and Seatzu S., *An algorithm for computing minimum norm solutions of finite moment problems*, In J.C. Mason, M.G. Cox (Eds.), Algorithms for Approximation II, Chapman, London, 1988, pp.361–369.

[119] John V., Angelov I., Öncül A. A. and Thévenin D., *Techniques for the reconstruction of a distribution from a finite number of its moments*, Chemical Engineering Science, **62**-11, 2007, pp.2890–2904.

[120] Kostoglou M. and Karabelas A.J., *Toward a unified framework for the derivation of breakage functions based on the statistical theory of turbulence*, Chemical Engineering Science, **60**, 2005, pp.6584–6595.

[121] Bakhbakhi Y., *A discretized population balance for particle formation from gas antisolvent process: The combined Lax-Wendroff and Crank-Nicholson method*, Computers & Chemical Engineering, **33**-6, 2009, pp.1132–1140.

[122] Batchelor G. K., The Theory of Homogeneous Turbulence, 1956, Cambridge University Press.

[123] Scott W. T., *Analytic studies of cloud droplet coalescence I.* Journal of Atmospheric Sciences, **25**, 1967, pp.54–65.

[124] P. M. Wilkinson, *Physical aspects and scale-up of high pressure bubble columns*, PhD Thesis, 1991, University Groningen, The Netherlands.

[125] Grienberger J. and Hofmann H., *Investigation and Modelling of Bubble Columns*, Chemical Engineering Science, **47**, 1992, pp.2215–2220.

[126] Schrag H. J., *Blasengrössen-Häufigkeitsverteilungen bei der Begasung von Gemischen organisch-chemischer Flüssigkeiten mit Stickstoff in Blasensäulen-Reaktoren*, PhD Thesis, 1976, University Aachen, Germany.

[127] Laakkonen M., Moilanen P., Alopaeus V. and Aittamaa J., *Modelling local bubble size distributions in agitated vessel*, Chemical Engineering Science, **62**, 2007, pp.721–740.

[128] Olmos E., Gentric C. , Vial C., Wild G. and Midoux N., *Numerical simulation of multiphase flow in bubble column reactors. lnfluence of bubble coalescence and break-up*, Chemical Engineering Science, **56**, 2001, pp.6359–6365.

[129] Gäbler A., Wegener M., Paschedag A. R. and Kraume M., *The effect of pH on experimental and simulation results of transient drop size distributions in stirred liquid–liquid dispersions*, Chemical Engineering Science, **61**-9, 2006, pp. 3018–3024.

[130] Andersson R. and Andersson B., *On the breakup of fluid particles in turbulent flows*, AIChE J., **5**, pp. 2020–2030.

[131] Liao Y. and Lucas D., *A literature review of theoretical models for drop and bubble breakup in turbulent dispersions*, Chemical Engineering Science, **64**-15, 2009, pp. 3389–3406.

[132] Hu B., Pacek A. W., Stitt E. H. and Nienow A. W., *Bubble sizes in agitated air alcohol systems with and without particles: turbulent and transitional flow*, Chemical Engineering Science, **62**, 2005, pp.6371–6377.

[133] Chien K. Y., *Predictions of channel and boundary-layer flows with a low-Reynolds-Number Turbulence Model*, *AIAA J.*, **20**, 1982, pp.33-3-8.

[134] A. Sokolichin, Eigenberger G., Lapin A. and Lübert A., *Dynamical numerical simulation of gas-liquid two-phase flows Euler/Euler versus Euler/Lagrange*, Chemical Engineering Science, **52**-5, 1997, pp.611–626.

[135] Launder B. and Spalding D., *The numerical computation of turbulent flows,* Computer Methods in Applied Mechanics and Engineering **3**, 1974, pp.269–289.

[136] Lew A. J., Buscaglia G. C. and Carrica P. M., *A note on the numerical treatment of the k-epsilon turbulence model,* Int. J. of Comp. Fluid Dyn., **14**, 2001, pp.201–209.

[137] Turek S., *Efficient Solvers for Incompressible Flow Problems: An Algorithmic and Computational Approach*, 1999, Springer-Verlag, Berlin Heidelberg, Germany.

[138] Hysing S., *Numerical simulation of immiscible fluids with FEM Level-Set techniques*, PhD Thesis, Universit at Dortmund, Germany, 2007.

[139] Kuzmin D., Mierka O. and Turek S., *On the implementation of the k–epsilon turbulence model in incompressible flow solvers based on a finite element discretization* , Int. J. Comput. Sci. Math., **2**-4, 2007, pp.193–206.

[140] Rannacher R. and Turek S., *A simple nonconforming quadrilateral Stokes element,* Num. Meth. Part. Diff. Equ., **8**, 1992, pp.97–111.

[141] Benzi M., Golub G. H. and Liesen J., *Numerical solution of saddle point problems*, Acta numerica, **14**, 2005, pp.1–137.

[142] Turek S., *Multilevel Pressure Schur Complement techniques for the numerical solution of the incompressible Navier-Stokes equations*, 1997, IWR.

[143] Ohmori K. and Ushijima T., *A technique of upstream type applied to a linear nonconforming finite element approximation of convective diffusion equations*, Analyse numérique, **18**-3, 1984, pp.309–332.

[144] Schieweck F. and Tobiska L., *An optimal order error estimate for an upwind discretization of the Navier-Stokes equations. Numerical Methods for Partial Differential Equations*, **12**-4, 1996, pp.407–421.

[145] Hughes T. J. R. and Brooks A., *A multidimensional upwind scheme with no crosswind diffusion*. In Hughes T. J. R. (Ed.), Finite element methods for convection dominated flows, AMD, **34**, 1979, pp. 19–35.

[146] Kuzmin D., Turek S. and Hario H., *Finite element simulation of turbulent bubbly flows in gas-liquid reactors*, Ergebnisberichte des Instituts für Angewandte Mathematik, Nummer 298, 2005, Fakultät für Mathematik, TU Dortmund.

[147] Mierka O., Kuzmin D. and Turek S., *Finite element simulation of turbulent bubbly flows*, Ergebnisberichte des Instituts für Angewandte Mathematik, Nummer 317, 2006, Fakultät für Mathematik, TU Dortmund.

[148] Boris J. P. and Book D. L., *Flux-corrected transport. I. SHASTA, A fluid transport algorithm that works*,3 Journal of computational physics, **11**-1, 1973, pp.38–69.

[149] L ohner R., Morgan K., Peraire J. and Vahdati M., *Finite element flux-corrected transport (FEM–FCT) for the euler and Navier-Stokes equations*, Int. J. Numer. Meth. Fluids, **7**, 1987, pp.1093–1109.

[150] Kuzmin D., Möller M. and Turek S., *High-resolution FEM–FCT schemes for multidimensional conservation laws*, Computer Methods in Applied Mechanics and Engineering, **193**-45, 2004, pp.4915–4946.

[151] Kuzmin D. and Turek S., *High-resolution FEM-TVD schemes based on a fully multidimensional flux limiter*, Journal of Computational Physics, **198**-1, 2004, pp.131-158.

[152] Kuzmin D., *On the design of general–purpose flux limiters for finite element schemes I, Scalar convection*, Journal of Computational Physics, **219**, 2006, pp. 513–531.

[153] Mohammadi B. and Pironneau 0., *A stable algorithm for the* $k-\varepsilon$ *model for compressible flows*. INRIA Research Report: 1355, 1990.

[154] Silva L.F.L.R., Rodrigues R.C., Mitre J.F. and Lage P.L.C., *Comparison of the accuracy and performance of quadrature-based methods for population balance problems with simultaneous breakage and aggregation*, Computers & Chemical Engineering, **34**-3, 2010, pp. 286–297.

[155] Rama Rao N.V., BairdM.H.I., Hrymak A.N. and Wood P.E.; *Dispersion of high-viscosity liquidâliquid systems by flow through SMX static mixer elements* Chemical Engineering Science, **62**, 2007, pp. 6885–6896.

[156] Thakur R. K., Vial Ch., Nigam K. D. P., Nauman E. B. and Djelveh G. *Static Mixers in the process industries–A Review* Trans IChemE, **81**, 2003, pp.787–826.

[157] Henrik R., *Computational fluids dynamics of dispersed two-phase flows at high phase fractions* PhD Thesis, Imperial College, London, 2005.

[158] Kuzmin D. and Turek S., *Finite element discretization and iterative solution techniques for multiphase flows in gas-liquid reactors*, In Glowinski, Krizek and Neittaanmäki (Eds.), Conjugate Gradient Algorithms and Finite Element Methods, Springer, Jyväskylä, Finland, 2002.

[159] Kuzmin D., Löhner R. and Turek S., *Flux-Corrected Transport*, in: Kuzmin, Löhner and Turek, Scientific Computation: Principles, Algorithms and Applications, Springer, 2005.

[160] Becker S., Sokolichin A. and Eigenberger G., *Gas-liquid flow in bubble columns and loop reactors: Part II*, Chemical Engineering Science, **49**, 1994, pp.5747–5762.

[161] Sokolichin A. and Eigenberger G., *Applicability of the standard $k-\varepsilon$ turbulence model to the dynamic simulation of bubble columns: Part I. Detailed numerical simulations*, Chemical Engineering Science, **54**-13/14, 1999, pp.2273–2284.

[162] Borchers O., Busch C., Sokolichin A. and Eigenberger G., *Applicability of the standard $k-\varepsilon$ turbulence model to the dynamic simulation of bubble columns. Part II: Comparison of detailed experiments and flow simulations*, Chemical Engineering Science, **54**-24, 1999, pp.5927–5935.

[163] Fox R. O., Laurent F. and Massot M., *Numerical simulation of spray coalescence in an Eulerian framework: Direct quadrature method of moments and multi-fluid method*, Journal of Computational Physics, **227**-6, 2008, pp.3058–3088.

[164] Vié A., Laurent F. and Massot M., *Size-velocity correlations in hybrid high order moment/multi-fluid methods for polydisperse evaporating sprays: Modeling and numerical issues*, Journal of Computational Physics, **237**-15, 2013, pp.177–210.

[165] Sokolichin A., Eigenberger G. and Lapin A., *Simulation of buoyancy driven bubbly flow: Established simplifications and open questions*, AIChE Journal, **50**, 2004, pp.24–45.

[166] Sokolichin A., *Mathematische Modellbildung und numerische Simulation von Gas–Flüssigkeits-Blasenströmungen*, Habilitationsschrift, Universität Stuttgart, 2004.

[167] Bayraktar E., Münster R., Mierka O. and Turek S., *Numerical methods to simulate turbulent dispersed flows in complex geometries*. In Schindler and Kraume (Eds.), Proceeding of the Sixth International Berlin Workshop on Transport Phenomena with Moving Boundaries (Berlin, Germany, November 24-25, 2011).

[168] Rannacher R. and Turek S., *A simple nonconforming quadrilateral Stokes element.*, Numer. Meth. PDEs, **8**,-2, 1992, pp.97–11.

[169] Turek S., Mierka O., Hysing S. and Kuzmin D., *Numerical study of a high order 3D FEM–Level Set approach for immiscible flow simulation*. In Repin S. and Tiihonen T. and Tuovinen T. (Eds.), Numerical methods for differential equations, optimization, and technological problems, **27**, 2012, pp.65–70, Springer.